# Electronic transport in mixed-phase hydrogenated amorphous/nanocrystalline silicon thin films

A DISSERTATION
SUBMITTED TO THE FACULTY OF THE GRADUATE SCHOOL
OF THE UNIVERSITY OF MINNESOTA
BY

Lee Raymond Wienkes

IN PARTIAL FULFILLMENT OF THE REQUIREMENTS
FOR THE DEGREE OF
DOCTOR OF PHILOSOPHY

Dr. James Kakalios

May 2013

**Acknowledgements**

I wish that one could go back and write their acknowledgements after a year or two away from graduate school – I think it is only with the benefit of hindsight that we truly appreciate the most meaningful impacts that others have made on our lives. However, I will do my best to thank all those who have helped me along the way. To begin with, I would like to thank my adviser James Kakalios, who has been a constant source of encouragement and enthusiasm during my graduate career. No matter what setbacks we encountered, Jim never let it get him down and was endlessly optimistic about our prospects. Jim allowed me to find my own path in the research world by treading the line between offering advice and telling me what to do. Though sometimes this made research difficult as a young student, such experiences have helped me develop a sense of what constitutes an important (and feasible) research problem and ultimately made me a better scientist.

The previous generation of students in the Kakalios lab, Yves Adjallah and Charlie Blackwell, were instrumental in beginning my experimental physics education. Yves introduced me to many of the basic characterization techniques during my first summer in the lab. More importantly, Yves instilled in me an appreciation for the intangible skills that keep a project running smoothly, though at the time I did not fully appreciate the lessons that I was being taught. May I continue to twist arms in your name Yves! Charlie introduced me to the black art which is plasma deposition, including my first real introduction to vacuum technology. Ghidewon Arefe was another source of vacuum and plasma technology knowledge and was instrumental in the first of a series of

renovations to the deposition system which culminated in the system described in the last section of chapter 3. While I was on the way out as the system was completed, I hope future generations of Kakalios students will benefit from the improved capabilities this system affords. Kent Bodurtha has been a constant fixture in the lab during my time there and has been a willing participant in many of my 'lab improvement' schemes. In particular, Kent was an equal partner in the development of the improved software which has enhanced our data collection efficiency. As Kent once pointed out, he officially started one week before I did despite being a year younger in graduate student years and therefore holds seniority over me. Thankfully Kent was not a stickler for rank! I would also like to thank the other transient members of the Kakalios lab over the years: Chris Pyawasit for building the 'CPM dark room' with Charlie my first summer here; Aaron Besaw, who was a CPM workhorse for a summer as a MRSEC student; Trevor Hutchinson, who collected some of the thermal equilibration data presented here during a summer REU; Cameron Nicholas for his assistance resurrecting the noise system; and newcomer to the lab Zvie Razieli for his assistance on fixing both the closed-cycle Janis cryostat and the noise system.

There are many fellow students from outside the Kakalios group to thank. Many members of the Goldman and Crowell groups – Joe Kinney, Yeonbae Lee, Steve Snyder, JJ Nelson and Chad Geppert – graciously taught me the ins and outs of working at low temperatures when my research led me away from our traditional room temperature and above measurement range. The Kortshagen group in the Mechanical Engineering Department has been my adoptive lab over the past several years and I have benefited

immensely from interacting with such a large and dynamic group. They have always been willing to share their knowledge and experience with me. In particular, I would like to thank Becky Anthony, Dave Rowe, Jason Trask, Lance Wheeler, Nic Kramer, Jeslin Wu and Ariel Chatman. Dave Rowe deserves a special mention for his willingness to push for and be involved in a complete reconstruction of the deposition system. Dave's set of 'real world' experiences kept the project on track and I have learned much from working so closely with him. I would also like to thank part-time Kortshagen member Rick Liptak for offering his technical assistance during the reconstruction of the deposition system and for freely sharing his knowledge of semiconductor characterization. To the many members of my incoming class – Joe Kinney, Xiaofei Wang, Nick Raddatz, Elizabeth Smith, Kate Raach, Brian Skinner, Abe Reddy – it has been a pleasure to get to know you and I am grateful to have had such a wonderful group of friends, particularly during those long nights of first year homework sets.

Many of the staff and faculty at the University of Minnesota have also contributed to this work. I would like to thank Boris Shklovskii for several helpful discussions on transport in nanoparticles and Uwe Kortshagen for enlightening conversations about nanoparticles and plasmas. Al Knutson provided me with a constant source of electronics parts and knowledge. Graham, Alex and the rest of the IT staff were helpful in my early years of graduate school as I tried to cobble together enough computers to more effectively automate our data collection. The folks at the Physics Department machine shop (Jon, Peter, Ron and Roger) have helped me in my many adventures in the student machine shop. Kurt Wick, in addition to providing equipment from the MXP storehouse,

has helped me develop a more complete knowledge of experimental physics. Though teaching MXP is probably more work than any other course in the department, it is humbling to realize just how much I have learned from teaching this undergraduate course. The Nanofabrication Center (NFC) staff, especially Greg Cibuzar and Gary Olin, has been extremely helpful by offering their time and expertise in order to ensure that our deposition system, which resides in the NFC, operated smoothly and safely.

Outside of the University of Minnesota, I have been fortunate to interact with many engaging researchers. I have had several excellent conversations with Paul Stradins of the National Renewable Energy Laboratory (NREL) on a wide range of topics over the years. David Bobela, also from NREL, graciously provided ESR and PDS data on some early undoped films that I studied and was very helpful by orienting me and introducing me to people during my first MRS meeting in San Francisco. Jeremy Fields of the Colorado School of Mines was pivotal in beginning a collaboration which resulted in some wonderful measurements on the photoluminescence spectra of a/nc-Si:H films which are described in his thesis. Going back to my undergraduate days, I owe a debt of gratitude to John Colton, who served as my undergraduate adviser, and was the first person to encourage me to go to graduate school. Coming into my undergraduate institution, I had little to no concept of what real research was and honestly had very little passion for physics until John took me on as an undergraduate research assistant. It was that first taste of research that inspired me to dive into physics more deeply and ultimately lead to me graduate school.

Last, but certainly not least, I owe many thanks to my family who has been there with me throughout my graduate school experience. In particular, I owe much to my lovely wife Desirée, who was there to encourage me to work hard when necessary and also there to convince me to take a weekend off when I needed it. Especially in those most difficult years of graduate school, the first and the last year, she was a constant source of support and encouragement. Through our years together, Desirée has also greatly influenced my thinking, helping to transform a simple boy who enjoyed math and science into a person who actually reads the news, thinks about science topics in a broader scope and is more open to new experiences (that means you Nemo, Ophelia and Paul). My brothers, Eric and Kirk, also deserve some thanks, as they provided encouragement during the long years of graduate school and were willing to share in my great enthusiasm for applying physics to the world around us. To my parents, Jan and Mark, what can I say except 'thank you.' You have supported me in whatever I have wanted to do since I can remember and have helped shaped the person I have become. Whether it was virtual trips to Australia or real travels to Germany, you have encouraged me to seek out experiences to make me a better person, lessons that have served me well during the past six years.

**Abstract**

Interest in mixed-phase silicon thin film materials, composed of an amorphous semiconductor matrix in which nanocrystalline inclusions are embedded, stems in part from potential technological applications, including photovoltaic and thin film transistor technologies. Conventional mixed-phase silicon films are produced in a single plasma reactor, where the conditions of the plasma must be precisely tuned, limiting the ability to adjust the film and nanoparticle parameters independently. The films presented in this thesis are deposited using a novel dual-plasma co-deposition approach in which the nanoparticles are produced separately in an upstream reactor and then injected into a secondary reactor where an amorphous silicon film is being grown. The degree of crystallinity and grain sizes of the films are evaluated using Raman spectroscopy and X-ray diffraction respectively. I describe detailed electronic measurements which reveal three distinct conduction mechanisms in n-type doped mixed-phase amorphous/nanocrystalline silicon thin films over a range of nanocrystallite concentrations and temperatures, covering the transition from fully amorphous to ~30% nanocrystalline. As the temperature is varied from 470 to 10 K, we observe activated conduction, multiphonon hopping (MPH) and Mott variable range hopping (VRH) as the nanocrystal content is increased. The transition from MPH to Mott-VRH hopping around 100K is ascribed to the freeze out of the phonon modes. A conduction model involving the parallel contributions of these three distinct conduction mechanisms is shown to describe both the conductivity and the reduced activation energy data to a high accuracy. Additional support is provided by measurements of thermal equilibration effects and

noise spectroscopy, both done above room temperature (>300 K). This thesis provides a clear link between measurement and theory in these complex materials.

**Table of Contents**

**List of Tables**

**List of Figures**

Chapter 4

## Chapter 1

## INTRODUCTION

While single crystal silicon has dominated the microelectronics industry since the 1960s, there are many applications to which it is not particularly suited. For example, thin film silicon is more cost effective for many large area devices, include photovoltaics,[1] switching elements for displays[2] and large area sensors, such as X-ray detectors.[3] In the latter two applications, the active element is typically a thin film transistor (TFT), a type of field effect transistor. The deposition process of thin film silicon enables it to be deposited over large areas and thickness-tuned precisely in order to limit materials losses; the thickness of silicon wafers is limited to hundreds of microns due to the physical limitations of cutting wafers from the silicon crystal ingot. Thin film silicon also has the advantage of being conducive to deposition on a wide variety of substrates, including glass and flexible substrates such as stainless steel[2] and high temperature polymers.[4]

In this thesis, I will present the results of detailed electronic transport studies of mixed-phase silicon thin films. These studies are motivated not only by the technological applications of thin film silicon, but also by interest in elucidating the fundamental transport mechanisms in these complex materials. In this chapter, I will first present a brief introduction to thin film silicon covering both amorphous and mixed-phase silicon. Chapter 2 will focus on a discussion of the relevant electronic transport physics and the previous work which has been presented in the literature. Details of the sample preparation will be described in chapter 3. A variety of experimental techniques have

been brought to bear on this material, which will be outlined in chapter 4. The data and its interpretation, discussed in the framework of current research in the field, will be presented in chapter 5. Finally, the conclusions and future outlook will be presented in chapter 6.

### 1.1 The Basics of Amorphous Silicon

Amorphous materials, despite their great abundance in nature, are a subset of materials that are often overlooked in traditional solid-state courses, due to the difficulty in examining their properties from a theoretical standpoint. In contrast to a crystalline semiconductor, which has a periodic lattice and thus possesses long-range order (LRO), the disordered nature of an amorphous semiconductor disrupts the LRO. The presence of LRO allows one to use Bloch's theorem to describe a crystalline system, wherein electronic states are extended in space and defined by their momentum. Using Bloch's theorem, many properties of crystalline semiconductors can be calculated analytically, as one only has to understand the properties of one periodic unit (8 atoms in the case of crystalline silicon) in order to understand the system, while in amorphous materials, a much larger subset of the material must be considered in order develop an understanding of the material's properties; for amorphous silicon, typically models consisting of thousands of atoms are needed. Among the many differences between amorphous and crystalline materials, perhaps the most important is that momentum is no longer a good quantum number due to the loss of LRO. As a result of the frequent scattering of carriers in an amorphous solid, where the scattering length is often on the order of the interatomic

spacing, a large uncertainty in momentum is introduced. This has several important consequences, such as relaxing the momentum selection rules for optical transitions and the inability to define an energy-momentum dispersion relation for the electronic energy bands.[5]

Fluids are disordered materials, but are more easily treated than amorphous materials, as they are in thermal equilibrium and can be described using traditional statistical mechanics. Amorphous materials are not in a true equilibrium, but rather a metastable equilibrium, with the crystalline phase being the lowest energy state. Because they are out-of-equilibrium materials, they must be produced in processes such as melt quenching or vapor deposition, where the atoms do not have sufficient time or energy to reach their global equilibrium (the crystal phase) during growth or cooling. Fluids are able to reach their equilibrium state due to the relatively weak nearest neighbor interactions they possess compared to amorphous materials. The stronger nearest neighbor interactions in amorphous materials impose short-range order (SRO), which is lacking in fluids, resulting in large energy barriers between the metastable states and the true minimum energy state. In tetravalent amorphous silicon, the atomic positions are tightly constrained by the requirements for $sp^3$ hybridization. The average bond length (2.35 Å) is the same (to within ~ 1%) as in crystalline silicon, with the main disorder being in the bonding angle between nearest neighbors, which has a spread of ~10° around the mean value of 109.5°, the same as in crystalline silicon.[6] Dihedral angle variations in amorphous silicon are on the order of 35%, and account for the loss of LRO in these materials. The similarities in the properties of amorphous semiconductors with their

crystalline counterparts are due to their common SRO, while the differences are generally due to the lack of LRO in amorphous materials.

The scale over which amorphous silicon exhibits order has been discussed for many years. Until recently, researchers believed that amorphous silicon was best represented by a continuous random network (CRN) model, where SRO is present but very little medium range order (MRO) on the scale of 1 – 3 nm exists.[7] In general, simulations using models of CRNs have been able to reproduce structural data such as the radial distribution function (RDF) obtained via electron diffraction, Raman and the vibrational density of states measured with neutron diffraction.[8–12] Recent evidence has thrown doubt on the applicability of the CRN model for amorphous silicon, most notably from fluctuation electron microscopy (FEM) measurements, one of the few techniques that is capable of explicitly probing MRO.[13–17] In FEM, the normalized variance of the image obtained via electron microscopy is analyzed rather than the average intensity.[18,19] FEM is much more sensitive to structural ordering than techniques that measure average values, such as diffraction, where incomplete ordering is lost in the averaging process. Recent evidence suggests a paracrystalline model[20] may be a more accurate representation of the microscopic structure of amorphous silicon. The paracrystalline model posits that small, strained grains less than 1 – 2 nanometers in size are embedded in the amorphous matrix, introducing substantial medium range order (MRO), which is reflected in the FEM data. Treacy and Borisenko have found that the paracrystalline model fits the FEM data much better than the CRN model and can also effectively reproduce other structural data, such as the RDF.[14] The application of these new

paracrystalline models to other measurements will undoubtedly be an area of increasing research in the coming years.

Intimately connected to the physical structure of amorphous silicon is the electronic structure, typically represented using the single electron density of states (DOS). Any discussion of electronic transport must be interpreted through the lens of the DOS of the material. The DOS of an amorphous semiconductor is best understood in comparison to its crystalline counterpart, depicted in figure 1.1. A crystalline semiconductor has the standard valence band and conduction band states, with sharp band edges and virtually no states in the forbidden gap region; any states that are found in the gap region are discrete states with a small energy width. States in the bands are delocalized or extended states, while gap states are localized states, states which are confined to particular spatial location. Amorphous semiconductors possess a similar DOS, but lack the sharp features of a crystalline semiconductor. The band edges are 'smeared' to produce band tail states (one for each band) that decay exponentially with energy into the gap, while the defect states are broadened by disorder into distributions of defects. Due to the band smearing, there is no longer a clear band edge in amorphous semiconductors and instead the term 'mobility edge' is used, which is the demarcation energy between localized and delocalized states.[5]

The band tail (BT) states in a-Si arise from strained silicon-silicon bonds, with the valence BT state distribution being approximately twice as wide as that of the conduction BT. Simulations indicate that bonds which are too short (long) correspond to states in the valence (conduction) BTs.[21] The reason for the exponential energy dependence of the

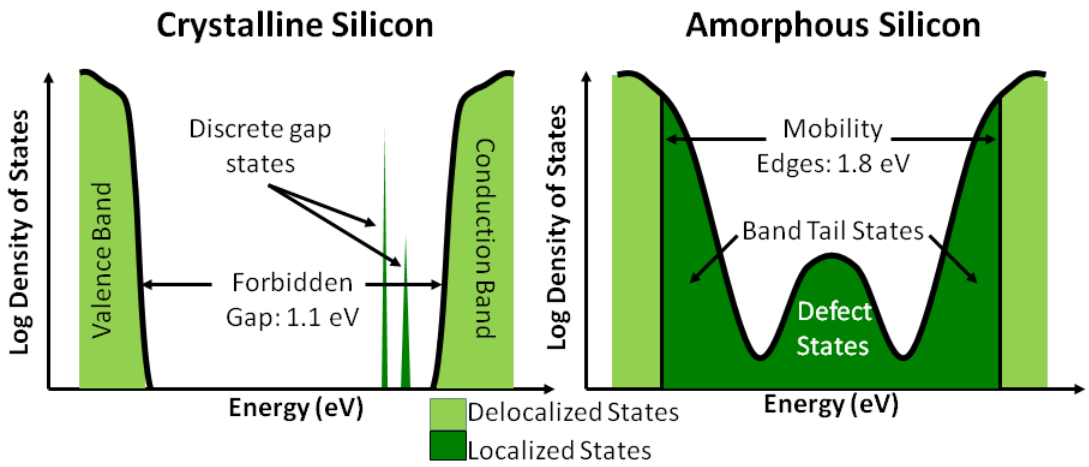


Figure 1.1: Sketch of the density of states (DOS) for both crystalline silicon (left) and hydrogenated amorphous silicon (a-Si:H) (right). The sharp band edges and discrete states of crystalline silicon are broadened in a-Si:H by the disorder of the amorphous structure.

BTs, rather than a Gaussian shape as is typically assumed in disordered induced broadening, has been debated for many years, with recent simulations pointing to the creation of correlations between the distorted bonds.[22] These correlations tend to produce filamentary structures that are nucleated from a central, most heavily distorted bond and whose distortion decays to equilibrium with increasing distance from the central bond.[23] While generic amorphous silicon models have for many years accurately reproduced the band tails observed,[24] the physical location of the electronic states has not been clearly identified until recently. In the work of Drabold *et al*,[25] it was found that by imposing conditions such that no filaments were generated, exponential band did not form, lending

support to the filament model for BT states. Recent work by Smets *et al*[26] has shed light on the reason for the difference in valence and conduction BT widths using a model of amorphous silicon where the structure is dominated by divacancies and nanovoid defects. Based on these calculations, the divacancy defect leads to an asymmetric distribution of distorted bonds, with there being more short bonds than long bonds. Given the assignment of short (long) bonds to the valence (conduction) BTs,[21] this would provide a self consistent explanation for the differing BT widths.

In a crystalline semiconductor, any deviation from a perfect lattice can be regarded as a defect and can be readily measured and quantified, while the inherent disorder of amorphous semiconductors does not allow for such a clean distinction. Generally, in amorphous semiconductor, a defect is regarded as a localized state within the mobility gap and is considered distinct from the states in the BTs. Until recently, it was assumed that most defects were coordination defects; as in the case where an atom is either missing a bond or has an additional bond compared to what its valence shell filling would normally dictate. In amorphous silicon, which is tetravalent, a *dangling bond* is formed when a silicon atom has only three covalent bonds with its nearest neighbors and a *floating bond* is formed when five bonds are forced on the silicon atom,[27] with the dangling bond being the most common in amorphous silicon. The coordination defects in a-Si (and in a-Si:H) can be in one of three charge states; neutral (singly occupied), negatively charged (doubly occupied) or positively charged (unoccupied). The large density of localized states in a-Si:H, both in the band tails and the gap, degrades the transport properties compared to crystalline silicon. The free-carrier mobilities are much

lower, resulting in lower conductivity values and poorer device performance when compared to similar devices prepared with crystalline silicon wafers.

Recent work has revealed a more complicated picture of mid-gap states than the simple band tail/dangling bond model sketched above. Simulations suggest that many mid-gap states may actually be due to highly strained silicon-silicon bonds, states that are more strained and thus more localized than those ascribed to BT states,[28,29] in addition to the coordination defects observable via electron spin resonance (ESR). Many of these highly strained bonds were found to be more effective traps for free charge carriers than dangling bonds.[28] Work by Smets *et al* suggests that defects primarily are located at divacancies in a-Si:H,[30] which could take on many different configurations depending on the local hydrogenation and possible bond reconstructions, resulting in a spread of defect energies. The divacancy dominated view of a-Si:H has been successful in explaining the hydrogen bonding spectrum observed in infrared spectroscopy and the relationship between hydrogen bonding and film density.[30–32]

The inclusion of hydrogen in amorphous silicon, forming hydrogenated amorphous silicon (a-Si:H), substantially reduces the density of dangling bond states in the mid gap region (from ~$10^{19}$ $cm^{-3}$ in unhydrogenated material to $10^{15}$ $cm^{-3}$ in high quality a-Si:H), as well as removes many strained Si-Si bonds, reducing states in the band tails such that they exhibit a steeper energy dependence. Without the inclusion of hydrogen, amorphous silicon could not be doped, as the high density of mid-gap states in a-Si strongly pins the Fermi level. The pinning of the Fermi level also limits the utility of unhydrogenated a-Si in electronic devices, such as thin film transistors or photovoltaics, which both depend on

the ability of some external stimulus to move the Fermi level. Hydrogen also has the effect of increasing the gap of amorphous silicon (to ~1.8 eV) compared to unhydrogenated amorphous silicon (~1.2 eV); this is believed to be due to the increased strength of the silicon-hydrogen bond as compared to the silicon-silicon bond.[33,34]

In the earlier years of amorphous semiconductor research, it was expected that the lack of topological constraints in amorphous semiconductors would prevent substitutional doping of these materials. It was therefore surprising when Spear and LeComber demonstrated both n- and p-type doping in a-Si:H in their seminal 1975 paper, where they were able to change the room temperature conductivity of a-Si:H by approximately ten orders of magnitude by chemically doping a-Si:H.[35] Doping occurs in a crystalline semiconductor when the host lattice forces an impurity (dopant) atom into a coordination that leaves either an unbonded electron or a missing electron, called a hole, in the bonding structure; these two configurations produce donor and acceptor states, respectively. Without an ordered lattice to force a particular coordination on an impurity atom, one would naively expect a phosphorus atom to remain three-fold coordinated in amorphous silicon rather than become four-fold coordinated and donate an electron, which is expressed by Mott as the 8-N rule.[36] The nature of doping in amorphous semiconductors is fundamentally different from that in crystalline semiconductors, as reflected in a reduced doping efficiency (compared to crystalline silicon) and noticeable effects in the temperature dependence of the conductivity, collectively known as thermal equilibration effects.[37,38] Details of the doping mechanism will be discussed in the next chapter in the context of thermal equilibration.

No discussion of a-Si:H would be complete without mention of the Staebler-Wronski effect (SWE), wherein defects are generated in a-Si:H upon exposure to light;[39] these defects serve to lower the conductivity,[39] reduce solar cell efficiencies[40] and increased threshold voltages for thin film transistors.[41] The defects can be removed following a high temperature anneal (~450K). The effect was originally observed in 1977 by Staebler and Wronski and while there has been great progress in understanding this effect, a complete explanation does not exist.[42–44] In most theories of the Staebler-Wronski effect, hydrogen diffusion is proposed as the enabler or catalyst of the defect creation. There are many interesting and sometimes apparently contradictory aspects of the SWE; for instance, the effect itself results not only from light exposure as was originally observed, but from any non-radiative recombination of excess charge carriers, such as occurs in double injection of a $p^+$-p-$p^+$ structure.[45] Furthermore, the efficiency with which these defects are created does not depend appreciably on temperature,[46] a surprising result if long-range hydrogen diffusion is involved given the strongly activated nature of hydrogen diffusion in a-Si:H.[47] Fritzsche has argued that the heterogeneous nature of a-Si:H complicates the elucidation of the SWE mechanism,[48] with recent experiments pointing to the possible existence of multiple kinds of light induced defects (LIDs), each with different characteristic annealing times and capture cross sections.[49,50] Smets posits that these defects are related to the different configurations of the divacancy defect in a-Si:H,[51] while simulations by Wagner and Grossman[28] implicate highly strained bonds as a possible source for the defects responsible for the SWE. Experiments by Bobela *et al*[52] found that annealing samples at relatively modest

temperatures (350 – 400ºC) dramatically reduces the creation of LID with only minimal hydrogen loss. These new results will hopefully lead to a clearer understanding of the nature of the SWE in the coming years.

### 1.2 Introduction to Mixed-Phase Silicon

Due to the aforementioned Staebler-Wronski effect (SWE) and the generally poor transport properties of a-Si:H compared to crystalline silicon, most notably short photocarrier lifetimes and low mobilities, there have been substantial efforts to create a form of thin film silicon that can be produced using large area processes at low temperatures (<250°C) but which also possesses superior opto-electronic properties. The thin film silicon field is moving in the direction of mixed-phase silicon, which has been reported to both be resistant to the SWE and have significantly improved transport properties.[53] Mixed-phase silicon consists of a matrix of hydrogenated amorphous silicon that contains small semiconductor nanocrystallites, typically 3 – 20 nm in diameter. A cartoon depiction of the structure of mixed-phase silicon is presented in figure 1.2. In addition to the amorphous and nanocrystalline phase, often a third phase is considered, namely the grain boundary region that separates the nanocrystalline grains from the amorphous matrix or that exists between adjacent nanocrystallites. Due to the disordered structure of the material, vacancies (1 – 2 missing silicon atoms) and voids (up to a few nanometers) are also present, playing an important role in the electronic structure of the material.

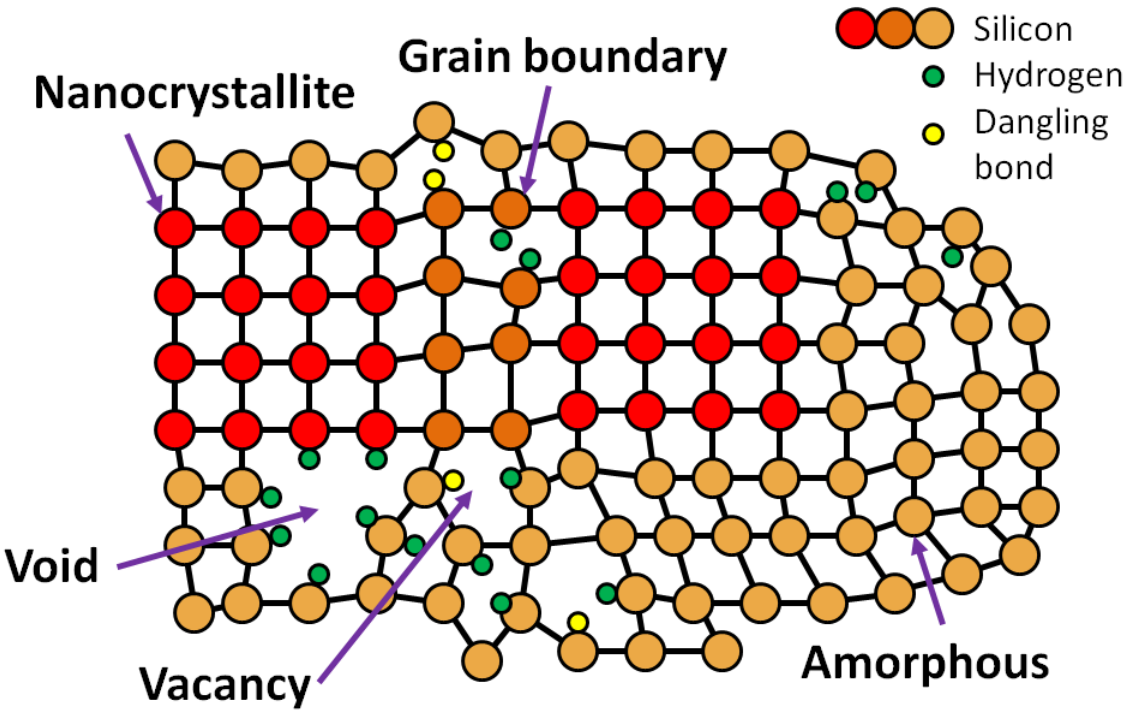


Figure 1.2: A cartoon depiction of mixed-phase silicon, including the amorphous and nanocrystalline phase, as well as the grain boundary region between the two phases or adjacent nanocrystallites. Void and vacancy structures also exist within the material and further complicate its structure in addition to adding dangling bond defects, while hydrogen serves to passivate some of these defects.

Experiments have found that charge transport occurs primarily through the nanocrystalline material for samples with crystal fractions above the percolation threshold,[54–56] with a few reports of enhanced transport properties before the onset of percolation,[57] implying there may be significant changes to the amorphous matrix simply due to the incorporation of nanocrystallites. In addition to the general improvement of

the transport properties from the nanocrystalline inclusions, a few other key differences should be discussed. The doping mechanism within the nanocrystallites has been shown to be via traditional substitutional doping, with nearly 100% electrical activation of incorporated dopants just as in crystalline silicon.[58] The hydrogen microstructure is also sometimes observed to be different in mixed-phase materials compared to a-Si:H, with changes in the distribution in hydrogen reflected in changes in silicon-hydrogen vibrational frequencies and a sharpening of infra-red absorption lines.[59] The heterogeneous nature of mixed-phase silicon means that one can no longer consider a single spatially uniform DOS, but rather a material in which each component (nanocrystalline, amorphous and grain boundary) has its own distinct DOS and transport properties.

Mixed-phase silicon has been ascribed many different names throughout the years – microcrystalline silicon (μc-Si:H), nanocrystalline silicon (nc-Si:H), protocrystalline silicon (pr-Si:H) and polymorphous silicon (pm-Si:H). Sometimes the differences between these materials is arbitrary, as in the case of μc-Si:H and nc-Si:H, while at other times the different terms represent materials grown via significantly different processes, as is the case with pm-Si:H. For our materials, synthesized in a co-deposition process, we employ the term a/nc-Si:H to emphasize that the a-Si:H and nc-Si are produced in separate reactors. This also serves to highlight the mixed-phase nature of the material, not evident in the terms μc-Si:H and nc-Si:H which are used to describe materials covering a wide range of crystalline volume fractions.

## Chapter 2

## ELECTRONIC TRANSPORT

### 2.1 Introduction to the Basic Conduction Mechanisms

In semiconductors, at temperatures where there is ample thermal energy, the dominant form of conduction is thermal activation of charge carriers across the band gap into empty extended states within the bands. In amorphous semiconductors this implies activation across the mobility edge that separates localized from delocalized states. Activated conductivity is described by an Arrhenius relationship:

$$\sigma_{ACT} = \sigma_0 \exp\left[-E_A / k_B T\right] \tag{2.1}$$

where the activation energy $E_A$ is the energy difference between the Fermi level and the mobility or band edge. For hydrogenated amorphous silicon (a-Si:H), $E_A$ generally lies between 0.2 – 0.8 eV, depending on the doping level and quality of the material.[5] Doped a-Si:H (and to a lesser extent, undoped a-Si:H) display an apparent change in the conductivity's activation energy due to the thermal equilibration of the defect and dopant states;[37] this occurs near 400 K for n-type doped a-Si:H and will be discussed in greater detail in the next section.

As the temperature decreases, hopping conduction begins to dominate; characterized by charge carriers that spend most of their time localized on particular sites in real space and periodically move or 'hop' to nearby localized states. The hopping rate is determined by both the energy difference between the sites and the wavefunction overlap, which is governed by the distance between the sites and the localization length of the states. An energy difference between the sites typically requires the absorption or

emission of a phonon. When there is sufficient thermal energy such that spatial distance between the sites is the most important factor for hopping, charge carriers will always hop to the state that is closest in real space; known as nearest neighbor hopping (NNH). NNH leads to an Arrhenius temperature dependence for the conductivity, similar to transport through extended states, though typically with smaller activation energies (< 0.2 eV). This energy scale can be thought of as the average phonon energy employed per hop.

At lower temperatures where charge carriers in localized states lack sufficient energy to always hop to the nearest neighbor, variable range hopping (VRH), first described by Mott,[36] begins to dominate the conduction. A state further away in real space may have a smaller energy difference than a nearest neighbor site, and the competing costs of energy and distance must be minimized. Using a simple argument, the Mott-VRH law can be derived to be:[36]

$$\sigma_{VRH} = \sigma_0 \exp\left[-\left(T_0 / T\right)^x\right] \qquad (2.2)$$

Where $\sigma_0$ is the conductivity prefactor and $T_0$ is a characteristic energy scale determined by the density of states (DOS) at the Fermi level ($\varepsilon_F$). The exponent $x$ is determined by both the dimensionality of the system and the shape of the DOS near $\varepsilon_F$; in the case of Mott-VRH, the DOS is assumed to be constant at $\varepsilon_F$, leading to $x$ = ¼ in three-dimensions. Variations to the shape of the DOS can result in different values for $x$, such as ½ in the case of a parabolic DOS in three dimensions, commonly referred to as Efros-Shklovskii VRH (ES-VRH).[60] Localized states near the edges of the conduction band are found to have a density that decreases exponentially with energy, $g(\varepsilon) \sim \exp[-\varepsilon/\varepsilon_c]$, where

$\varepsilon_c$ sets the energy scale for the decrease of the density of localized states near the conduction band ($\varepsilon_v$ would be used for the localized states near the valence band edge). Theoretical work by Godet[61,62] has shown that VRH through exponential band tail (BT) states, which we will refer to as Exp-VRH to distinguish it from Mott- or ES-VRH, results in a temperature dependent conductivity with a similar form:

$$\sigma_{VRH} = \sigma_0 T^{1/2} \exp\left[-\left(T_0/T\right)^{1/4}\right] \tag{2.3}$$

where the dominant temperature dependence in the exponent is the same as in Mott-VRH. The argument leading to an exponent of ¼ for Exp-VRH is based on the dimensionality of the problem and is an extension of earlier work by Grünewald and Thomas,[63] who introduced the concept of a transport energy above the Fermi level at which conduction predominantly occurs. As the temperature increases, the transport energy moves up the exponential distribution into a region with a higher DOS, resulting in a shorter average hopping distance.

From either Mott- or Exp-VRH, an estimate of the DOS at the Fermi level, $g(\varepsilon_F)$, can be obtained from $T_0$. As has been reported by several others, estimates of the DOS obtained from Mott-VRH are often inconsistent with other measurements of $g(\varepsilon_F)$ or result in unphysical values.[64,65] For Exp-VRH, Godet calculates the relationship between $T_0$ and $g(\varepsilon_F)$ to be:[62]

$$g(\varepsilon_F) = \frac{310}{k_B T_0 \alpha^3} \tag{2.4}$$

where $\alpha$ is the electron localization radius and $k_B$ is Boltzmann's constant. The numerical factor of 310 in eqn. 2.4 arises from fits by Godet of $T_0$ against $g(\varepsilon_F)\alpha^3$, where $g(\varepsilon_F)\alpha^3$ is

referred to as the localization parameter.[62] These data are calculated using a model of transport in BT states, where the localization parameter is varied and the temperature dependent conductivity is calculated. From an experimental standpoint, $T_0$ values derived from fits to the conductivity data and estimates of $\alpha$ obtained from other measurements enable a determination of $g(\varepsilon_F)$.

In the previously discussed forms of hopping, NNH and all types of VRH, it is assumed that the energy needed per hop is obtained from only a single phonon. For strongly localized states, this is likely true. When hopping occurs between states that are partially delocalized (possessing a large localization length), there exists the possibility to use multiple phonons per hop. This process is termed multi-phonon hopping (MPH) and typically results in a power-law temperature dependence of the conductivity. Power-law behavior attributed to MPH has been observed in several other systems containing structure on the nanoscale, including metal-oxide glasses,[66] defect/void structures in amorphous germanium,[67] localized bonds in amorphous carbon,[68,69] and grain boundary states in nanocrystalline diamond.[70] In the standard description of MPH,[67,68,71] electrons are weakly localized and, due to weak electron-lattice interactions, preferentially couple to phonons with wavelengths close to the electron's localization length, i.e. long wavelength acoustic phonons. A charge carrier may require multiple long-wavelength, low energy phonons in order to complete a given transition. Robertson and Friedman[71] calculated the rate $\Gamma$ for such multi-phonon transitions in the context of the relaxation of charge carriers after optical excitation to be:

$$\Gamma = \left(\nu_0 \exp[-2s/\alpha]\right)\left(\exp\left[-\frac{E_M}{h\nu_0}\right]\right)\left(\frac{E_M}{h\nu_0}\right)^p \left[1 + n_{BE}(\nu_0)\right]^p \qquad (2.5)$$

where $p$ is the average number of phonons required, $s$ is the edge-to-edge distance between hopping sites, $\alpha$ is the localization radius, $E_M$ is a measure of the electron-phonon coupling and $n_{BE}(\nu_0)$ is the Bose-Einstein distribution for phonons with a frequency $\nu_0$. It is this last term in eqn. 2.5, $[1 + n_{BE}(\nu_0)]^p$, which dominants the temperature dependence. This factor (rather than $[n_{BE}(\nu_0)]^p$) results from the rate-limiting step being the emission of $p$ phonons, as was the case for the conditions examined by Robertson and Friedman, where the charge carriers were already in excited states following optical pumping. For the dark conductivity, the rate limiting step is the absorption of $p$ phonons to hop to a state higher in energy, necessitating the use of $[n_{BE}(\nu_0)]^p$. This results in a hopping rate of the form:

$$\Gamma = \left(\nu_0 \exp[-2s/a]\right)\left(\exp\left[-\frac{E_M}{h\nu_0}\right]\right)\left(\frac{E_M}{h\nu_0}\right)^p \left[n_{BE}(\nu_0)\right]^p \qquad (2.6)$$

When emission is the limiting step (eqn. 2.5), the hopping rate asymptotically approaches a constant at low temperatures, an unphysical effect for the dark conductivity of a semiconductor. Eqn. 2.6, where the $[1 + n_{BE}(\nu_0)]^p$ term has been replaced by $[n_{BE}(\nu_0)]^p$, displays the correct temperature dependence – a conductivity that goes to zero at low temperatures when there are insufficient phonons for the transition. Using the standard expression for hopping transport[72] and substituting eqn. 2.6 for $\Gamma$, we can express the conductivity due to MPH as:

$$\sigma_{MPH} = \frac{e^2 r^2 n_c}{6 k_B T} \Gamma \tag{2.7a}$$

$$\sigma_{MPH} = \frac{e^2 r^2 n_c}{6 k_B T} \left(\nu_0 \exp[-2s/a]\right) \left( \exp\left[ -\frac{E_M}{h\nu_0} \right] \right) \left( \frac{E_M}{h\nu_0} \right)^p \left[ n_{BE}(\nu_0) \right]^p \tag{2.7b}$$

Here $r$ is the center-to-center distance between nanocrystallites, $e$ is the electron charge and $n_c$ is the density of charge carriers. As transport occurs via weakly localized electrons with a large localization radius, one must distinguish the center-to-center distance of the sites ($r$), which controls the effective distance hopped, from the edge-to-edge distance ($s$) that determines the wavefunction overlap. Figure 2.1 illustrates this difference; for mixed-phased silicon, which consists of a mixture of nanocrystallites in an amorphous matrix, we expect that the hopping will occur between ncs, where the hopping state is a partially delocalized electron confined to a single nc.

Previous experimental observations of multi-phonon hopping have been in the regime of $k_BT >> h\nu_0$, which simplifies the phonon factor in either eqn. 2.5 or 2.6 to a simple power-law. For our samples, where a transition from VRH to MPH is present, we expect $k_BT \sim h\nu_0$ over a considerable temperature range, requiring the use of the full expression (eqn. 2.7b) in order to provide an accurate description of the data.

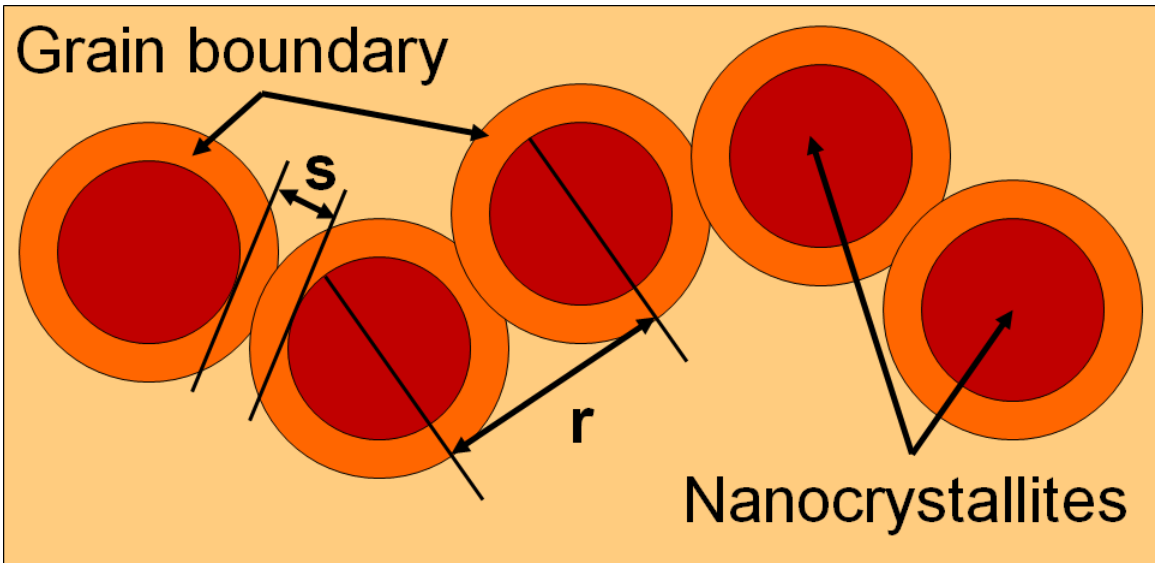


Figure 2.1: Cartoon sketch of several nanocrystallites, illustrating the differences between the multi-phonon hopping parameters in eqn. 2.7b. *s* is the edge-to-edge distance, which affects the wavefunction overlap term, while *r* is the center-to-center distance that affects the total effective distance that is traversed with each hop. The electrons are assumed to be delocalized within the nanocrystalline grains, but confined to the grains.

## 2.2 Doping and Thermal Equilibration

The mechanism by which doping occurs in the absence of topological constraints (as in a-Si:H) was explained when Street introduced the concept of a thermodynamic equilibration between dopant states and defect states. He proposed that doping can be viewed as a chemical reaction between neutral dopant atoms and ionized dopant atom/charged defect pairs. Considering the case of phosphorus, this is described as:[73]

$$Si_4^0 + P_3^0 \Leftrightarrow P_4^+ + D^- \qquad (2.8)$$

Where the superscript refers to the charge and the subscript refers to the coordination. A

$D^-$ is a negatively charged (doubly occupied) dangling bond, which could also be represented as $Si_3^-$, but conventionally is denoted by $D^-$. The key point of Street's theory is that an ionized phosphorus atom, with only four valence electrons, would naturally be four-fold coordinated, while a neutral phosphorus atom would remain three-fold coordinated in an amorphous matrix. By creating a charged under-coordinated defect at the same time as an ionized over-coordinated dopant, the energy cost of incorporating a four-fold coordinated phosphorus atom can be substantially reduced, explaining the observed correlation between charged defects and doping.[74] In compensated a-Si:H, the acceptor plays the role of the charged defect, ionizing the donor such that it can be four-fold coordinated without the need for an accompanying defect. At a given temperature, a thermodynamic equilibrium is established between the left and right sides of eqn. 2.8, leading to both ionized dopant/defect pairs and neutral dopants that maintain their preferred coordination. Due to the finite width of the Fermi-Dirac distribution, which defines the occupancy of electronic states, some electrons will be excited into the band tail (BT) states. A charge carrier which is donated by an ionized phosphorus atom must exist either as a negatively charged defect or in an occupied BT state, giving us:

$$n_{P_4^+} = n_{BT} + n_{D^-} \tag{2.9}$$

where the $n$ is the number density and the subscript denotes the state. The density of four-fold coordinated phosphorus atoms is roughly ten percent higher than that of negatively charged dangling bonds. At higher temperatures, more phosphorus atoms will become ionized, increasing the equilibrium density of both the occupied BT states and charged defects. As it is the occupied BT states that contribute to the conductivity in

doped a-Si:H, changes in these states are readily observed in the conductivity.

The time to reach equilibrium increases exponentially with decreasing temperature and is governed by the energy barrier between configurations, measured in a-Si:H to be ~1 eV.[75] We can define a temperature, $T_E$, above which the states are in equilibrium and below which the density of states (DOS) is effectively frozen. The exact $T_E$ is defined by the observation time, which is typically taken to be ~100 s. Much of the language and physics involved in thermal equilibration is borrowed from the field of melt-quenched glasses. A glass at high temperatures is in equilibrium and as it is cooled, at some point it will no longer be able to maintain equilibrium, resulting in a change in one or more properties; usually there is a discontinuous change in a derivative of a thermodynamic property with no latent heat. This temperature is called the glass transition temperature, $T_G$, and is analogous to $T_E$.

In a-Si:H, thermal equilibration manifests itself as a 'kink' in an Arrhenius plot of the conductivity data – above $T_E$, there is a larger activation energy than below $T_E$. Above $T_E$, the defect states and dopant states can remain in equilibrium, which forces the Fermi level to sit in a minimum between the $D^-$ states and the occupied BT states in order to maintain charge neutrality, as illustrated in figure 2.2. If the temperature is raised, more defect/ionized dopant pairs will be created, keeping the Fermi level in the minimum of the DOS. Below $T_E$, the DOS is effectively frozen and in order to maintain charge neutrality, the Fermi level must move closer to the band edges due to the occupancy of the BT states, which is a convolution of the reducing width of the Fermi-Dirac function and the steep DOS in the BTs; this is known as a *statistical shift*. It appears as an abrupt

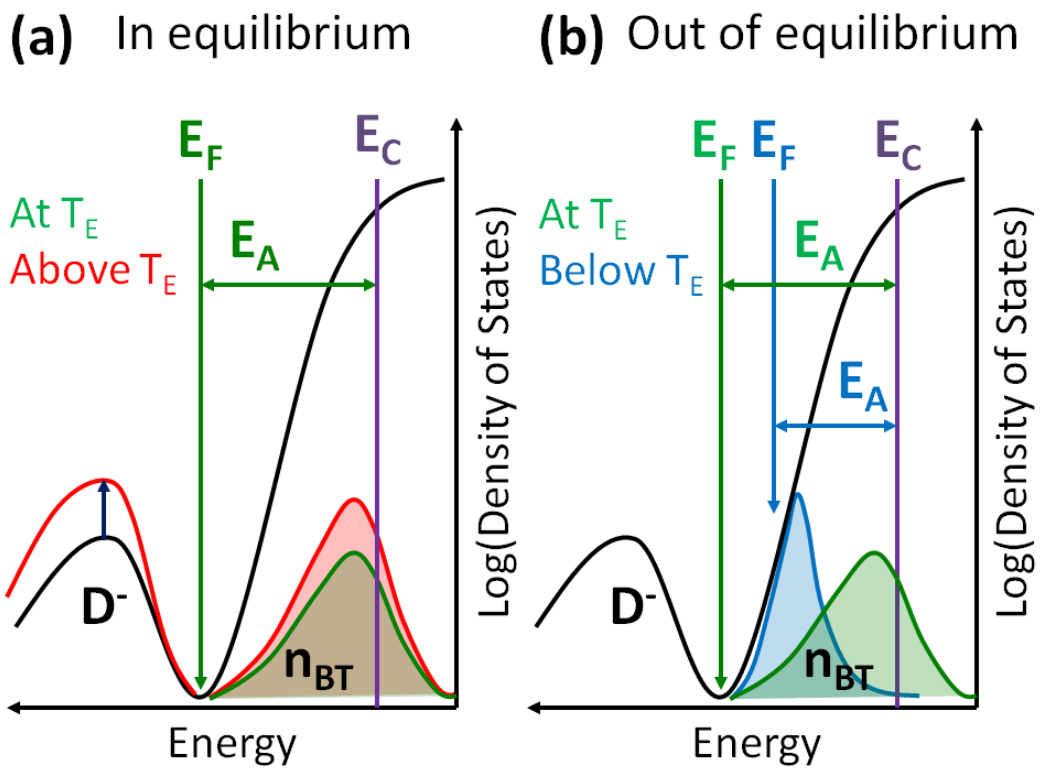


Figure 2.2: A sketch of the density of states of a-Si:H illustrating the mechanism of thermal equilibration in doped a-Si:H. (a) At high temperatures, where the material is in equilibrium, the density of states (DOS) adjusts in order to keep the Fermi level in the minimum between the $D^-$ states and the occupied band tail states ($n_{BT}$), maintaining charge neutrality. If there is an increase in temperature (red), more defect states/ionized donors are created, but the Fermi level's position in the mobility gap remains fixed. For clarity, the ionized donor states are not shown. (b) As the temperature is lowered and the relaxation time increases, the DOS can no longer maintain equilibrium and becomes effectively frozen. Now the Fermi level must shift closer to the conduction band (blue) as the temperature is lowered in order to maintain charge neutrality due to the Fermi-Dirac distribution's decreasing width and the steep slope of the DOS in the band tails.

kink rather than a slow transition, because the shift is a highly non-linear change due to the exponential dependences involved (the width of the band tails and the Fermi-Dirac function). Because of its intimate connection to the metastability of amorphous materials, thermal equilibration should not exist in pure nanocrystalline silicon and can thus provide a means to distinguish between activated transport occurring in the amorphous or nanocrystalline phase of the material.

### 2.3 Noise Spectroscopy in a-Si:H and a/nc-Si:H

Noise spectroscopy examines the fluctuations of a given quantity, in our case the electronic current, about a mean value. By measuring and statistically analyzing these fluctuations, information can be obtained about the underlying microscopic processes. Noise spectra are often categorized by their frequency dependence, with typical examples being white noise, where the noise level is frequency independent, and $1/f$ noise, where the noise magnitude is inversely proportional to the frequency. In electronic systems, white noise may be due to Johnson noise (aka thermal noise),[76] reflecting the random thermal motions of charge carriers, or from shot noise, which arises due to the discrete nature of charge carriers;[77] both of these noise sources are fundamental in nature and cannot be removed. In contrast, $1/f$ noise is not fundamental and can be reduced, but rarely eliminated, by proper materials and device engineering.[78–83] Nevertheless, $1/f$ noise is a nearly ubiquitous form of noise, occurring in almost every electronic system, including transistors[80] and even many simple resistors.[84] The $1/f$ noise in a system is often indicative of traps or defects in the material, but the exact mechanisms that leads to

1/*f* noise are not universal and vary from system to system. For two excellent reviews on 1/*f* noise in solid state physics, the reader is referred to the papers by Weissman[85] and Dutta and Horn.[86] In thin film silicon, it is primarily the 1/*f* noise that is of interest.

Noise spectroscopy has a rich history in amorphous silicon; starting in the 1980s, the noise properties of a-Si[87] and a-Si:H[88,89] began to be studied. In these early investigations, researchers examined only the power spectrum, derived from the two-point correlation function. If the fluctuations are Gaussian, then all relevant information is contained in the power spectrum. For non-Gaussian noise, that is, noise with higher order correlations, other statistical tests, such as the second spectrum or correlation coefficients, must be used. Highly non-Gaussian noise in the form of random telegraph signal noise (RTSN) was first noted in 1990 by Choi *et al* in p+ doped samples using a transverse geometry.[90] In 1991, Parman *et al* reported the observation of RTSN in n-type doped a-Si:H samples in a coplanar geometry, as well as other highly non-linear characteristics to the noise.[91,92] RTSN arises in systems where a few key fluctuators have a large effect on the total conductance of the system and is typically observed in very small samples or devices, such as nanoscale transistors,[93–96] where electron traps in the oxide layer modulate the conductivity of the channel, and silicon nanowires,[97] making the observation of RTSN in coplanar a-Si:H surprising. Work by Parman *et al*[98,99] and Khera and Kakalios[100,101] explored the non-Gaussian properties of this noise, characterizing it extensively. Following these studies, groups at the University of Chicago,[102] the University of Saskatchewan[103–107] and the University of Utrecht[108–110] have all studied noise in a-Si:H, both doped and undoped, and measured a range of noise properties,

depending on a variety of parameters. A 2002 review of noise spectroscopy in a-Si:H summarizes these studies.[111]

Compared to the large amount of work on noise spectroscopy in a-Si:H, the noise properties of mixed-phase silicon has received significantly less attention. A few works have been presented on mixed-phase materials, where a trend of decreasing noise power with increasing crystal fraction has been reported.[112] These authors observe a dramatic reduction in the noise power during the transition from a-Si:H to polymorphous silicon, with a more modest decrease in the noise power as the material's crystallinity further increases. The temperature dependence and Gaussian character of the noise is unexplored. Only one paper to date has addressed the Gaussian nature of the noise signal, where it was found that the noise in μc-Si:H was Gaussian in the temperature range of 300 – 500K.[113] As our samples span a regime where the conduction channel likely switches from the amorphous to nanocrystalline phase,[56] we are in a unique position to study the change in the higher order statistics as the electronic transport channel shifts.

### 2.4 Transport in Mixed-Phase Silicon

Due to its complicated structure and heterogeneous nature, the study of transport in mixed-phase silicon remains an active area of research. To date, there are numerous studies of charge transport in mixed-phase silicon – in order to provide context for the present work, we shall briefly review the field. The simplest conduction mechanism that is invoked to explain conductivity data is activated conduction, often with multiple

activation energies. Müller *et al*[114] studied n-type doped, highly crystalline samples, with a crystal fraction ($X_C$) > 90%, and used both a high and low temperature activation energy to fit their data. Lof and Schropp[115] attempted to explain conduction in undoped, mixed-phase silicon films by assuming activated transport with a strong statistical shift of the Fermi level. This work focused mainly on the dependence of the conductivity on $X_C$, mostly ignoring the temperature dependence. Our group has previously reported the effect of relatively small amounts of nanocrystalline inclusions ($X_C$ < 20%) on the conductivity of undoped a/nc-Si:H films, finding the conductivity to be activated, but with a large enhancement in the conductivity and reduction in the activation energy for films with $X_C$ = 2 – 4%.[116] A model involving competition between charge donation by the nanocrystallites and defects induced in the deposition process was proposed.

Hopping and tunneling conduction are perhaps the most commonly reported electronic transport mechanisms in mixed-phase silicon thin films. Often, a temperature dependence of $\sigma \sim \exp[-(T_0/T)^x]$ is reported, with $x$ = ¼ or ½. For example, in the work of Concari *et al*,[117] the conductivity was observed to follow $\sigma \sim \exp[-(T_0/T)^{1/4}]$ in undoped and lightly p-type silicon thin films, which they found to be in agreement with Godet's model of hopping in exponential band tails.[61,62] The same temperature dependence was reported in undoped, highly crystalline films ($X_C$ > 70%) by Ambrosone *et al*,[118] who interpreted their results in the framework of traditional Mott-VRH.[36] The work of Dussan and Buitrago[119] also concluded that Mott-VRH is the active transport mechanism in lightly p-type samples below room temperature. While their crystal fractions are not reported, based on the $H_2/SiH_4$ ratio during deposition, one would expect their films to

have a substantial amorphous component.[120] For undoped samples with $X_C$ ranging from 45 – 65%, Qin *et al*[121] reported conductivity data that was well described by Mott-VRH. Di Nocera *et al*[122] found their data on heavily doped mixed-phase silicon was well fit by a VRH expression, but the parameters extracted from the fit were unphysical, particularly the density of states at the Fermi level which was calculated to be ~$10^{24}$ $eV^{-1}cm^{-3}$. Consequently, they proposed a theory based on the existence of two parallel tunneling mechanisms through the grain boundary region, though the offsets employed between the bands of the nanocrystalline and amorphous phase are considerably different from previously measured values.[123]

Rafig and coworkers[124] observed $\sigma \sim \exp[-(T_0/T)^{1/2}]$ in undoped, fully crystalline nc-Si:H, which is normally ascribed to Efros-Shklovskii VRH[60] or Šimánek's percolation model of hopping, originally developed for conduction in granular metals.[125] The authors conclude that Šimánek's model is the more likely, based on the parameters extracted from both fits. The same temperature dependence is reported by Zhou *et al*[126] for highly crystalline ($X_C$ ~ 90%), undoped samples; they also interpret their data in the framework of granular conduction. Konezny *et al*[127] developed a model for transport in highly crystalline ($X_C$ > 60%) undoped samples involving fluctuation-induced tunneling, based on the work of Sheng,[128] and found good fits to their data at low temperatures, with deviations at high temperatures.

The work of Lips, Kanschat and Fuhs[58] provides a great deal of information about the microscopic nature of electronic conduction via an extensive electron resonance (ESR) study. Among the important points of this work are that nc-Si:H exhibits a metal

insulator transition (MIT) at ~$4\times10^{18}$ P/$cm^3$, approximately the same doping concentration as in c-Si, and that the intra-grain mobility is similar to comparably doped c-Si. These two facts show that on a very local scale (within the nanocrystalline grains) the electronic environment is similar to that of crystalline silicon. In agreement with others, Lips and coworkers conclude that band tail states in the grain boundary between crystallites limits the global conduction between electrodes.

The study of Si nanocrystals (ncs) in various insulator composites is also potentially relevant as, over much of the temperature range studied here, the a-Si:H is effectively an insulating material. Balberg and coworkers have examined Si ncs in a matrix of $SiO_2$ (Si nc/$SiO_2$).[129,130] They found many similarities in the photocurrent behavior between highly crystalline Si nc/$SiO_2$ composites and highly crystalline nc-Si:H, with the majority of their data taken below room temperature.[129,131] However, their results from the same work concerning the temperature dependence of the dark conductivity of Si nc/$SiO_2$ did not clearly demonstrate a dominant conduction pathway. So *et al*[132] report activated conduction in undoped Si ncs in insulating $Si_3N_4$ and a $\sigma \sim \exp[-(T_0/T)^{1/2}]$ temperature dependence of the conductivity for a doped version of the Si nc/$Si_3N_4$ system, which they find is best described by the model of hopping in granular metals.[125] A work studying the transport in heavily p-type doped nc Si/a-SiC:H samples by Myong *et al*[133] find the conductivity follows $\sigma \sim \exp[-(T_0/T)^{1/4}]$, which they attribute to band tail hopping.

This thesis describes detailed conductivity measurements over a wide temperature range (10 – 470K) of n-type doped a/nc-Si:H in the transition region between amorphous

and nanocrystalline, with $X_C$ varying between 0 and 30%. These measurements, when analyzed using the reduced activation energy,[134–136] clearly indicate that three transport mechanisms are active within the films. The microscopic states responsible for the conduction will be discussed and a model of the conduction is presented. These data are supplemented with noise spectroscopy and thermal equilibration measurements.

## Chapter 3

## SAMPLE PREPARATION

Amorphous and mixed-phase silicon are most commonly grown by plasma enhanced chemical vapor deposition (PECVD)[137] and its many variants, such as very high frequency PECVD (VHF-PECVD),[138–141] expanding thermal plasma (ETP),[142] and remote plasma deposition.[143] In these techniques a low-temperature plasma is employed to dissociate silane ($SiH_4$) into silicon and hydrogen radicals, which may then be deposited onto substrates in the plasma chamber. Other notable techniques include hot wire (HW) deposition, where a hot filament serves to dissociate the silane,[144–147] and sputtering, which must be done in the presence of hydrogen gas in order to produce a-Si:H.[148] Currently, PECVD is the most widely used deposition process for both research and industrial applications. Growing mixed-phase material by PECVD requires tuning the plasma parameters within a narrow band for which acceptable material can be synthesized. In order to allow for greater flexibility in sample parameters, we have used a dual plasma approach, in which each phase is produced in a separate plasma chamber, decoupling the growth of the amorphous and nanocrystalline material.[116] In this chapter, I will first provide a basic introduction to the deposition of both amorphous and mixed-phase silicon in a single plasma system and then describe the novel dual plasma approach used to grow the samples in this thesis.

### 3.1 Single Plasma Deposition of Silicon

During PECVD of electronic quality a-Si:H, pure silane gas ($SiH_4$) at pressures less than 1 Torr is dissociated by electron bombardment using an RF source, typically operating at 13.56 MHz and a power density of ~50 mW/cm$^2$.[5] Improved film properties can be achieved by dilution of the silane with hydrogen.[149] The dissociated silane, mainly in the form of $SiH_3$ radicals, generates a flux of growth precursors to the film's surface, where it begins to adhere to the substrate and form a film. The best quality films are grown with the substrates at ~250ºC, which minimizes the mid-gap defect density as measured by electron spin resonance.[150] In a single plasma deposition of mixed-phase silicon, the nanocrystallites may be either nucleated within the growing film or form in the plasma and then be transported to the film. The first method produces films which are termed either microcrystalline or nanocrystalline silicon (μc-Si:H or nc-Si:H respectively),[151,152] both terms referring to the same material in most cases. Films produced by the gas phase nucleation of silicon nanocrystals are referred to as polymorphous silicon (pm-Si:H).[153]

In order to produce nc-Si:H or μc-Si:H films, the majority of researchers grow films using silane heavily diluted with hydrogen, typically with a ratio of $H_2$:$SiH_4$ of 10:1 or greater.[152] There are three proposed mechanisms for the role of hydrogen in the formation of the crystalline material: enhanced surface diffusion,[154] weak bond etching[155] or chemical annealing.[156] Matsuda concluded that surface diffusion is the most likely mechanism based on a review of the experimental data in the literature.[151,157] Alternatively, mixed-phase silicon can be produced by diluting the silane with an inert

noble gas, such as argon[158] or helium.[159] The inert gas is believed to deliver additional energy to the film's surface, primarily via metastable excited states of the noble gas rather than via ionized states. The additional energy either breaks strained Si-Si bonds or enhances the surface diffusion via localized heating, allowing bonds to reform into a crystalline structure.[158]

Synthesizing pm-Si:H, wherein the nanocrystallites are nucleated in the plasma rather than the film's surface, requires high RF power densities, high gas pressures and hydrogen dilution. These conditions tend to produce nanoparticles in the plasma, while avoiding agglomeration of the nanoparticles. Plasmas with these conditions are often called "dusty plasmas" due to the presence of nano- to micron sized particles which significantly alter the plasma properties.[160] The high RF power promotes the formation of additional $SiH_3$ radicals as well as the more reactive $SiH_2$ and SiH radicals, while the high pressure reduces the mean free path of the radicals in the plasma, enhancing the probability of their interaction in the gas phase to form higher order silane molecules and eventually particles. The hydrogen plays a role in the crystallization of the nanoparticles. These nanoparticles are then incorporated into the film as it grows[161,162] – this is in addition to the normal amorphous silicon film that is grown through $SiH_3$ diffusion to the substrate. This growth mechanism leads to films with significantly different transport properties than a-Si:H.[53,163,164] This form of mixed-phase silicon growth, where the nanocrystallites are produced in the gas phase, is the most similar to the co-deposition process described in the next section.

### 3.2 Dual Plasma Deposition of Undoped Films

While pm-Si:H films exhibited an increased resistance to the Staebler-Wronski effect (SWE) and generally improved transport properties,[53] there is only a narrow window of growth conditions that yields high quality films. Moreover, it is difficult to separately adjust the particle and film properties. In order to maximize the benefits of pm-Si:H while addressing some of its drawbacks, a co-deposition dual plasma process was developed,[116,165] in which two plasmas are simultaneously operated, allowing for the independent tuning of the deposition parameters of each plasma for the desired material (amorphous or nanocrystalline). The basic schematic of such a reactor is depicted in figure 3.1. In the upstream reactor (fig. 3.1a) silicon nanocrystals are synthesized, which are then entrained by an inert carrier gas and injected into a downstream reactor where an amorphous film is grown, as illustrated in fig. 3.1b. The nanocrystals are incorporated into the growing film, resulting in a mixed phase film. The nanocrystal reactor is based on the design of Mangolini *et al*,[166] known to produce high quality silicon nanocrystals with a narrow size distribution. The downstream reactor is operated at a lower pressure and RF power level compared to the nanocrystal reactor (0.7 Torr vs 1.5 Torr and 5W vs 50W, respectively)[116] in order to produce a high quality amorphous matrix in which the silicon nanocrystals are embedded.

From a research standpoint, another advantage of this deposition process is that films with varying crystalline fraction, but a single crystallite size, can be produced in a single deposition run. Films closest to the nanoparticles injection point, denoted as C in the figure 3.1b, have the highest concentration of nanocrystallites, while no nanocrystals

are detected in films near the edge of the reactor (substrate A). To emphasize the fact that both phases are produced separately, I will denote films grown with the dual plasma method as hydrogenated amorphous/nanocrystalline silicon (a/nc-Si:H).

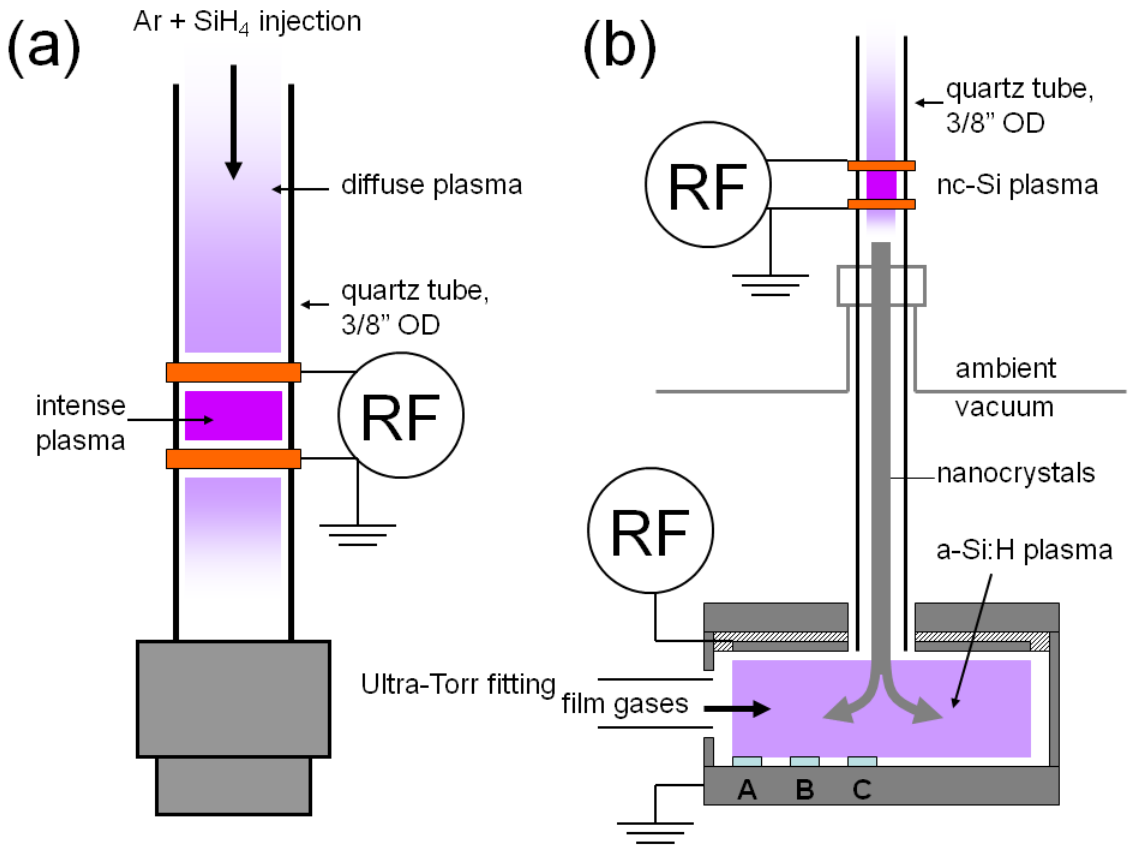


Figure 3.1: (a) A close up of the nanoparticle reactor. (b) A schematic of the complete deposition system – silicon nanocrystals are grown in the top reactor which are then entrained by the argon gas and injected into the bottom chamber, where the amorphous film is deposited. The distance of the substrate from the injection point determines the crystal concentration of the film, with the C film having the highest concentration of nanocrystallites and the A film exhibiting no detectable nanocrystallites.

### 3.3 Dual Plasma Deposition of Doped Films

The deposition system described in the previous section did not have access to dopant gases; this was done deliberately in order to ensure that any effects observed in the films were due to the nanocrystalline inclusions and not resulting from unintended residual gas doping. However, doped films are important for technological applications (for example, in p-n junctions or n+ contact layers) and the transport in doped mixed-phase silicon films is poorly understood. This motivated the construction of a new dual-chamber co-deposition system in order to synthesize and study doped a/nc-Si:H. For technical reasons, it's geometry differed slightly from the undoped system.

There are two main differences between the undoped co-deposition reactor and the second reactor used for doped films: (1) the geometry has changed from top-injection of the nanoparticles to side-injection and (2) a single source of precursor gas is used.[136,167] Both changes were made due to limitations of the available process equipment. The reactors in the side-injection configuration are also operated at different pressures and RF power levels in order to optimize growth conditions for each phase, but now the amorphous film's precursor gases are the residual silane/doping gases left unreacted from the nanoparticle reactor. This side-injection reactor also produces films with varying nanocrystalline concentrations in a single deposition run. A schematic of the reactor is displayed in figure 3.2.

For the films used in this study, the nanoparticle reactor, consisting of a 3/8" quartz tube with ring electrodes, was set to high power and pressure conditions (70W, 1.7 Torr) to promote the growth of nanoparticles. The film reactor was set to a lower power level

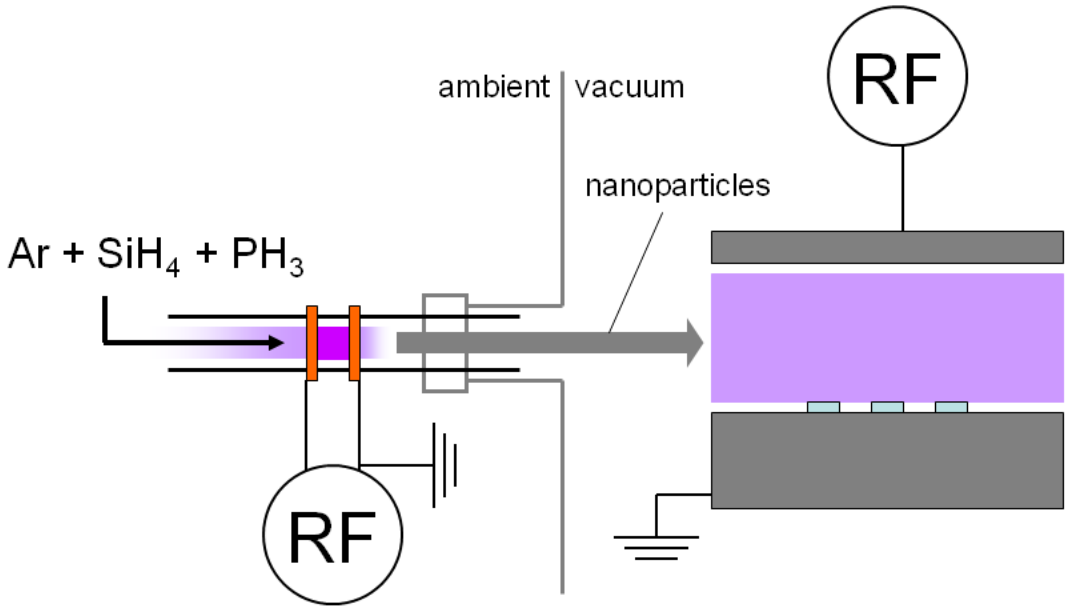


Figure 3.2: The side-injection configuration for growing doped mixed-phased silicon thin films. The upstream reactor (left) produces nanoparticles that are entrained by the inert argon and injected into the downstream reactor (right) where the a-Si:H film is grown on a heated substrate. The physical spacing of the substrates in the chamber, along with the $Ar/SiH_4$ ratio, determined the crystal fraction of the films.

and pressure (5W, 0.7 Torr). An orifice between the two chambers is used to adjust the pressure difference between the two reactors. The total gas flow was set to 90 sccm for the films produced here with the doping set by the gas phase ratio of $PH_3/SiH_4$ ($6\times10^{-4}$). The crystallinity was altered by changing the $Ar/SiH_4$ ratio and the position of the substrates in the chamber. Films were grown on Corning 1737 glass substrates for

transport and Raman measurements, while additional samples (in the same run) were grown on c-Si wafer pieces for FTIR measurements. The typical film thickness is ~2 μm, with one film being 250 nm.

### 3.4 Improved System for Dual Plasma Deposition

The dual plasma co-deposition system is able to synthesize materials that would be extremely difficult or impossible to produce in a standard single plasma approach. The system described in the preceding section was recently redesigned in order to allow more flexibility in the choice of process gases and to enhance the reliability and reproducibility of the samples. The reactor was built in collaboration with David Rowe from Prof. Uwe Kortshagen's group in Mechanical Engineering. Prof. Kortshagen has a separate set of plasma reactors to produce free-standing nanoparticles or thin films of nanoparticles which shares the gas manifold and pumping lines.

The co-deposition system is capable of fabricating a wide range of mixed-phase materials, including: freestanding Si, Ge, or SiGe nanocrystals; Si, Ge or SiGe nanocrystals in a-Si:H; Si, Ge or SiGe nanocrystals in a-Ge:H; Si, Ge or SiGe nanocrystals in insulating a-$SiN_x$:H; single phase a-Si:H, a-Ge:H, a-SiGe:H or a-$SiN_x$:H; and multilayer structures such as employed in thin film transistors. The film and nanoparticles are produced in separate reactors with separate gas lines, allowing the two phases to be independently doped; for example, one could grow n-type Si ncs embedded in p-type a-Si:H, a material which would be impossible to produce in a single plasma reactor. Proof of concept undoped a/nc-Si:H films have been produced in the newly

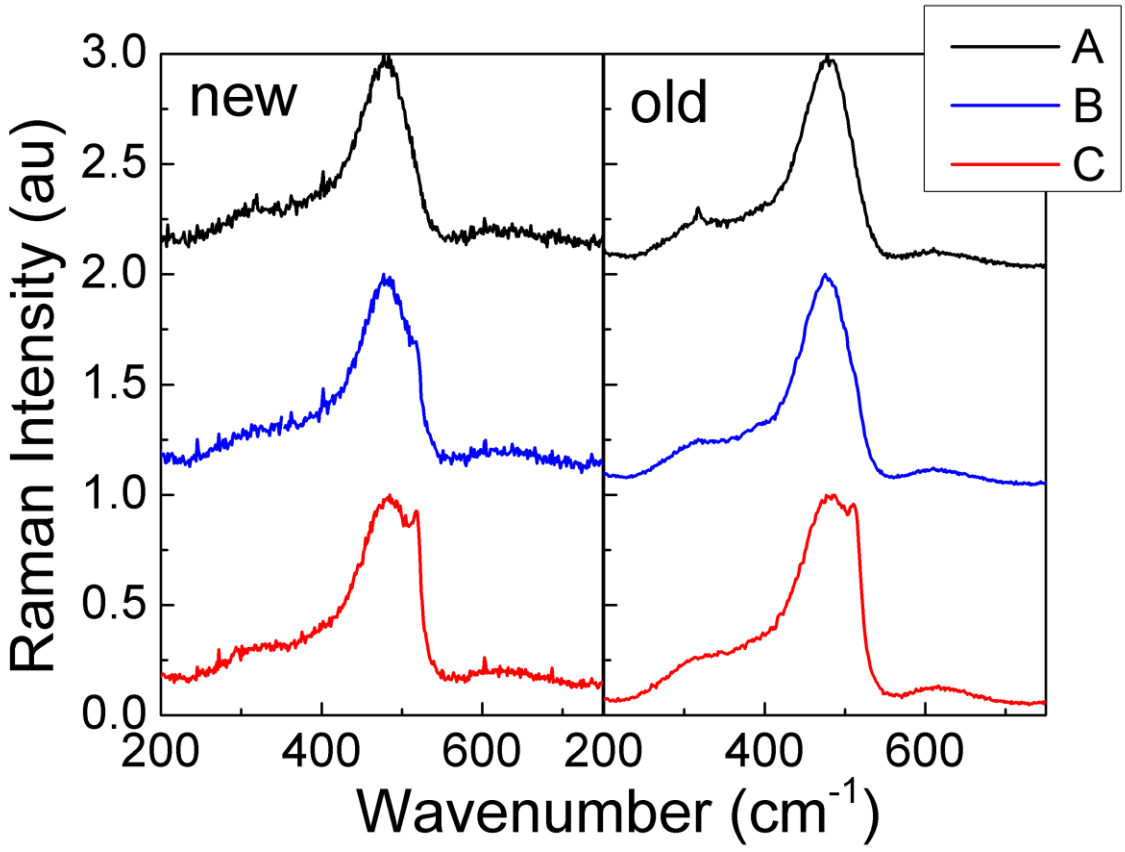


Figure 3.3: Raman spectra of undoped a/nc-Si:H films produced from the newly redesigned reactor (left) compared to undoped a/nc-Si:H films produced in the previous co-deposition system (right). Raman spectroscopy is used to quantify the fraction of the material that is crystalline – the sharp peak at ~520 $cm^{-1}$ is due to the crystalline component of the material. The newly grown films show a similar spread in crystal fractions as compared to the earlier samples.

redesigned and rebuilt system, which are compared to the films produced by the earlier undoped co-deposition system described in section 3.2.[116] Representative Raman spectra for films synthesized in both reactors are plotted in figure 3.3. In addition, a wide range

of silicon and germanium nanoparticles have been synthesized and characterized. Recent work by Kent Bodurtha on nc-Ge/a-Si:H composite materials, enabled by this reactor, has already shown several interesting phenomena.[165]

# Chapter 4

# EXPERIMENTAL TECHNIQUES

## 4.1 Structural Characterization

In this section, I will describe the three primary structural characterization techniques that were employed here; infrared (IR) spectroscopy, Raman spectroscopy and X-ray diffraction (XRD). Both Raman and IR spectroscopy probe the vibrational modes of a sample in order to extract information about the local environment and bonding structure. The presence or absence of vibrational modes, shifts of certain modes, and relative strength of selected modes can all provide information about the microscopic bonding environment. Infrared absorption and Raman scattering are complimentary techniques, as bonds are generally either primarily Raman or IR active, meaning the bond is only observable, or can be more clearly observed, with one technique or the other. IR spectroscopy relies on the direct absorption of light, while Raman is a form of inelastic scattering of photons with phonons. The third technique, XRD, is based on the diffraction of x-rays from lattice planes in a crystal. In addition to identifying and confirming the presence of crystalline material, XRD can provide information on the crystallite size. In the following sections, I will briefly explain the theoretical principles underlying each technique, explore the limitations and advantages of each method, and discuss the usefulness of these techniques as it applies to thin film silicon.

### 4.1.1 Infrared (IR) Spectroscopy

Infrared (IR) spectroscopy relies on the excitation of vibrational modes via direct absorption of IR light. According to classical electrodynamics, a changing electric dipole moment (either in direction or magnitude) can absorb or emit radiation, with the classic example being a simple oscillating dipole.[168] Any vibration that leads to a non-zero change in the dipole moment of the system will be IR active and lead to absorption. For example, consider two bonds relevant in amorphous silicon in figure 4.1:

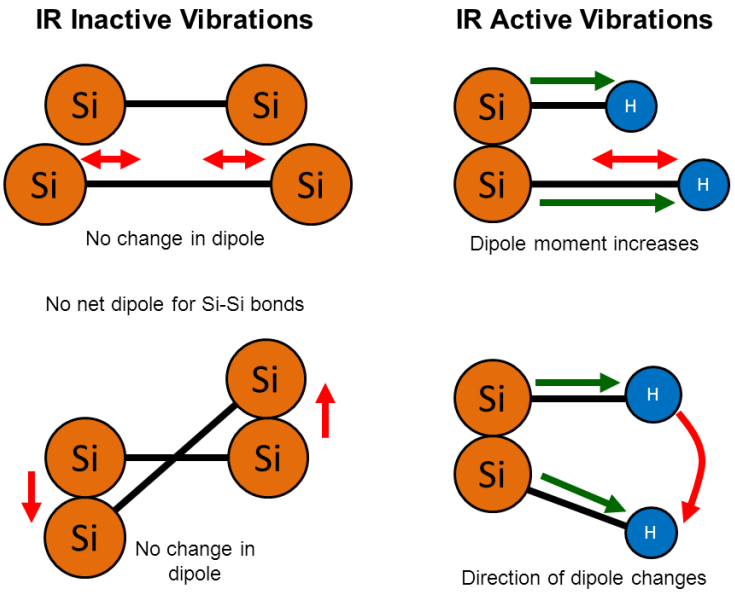


Figure 4.1: Sketches of two different bonds relevant to thin film silicon, one which is IR inactive, the Si-Si bond, (left) and one of which is IR active, the Si-H bond (right).

On the left side of figure 4.1, we see that the Si-Si bond is symmetric and has no net dipole, which by itself does not make the bond IR inactive. More importantly, no dipole

moment is induced by the vibrational motions indicated, making the bond IR inactive. For the Si-H bonds on the right there is a net dipole moment due to the differences in electron affinity between silicon and hydrogen. Thus both stretching (top) and wagging (bottom) vibrations cause a change in the dipole moment and induce IR absorption. It can be shown that any normal vibration of an asymmetric bond (that is, a bond with a net dipole) will be IR active.[169] For a more complete introduction to infrared spectroscopy, the reader is referred to the classic text by Herzberg[169] or the more recent book by Smith.[170]

In crystalline silicon, there are many silicon-hydrogen absorption lines that can be observed in IR spectroscopy.[171,172] These lines correspond to differences in the local environment (e.g. Si-H or $Si-H_2$) or different types of motion (stretch, wag or scissors). In amorphous and nanocrystalline silicon, the inherent disorder of the material broadens these absorption lines. There is a greater frequency difference between different types of vibrational motion resulting in three main silicon-hydrogen groups[148] – the wagging modes at 640 $cm^{-1}$, the scissors modes at 900 $cm^{-1}$ and the stretching modes near 2000 $cm^{-1}$. Within these groups, the internal structure of the absorption spectrum is determined by the differences in the local environment of each bond, such as the number of hydrogens bonded to each silicon, the location of the silicon atom (e.g. bulk or surface), which atoms are back-bonded to the silicon (usually a silicon or oxygen atom) and if there are nearby hydrogens bonded to other silicon atoms, which can influence the frequency via a dipole-dipole interaction.

We shall concern ourselves here with silicon-hydrogen stretch modes, located in the

2000 – 2100 $cm^{-1}$ region of the spectrum. Generally two distinct peaks can be observed in the IR spectrum, indicating differing local environments of the Si-H bonds. While the low stretching mode (LSM) peak at 2000 $cm^{-1}$ is ascribed to isolated Si-H bonds,[173–175] the high stretching mode (HSM) at 2090 $cm^{-1}$ has been attributed to either the presence of $Si-H_2$[175] or clustered Si-H.[176,177] By correlating the relative strength of each mode as a function of hydrogen content and density, Smets and van de Sanden found evidence that the LSM were monohydrides residing near vacancies and that the HSM represented clustered hydrogen on void surfaces.[31] In order to quantify the amount of hydrogen in each mode, we use the microstructure parameter, *R*:

$$R = \frac{I_{2090}}{I_{2090} + I_{2000}} \tag{4.1}$$

where $I_{2000}$ and $I_{2090}$ represent the integrated intensity of the 2000 and 2090 $cm^{-1}$ mode respectively. An example of the fitting procedure is depicted in figure 4.2. This ratio gives an indication of the heterogeneity of the films, as a higher *R* indicates more clustered hydrogens, likely at void or grain boundary surfaces. It has been previously observed in a-Si:H that an increase in *R* corresponds with an increase in the structural disorder in the film.[173,174,178]

Concerning the IR spectra of mixed-phase silicon, additional lines are sometimes observed that correspond to shifted LSM and HSM frequencies for hydrogen bonded to the nanocrystal surfaces.[59,179] The spectra for the films presented in this thesis contain only the traditional LSM and HSM modes of amorphous silicon in our samples, perhaps due to our relatively low nanocrystalline concentration (<30%) or other structural

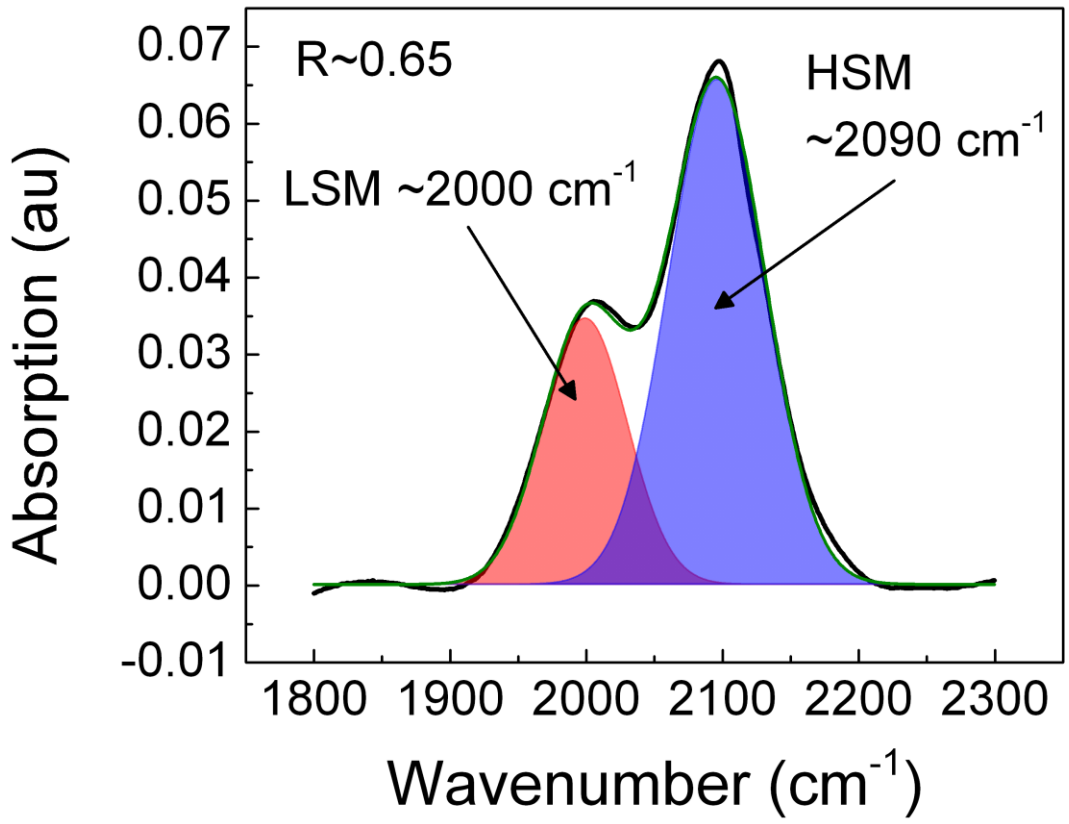


Figure 4.2: A sample IR absorption spectra for an n-type doped a-Si:H film – both the high stretching mode (HSM) and low stretching mode (LSM) are visible. The relatively large *R* value (0.65) indicates that the film likely contains many voids and is structurally disordered.

variations that serve to obscure the signal from that due to the hydrogen attached to the nanocrystallites. The IR data presented in this thesis were collected using a Nicolet Magna 750 Fourier Transform Infra-Red (FTIR) spectrometer operating in transmission mode within the Characterization Facility (CharFac) at the University of Minnesota. Samples to be analyzed using FTIR were grown on silicon wafer substrates, as the glass

used for transport measurements is not transparent in the IR unlike c-Si.

### 4.1.2 Raman Spectroscopy

Raman spectroscopy probes the vibrational modes of a material by measuring the frequency shifts of inelastically scattered photons. The shift in the energy of the photon corresponds to a Raman active vibrational mode of the system. The elastic scattering, in which the incoming light's frequency does not shift, is referred to as Rayleigh scattering. Since Rayleigh scattering is a two particle process (electron + photon) and Raman scattering is a three particle process (electron + phonon + photon), the intensity of Raman scattering is several orders of magnitude smaller than Rayleigh scattering. Raman lines are only active if the vibration induces a change in the polarizability of the bond; generally, symmetric bonds are more likely to be Raman active. A good explanation of the basic principles of Raman spectroscopy can be found in the introductory chapter of E. C. Le Ru and P. G. Etchegoin.[180]

As Raman is most sensitive to symmetric modes, we will use it to probe the silicon-silicon bonds. When many atoms come together to form a periodic arrangement in a crystal, the vibrational modes of the system describe a set of collective vibrations called phonons. Rather than appearing as individual discrete lines as in molecules or isolated bonds such as the silicon-hydrogen bond, these vibrations are characterized by a set of allowed frequencies called bands. Despite the fact that amorphous silicon does not possess long range periodic order, it still exhibits phonon bands that are remarkably similar to crystalline silicon.[5] There are four observed phonon bands – the transverse

optical (TO), transverse acoustic (TA), longitudinal optical (LO) and longitudinal acoustic (LA). While Raman is most sensitive to symmetric bonds, it can also detect the Si-H bonds, both the wagging modes at 600 $cm^{-1}$ and the stretch modes near 2000 $cm^{-1}$, though with a much lower signal-to-noise ratio than with FTIR; the wagging modes near 600 $cm^{-1}$ are visible as a small peak in the a-Si:H spectra in figure 4.3.

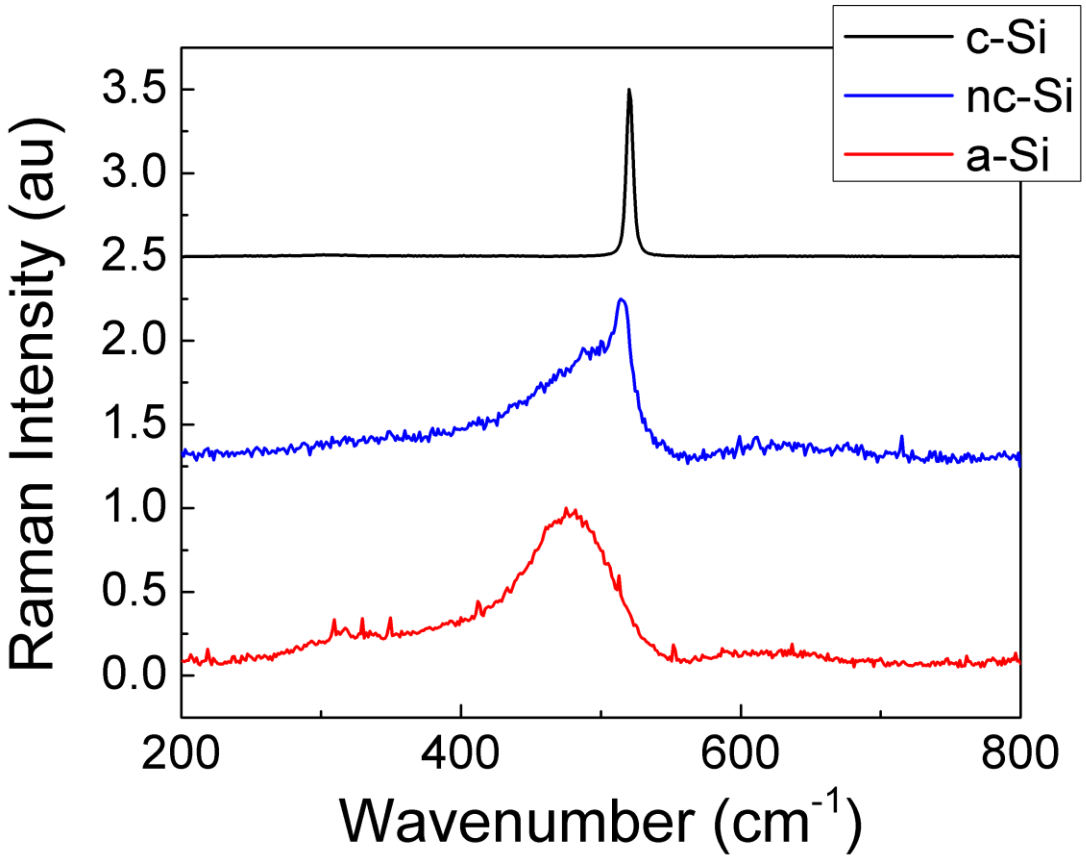


Figure 4.3: Comparison of the Raman spectra for crystalline (top), nanocrystalline (middle) and amorphous (bottom) silicon. A broadening of the TO Raman mode is observed, along with the appearance of other modes (LO, LA) as the material becomes more disordered. The nanocrystalline sample also contains a significant amorphous component, partially obscuring the main peak, which is noticeably broader than in c-Si.

Selection rules play an important role in determining which particular modes are observed using Raman spectroscopy. Figure 4.3 shows three Raman spectra; crystalline silicon (top), a-Si:H (bottom) and freestanding silicon nanocrystals (middle). Even though the materials have remarkably similar phonon spectra, the Raman spectra are quite different, with crystalline silicon (c-Si) only displaying a single peak at 520 $cm^{-1}$ rather than a broad band with multiple peaks as for a-Si:H. In c-Si, momentum ($k$) must be conserved and as a photon has negligible momentum compared to a phonon, only one part of the phonon spectra is visible; the $k = 0$ point of the TO mode. As discussed in chapter 1, a-Si:H lacks long range order and does not require $k$-conservation, consequently Raman scattering from all of the phonon modes can be observed. The locations of the Raman active modes in mixed-phase silicon are listed in table 4.1.

| **Phase** | **Mode** | **Center ($cm^{-1}$)** | **Width ($cm^{-1}$)** |
|---|---|---|---|
| a-Si | TA | 170-180 | 50-55 |
| a-Si | LA | 310-320 | 60-65 |
| a-Si | LO | 410-420 | 85-90 |
| a-Si | TO | 480 | 55 |
| nc-Si | TO* | 500-510 | 20-30 |
| nc-Si | TO | 515-520 | 8-10 |

Table 4.1: Raman modes in amorphous and nanocrystalline silicon, listing the wavenumber where the mode is centered, the mode's width and bonding phase to which the mode corresponds. A discussion of the mode labeled TO* is presented in the text.

The issue of *k*-conservation is of particular importance as it applies to Si nanocrystals (ncs). For Si ncs, long range order is limited by their finite size, which slightly relaxes the *k*-selection rules. This relaxation leads to more of the phonon band being accessible, all of which is lower in energy than 520 $cm^{-1}$. Because the silicon nanocrystals are ordered over longer length scales than amorphous silicon, there is a slight downward shift of the TO mode by a few $cm^{-1}$ in addition to asymmetric broadening.[181–183] Researchers often cite the downward shift as resulting from quantum confinement (QC) effects, a somewhat confusing terminology as QC is typically associated with an increase in energy, as observed in the optical absorption or photoluminescence (PL) spectra of QC silicon nanocrystals.[184] Actually, the downward shift of the Raman peak is due to the relaxation of momentum selection rules brought on by a finite lattice size rather than confinement of the phonon modes. Because of the shift's dependence on the particle's size, it is tempting to use the Raman shift to quantify the particle size, but one must exercise caution, as many other factors, including stress[183] and surface states,[185] can cause similar shifts.

The dramatic differences in the Raman spectra of amorphous and nanocrystalline silicon enable us to use Raman measurements to quantify the relative amounts of each phase in a sample. In particular, we examine the ratio of the integrated intensities of the TO peaks, defining the crystal fraction ($X_C$) as:

$$X_C = \frac{I_{520} + I_{500}}{I_{520} + I_{500} + I_{480}} \tag{4.2}$$

Here, $I_{480}$ and $I_{520}$ represent the areas under the amorphous (480 $cm^{-1}$) and crystalline (520 $cm^{-1}$) TO peaks respectively. For large crystalline fractions, an additional peak at 500 - 510 $cm^{-1}$ ($I_{500}$) is included in the crystal content calculations, in order to account for the natural asymmetry of Raman signals arising from nanoscale silicon crystallites.[181,183,186] Some researchers ascribe the lower peak of the nc-Si modes to grain boundary scattering.[187] The actual fitting of the data is not straight forward, as the location and shape of the peaks in nanocrystalline silicon is the subject of debate – the reader is referred to Smit *et al*[186] for a detailed discussion of the common fitting techniques. For reasons of consistency, we will adhere to the standard method of using two peaks to fit the nc-Si portion of the spectra. An example of the fitting procedure for a typical mixed-phase silicon film is shown in figure 4.4.

Often a correction factor is employed to adjust for the ratio of the Raman scattering cross sections between amorphous and nanocrystalline silicon and is typically taken to be around 0.8 – 0.9.[188–191] This factor has been omitted in our calculations of the crystalline content, that is the ratio of scattering cross-sections is taken to be unity, as the value is dependent on crystallite size as well as the optical absorption of the crystallites, and is presently not thoroughly established.[188,191] Any error in the determination of the crystalline content by neglecting this factor will affect the absolute crystal fraction, but not the relative values for the series of films studied here.

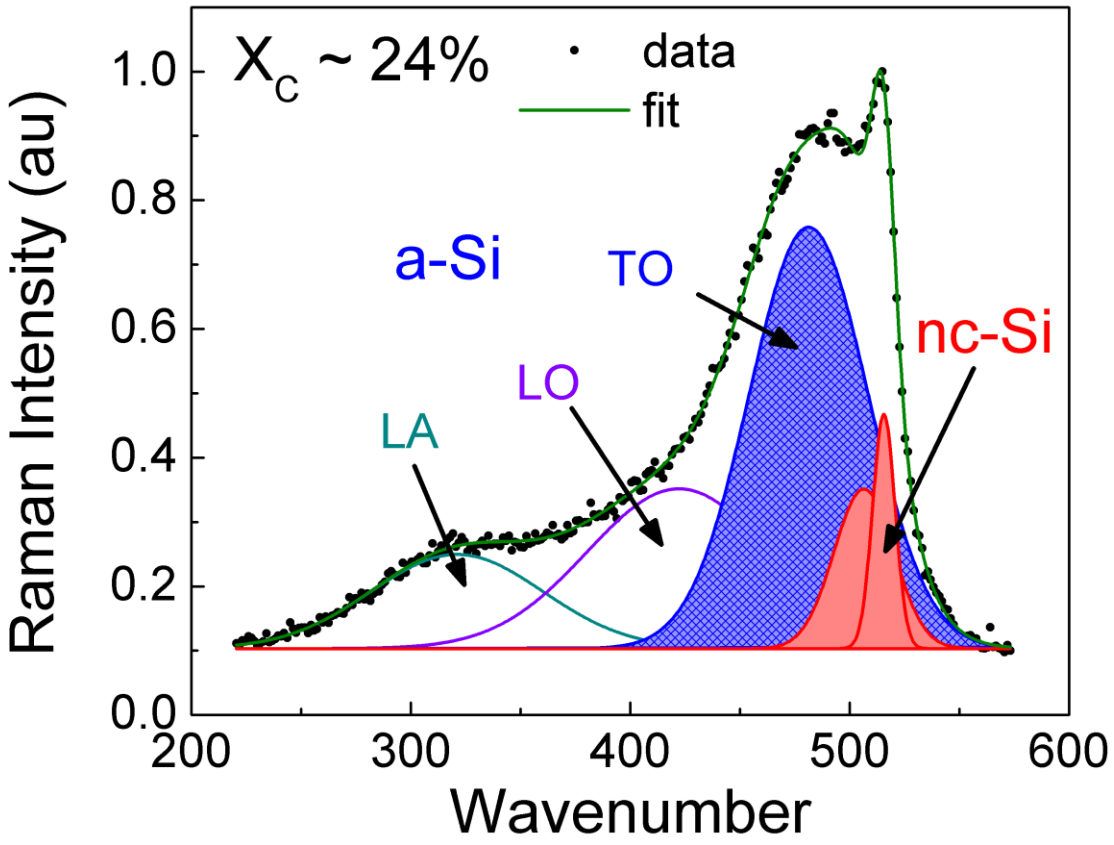


Figure 4.4: Sample Raman spectra for an undoped mixed-phase silicon thin film, where the important amorphous and nanocrystalline modes are labeled. The modes used in the crystal fraction determination are shaded – hatched blue for the amorphous TO mode and solid red for the nc-Si TO modes. The crystal fraction ($X_C$) for this undoped film is determined to be ~24%.

The Raman data were collected using a Witec Alpha 300R confocal Raman microscope located within the Characterization Facility (CharFac) at the University of Minnesota. It was equipped with an UHTS 200 spectrometer and used an argon-ion

excitation laser (514.5 nm) at a power of 5 mW focused to a diameter of ~ 2-3 μm. These parameters were chosen to minimize heating of the sample by the laser, which can cause distortions in the final spectra, and were determined by comparing data from various powers and spot sizes. Due to a notch filter designed to reduce the intensity of Rayleigh scattering at a wavelength shift of zero, the TA peak could not be observed and was not used in fits of the Raman data.

### 4.1.3 X-Ray Diffraction (XRD)

When scattering monochromatic light with a wavelength smaller than the interatomic spacing of the sample (~2.5Å for silicon), diffraction occurs between planes of equally spaced atoms for angles corresponding to constructive interference. As a toy model, consider two planes of atoms separated by a distance $d$ and x-ray light with a wavelength $\lambda$ incident upon the sample at an angle $\theta$ (figure 4.5). The condition for constructive interference is:

$$n\lambda = 2d \sin\theta \qquad (4.3)$$

where $n$ is an integer. The right hand side of eqn. 4.3 is the total path difference between light reflected from adjacent planes. By plotting the intensity of the scattered light against the angle of incidence (or reflection), one can obtain the spacing between the different crystalline layers and identify the crystalline structure of a material.

XRD provides only limited information for amorphous materials as it probes the long range order. For nanocrystalline materials, XRD provides evidence of the crystallinity of the sample and, by using the broadening introduced by the finite size of

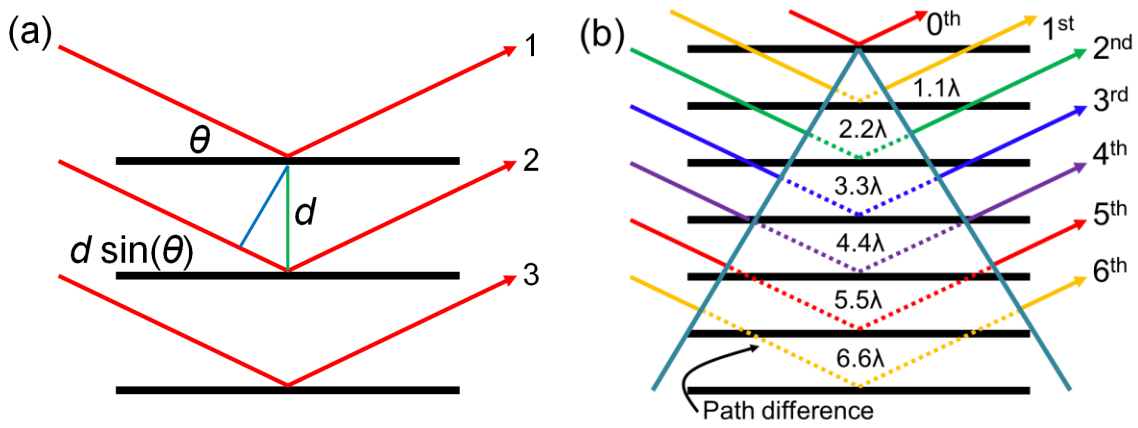


Figure 4.5: (a) A cartoon illustration of x-ray scattering from parallel planes of atoms. The path difference between rays 1 and 2 is given by $2d\times\sin(\theta)$ and must be equal to an integer multiple of the wavelength $\lambda$ of the incident x-rays for constructive interference to occur. (b) A pictorial description of finite size broadening. Each reflection must have a partner lattice reflection a few planes down for proper destructive interference; the path difference (dotted lines) between these reflections must be $n\lambda/2$, where $n$ is an integer. The $0^{th}$ and $5^{th}$ reflections are a pair (red, $5.5\lambda$ path difference) and the $1^{st}$ and $6^{th}$ are a pair (orange, $6.6\lambda - 1.1\lambda = 5.5\lambda$ path difference).

the lattice, can determine the crystallite size. In a sample with an infinite number of lattice planes (as is essentially the case in a bulk, single crystal sample), the diffraction peaks' width is determined by instrumental and thermal broadening. As the grain size of the sample decreases, the infinite lattice assumption breaks down and there is additional broadening due to the nanocrystal's finite size. The maximum crystallite size that can be observed depends on the instrument, but generally speaking, crystal sizes up to about 100 nm will produce broadening that can be observed above the instrumental background.

The XRD data in figure 4.6 illustrates how one can resolve the grain size difference between two samples, where the grain sizes are 3.5 nm and 18 nm.

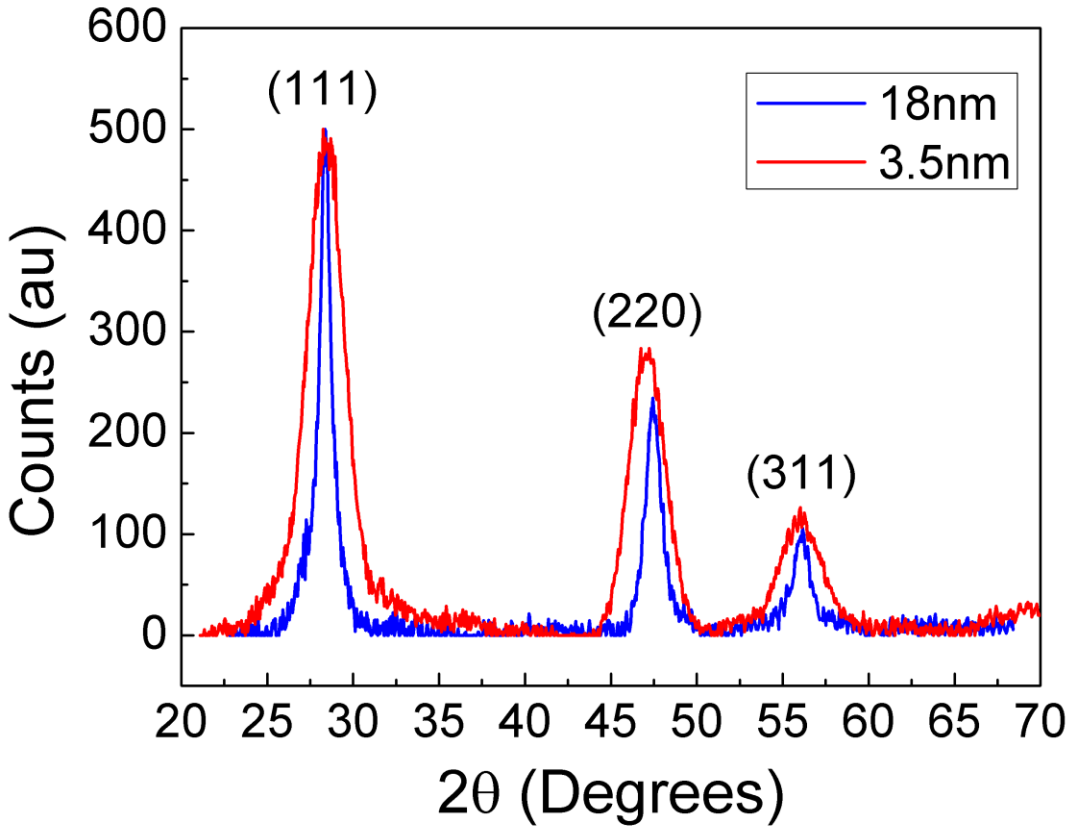


Figure 4.6: Sample X-ray diffraction (XRD) patterns from nanocrystalline silicon samples with different grain sizes. Notice the broader line shapes for the sample with 3.5 nm grains (red) as compared to 18 nm sample (blue).

For an intuitive understanding of this broadening, consider our toy model above (figure 4.5b). Suppose we are at an angle of incidence such that the path difference for reflections from the first plane is $1.1\lambda$ (rather than $\lambda$ which would lead to constructive

interference). For the second plane, the path difference is 2.2$\lambda$, for the third plan it is 3.3$\lambda$ and so on until for the fifth plane and sixth planes it is 5.5$\lambda$ and 6.6$\lambda$ respectively. The fifth plane is exactly out of phase with the surface ($0^{th}$) reflection and the sixth plane is out of phase with the first plane. Both have a 5.5$\lambda$ (11$\lambda$/2) path difference, which satisfies the $n\lambda/2$ condition for destructive interference. These two waves will destructively interfere and for an infinitely large crystal, every plane will have a partner plane with which it will destructively interfere when viewed at an angle that does not correspond to a Bragg reflection. If we now consider an angle that produces a difference of only 1.001$\lambda$, we see that the destructive interference partners are now 500 lattice planes apart; a Si nanocrystal with a 5 nm diameter is only ~15 lattice planes wide in the (111) direction (Bragg peak at $2\theta$ = 28.4°). Thus, the width of the peak, once instrumental artifacts have been taken into account, is a measure of the number of lattice planes in the sample, that can be converted to a crystallite size. A more rigorous analysis finds that the peak width due to crystallite size effects ($\beta$) is related to the crystallite size ($\delta$) by the Scherrer equation:[192]

$$\delta = \frac{\lambda}{\beta \cos\theta} \tag{4.4}$$

The XRD data were collected using a Bruker-AXS Microdiffractometer with 2.2 kW sealed Cu x-ray source ($\lambda$=1.5418Å). A data set collected using a Corundum sample ($Al_2O_3$), which has negligible natural linewidth compared to the instrumental factors, was used to calibrate the instrumental broadening.

## 4.2 Electronic Characterization

The electronic transport properties were characterized using three transport measurements: temperature dependent conductivity, thermal equilibration measurements and noise spectroscopy. Conductivity and noise spectroscopy are complimentary, as conductivity provides time averaged data, while noise spectroscopy probes fluctuations about the average. Thermal equilibration measurements characterize the glassy nature of the hydrogen microstructure in amorphous silicon and can differentiate between conduction that in the amorphous and nanocrystalline materials.

### 4.2.1 Conductivity

The conductivity measurements were carried out in a Janis closed-cycle helium cryostat, capable of controlled temperature variations from 10 to 500K. Due to the large sample resistance, measurements were made in a standard two-probe configuration using chromium contacts connected to thin wires using conductive silver paste. Ohmic behavior was confirmed throughout the temperature range measured. The data were collected by first annealing the sample at 470K for two hours to remove any effects from light induced defects (known as the Staebler-Wronski effect)[39] or surface adsorbates.[193] No difference in the conductivity was found between the annealed and light soaked states, which is not uncommon for doped samples. After annealing, the sample was slowly cooled (~3 K/min) to the lowest measurement temperature, typically 10K, and the conductivity was measured upon warming.

Evaluating the functional form of the temperature dependent conductivity data can

be challenging. One often plots the conductivity data against different abscissa ($T^{-1}$, $T^{-1/4}$, $T^{-1/2}$, log(T), etc), in order to establish a linear relationship. This approach is acceptable for data sets with a large dynamic range and when only a single transport mechanism is present. With smaller dynamic ranges or when a shift in the transport mechanism occurs, this technique can lead to erroneous results. One useful method for this situation is known as the "reduced activation energy" analysis, pioneered by Zabrodskii[134,194] and independently developed in an equivalent form by Hill.[195] It is particularly suited to differentiating between various forms of exponential temperature dependences, such as Mott or Efros-Shklovksii variable range hopping (VRH). The reduced activation energy is calculated from the conductivity data according to eqn. 4.5 and fit to determine the functional form. After Zabrodskii, we define the reduced activation energy, $w(T)$, as:

$$w(T) = \frac{d \ln \sigma}{d \ln T} \tag{4.5}$$

As an example, consider the generic form of VRH from chapter 2 (eqn 2.2):

$$\sigma = \sigma_0 \exp\left(-(T_0 / T)^x\right) \tag{4.6}$$

Applying eqn. 4.5 to eqn. 4.6 and simplifying, we obtain:

$$w(T) = x(T_0 / T)^x \tag{4.7}$$

The slope of a log-log plot of $w(T)$ against $T$ is the exponent $x$, which can be used to determine the type of VRH; $x$ = ¼ indicates Mott-VRH and $x$ = ½ indicates ES-VRH.[60] An exponent of zero ($x$ = 0) corresponds to a power law temperature dependence ($\sigma \approx T^n$) and the value of $w(T)$ gives the value of the exponent, $n$. A slope of unity for $w(T)$

reflects activated behavior, $\sigma = \sigma_0 \exp(-E_A/k_BT)$; if there are multiple activation energies within the measured temperature range, this will appear as a sawtooth-like pattern.[135]

### 4.2.2 Thermal Equilibration

To measure and quantify the thermal equilibration properties of the electronic transport in the n-type doped a/nc-Si:H films, the temperature dependence of the conductivity was measured as a function of the quench-rate from a high temperature anneal. In addition, the slow, time-dependent relaxation of the conductivity at a single temperature below the equilibration temperature was recorded. The former is identical to experiments used by Street *et al*,[37] while the latter are equivalent to sweep-out measurements described in Kakalios *et al*.[196] Because these phenomena are particular to a-Si:H, these measurements can be used to differentiate between conduction in the amorphous and nanocrystalline phase.

For the rate dependent conductivity measurements, the films were annealed at 470K and then quenched to room temperature at varying cooling rates, ranging from 0.1K/min to 100K/min. The sample rested in thermal contact with a copper block with resistive cartridge heaters and a copper tube, through which cool gas could flow to increase the rate of cooling. To achieve the fastest cooling rates of ~100K/min, the chamber was partially filled with dry nitrogen gas in order to improve the thermal response. The conductivity of the film was then measured under vacuum in the dark upon warming at a constant rate of 1K/min. For a conventional n-type doped a-Si:H film with no nanocrystalline inclusions, the conductivity magnitude and activation energy below a

temperature $T_E$ (~400 K) is sensitive to the rate at which the sample is cooled from a high temperature anneal, while above this temperature the conductivity is independent of thermal history. In order to quantify the variation in conductivity between fast and slow cooling, we define a metric called the "conductivity gap", $\sigma_{gap}$:

$$\sigma_{gap} = \frac{\sigma_{fast}}{\sigma_{slow}} - 1 \tag{4.8}$$

Where $\sigma_{fast}$ and $\sigma_{slow}$ are the conductivities at a given temperature following a fast cool (100 K/min) or slow cool (0.1 K/min) respectively. If no change is observed with thermal history, $\sigma_{gap}$ will be zero. The arrows in figure 4.7 demonstrate the conductivity gap at 350K for a standard doped a-Si:H sample.

For the relaxation measurements, the films were annealed at 470K and then rapidly quenched at ~100K/min. The temperature was then stabilized at the desired temperature and the conductivity was monitored as a function of time. For temperatures below the equilibration temperature, the conductivity slowly relaxes to a lower value. The relaxation curves can be fit to a stretched exponential time dependence:

$$\sigma = \sigma_0 \exp\left[-(t/\tau)^{\beta}\right] \tag{4.9}$$

Where $\tau$ is the relaxation time and the exponent $\beta < 1$. For the same $\tau$, as $\beta$ decreases, the rate of decay becomes faster for times less than $\tau$ and slower at times longer than $\tau$, making the plot appear stretched compared to a traditional exponential.

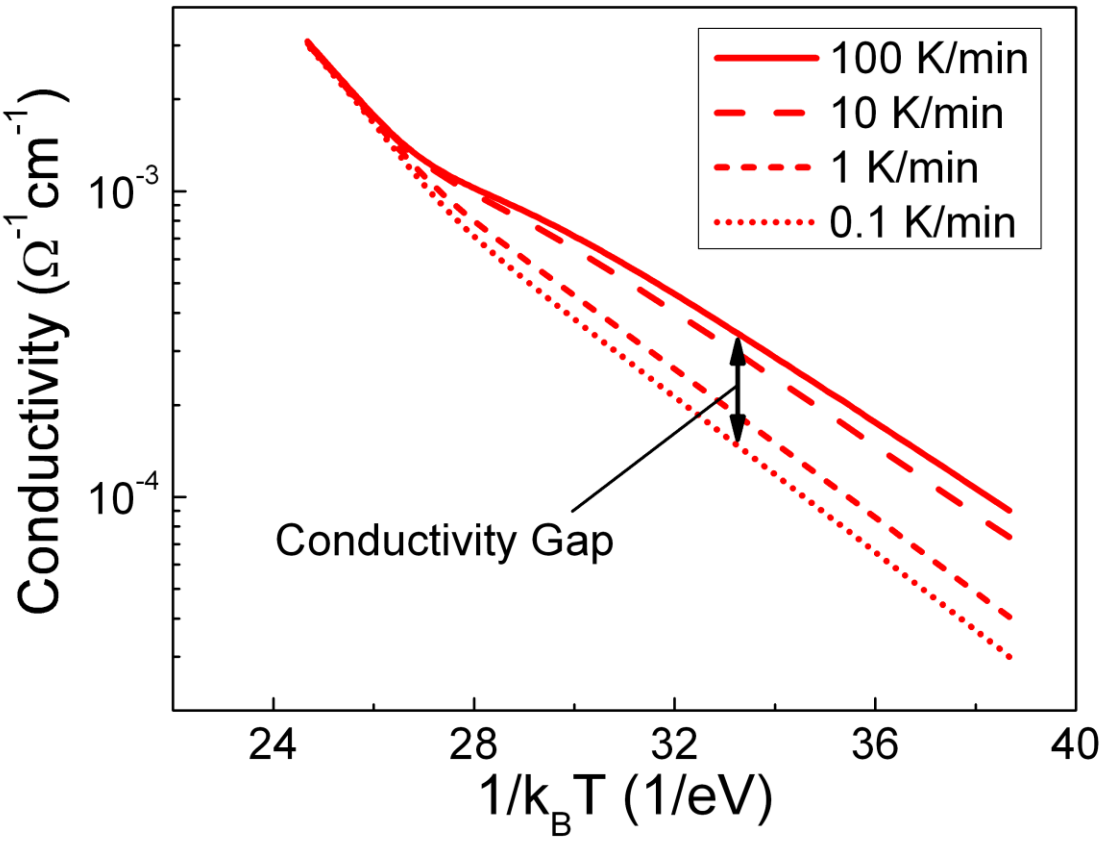


Figure 4.7: Arrhenius plot of n-type doped a-Si:H when cooled at different rates from a high temperature anneal, displaying the marked dependence of the conductivity on the cooling rate. The arrows show the conductivity gap, defined with eqn. 4.8 in the text, at 350K.

### 4.2.3 Noise Spectroscopy

The noise measurements were carried out using the system depicted in figure 4.8. The sample sits inside a shielded vacuum chamber on a copper block, where the temperature can be controlled from ~240K to 450K using a resistive heater and a flow of chilled nitrogen gas through the cooling tube. Electrical contact is made to the sample

using BeCu spring clips in contact with a thin layer of chromium (~50 nm) which has been thermally evaporated onto the sample. A series of batteries provides a voltage to the sample and the resulting current is amplified and converted to a voltage by an Ithaco 564 preamp, powered by batteries to reduce ground loops and 60 Hz pick-up. The amplified signal is digitized and Fourier transformed by an HP 3561A spectrum analyzer. Data were taken from just above dc (2.5 Hz) to 1 kHz and from 1024 to 4096 spectra were collected for analysis.

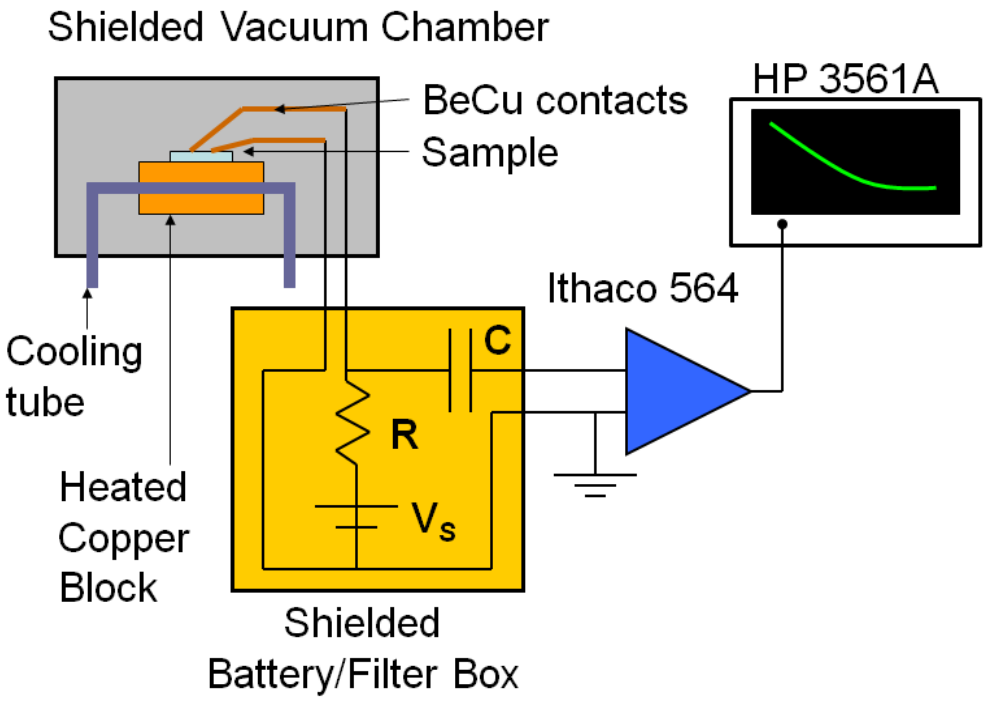


Figure 4.8: Sketch of the noise spectroscopy measurement set-up. The voltage is supplied to the sample via batteries and the Ithaco 564 amplifies the resulting current. An RC filter blocks the dc current so that the preamp may be set to the highest gain possible.

A simple RC filter, similar to that employed by Johanson *et al*,[103] is used to block the dc portion of the signal, permitting the use of a higher preamp gain. The RC time constant is determined by the parallel resistance of the sample and an added resistor *R*. For most measurements $C \sim 2\ \mu F$ and $R \sim 1\ M\Omega$. The dc current can be measured using a switch (not shown) prior to the noise measurements; during the noise measurements the ammeter is disconnected to prevent noise contamination. Great care was taken to eliminate all extraneous noise (i.e. 60 Hz and harmonics) via prudent grounding and shielding, though unavoidably a few discrete lines still remain which can be ignored during the data analysis. Prior to all measurements, the sample was annealed at 450K for 2 hours in order to eliminate any light-induced defects[39] and remove any surface adsorbates.[193]

Assuming one has a Gaussian noise source, all of the information concerning the current fluctuations is contained in the two-point autocorrelation function, which is a second order moment of the current; the power spectrum is essentially the Fourier transform of the autocorrelation function. If the noise source is non-Gaussian in nature, then higher order moments can contain non-trivial information that can be probed using techniques such as the second spectrum or inter-octave correlations. In this thesis, the inter-octave correlations were examined to establish the degree of Gaussian character of the noise. The power in the $i^{th}$ octave is the sum of the noise power from the frequency $f_0$ to $2f_0$, as defined in eqn. 4.10:

$$O_i = \sum_{f=2^i f_0}^{2^{i+1} f_0} S_1(f) \qquad (4.10)$$

The correlation coefficient between the $i^{th}$ and $j^{th}$ octave ($\rho_{ij}$) is defined as:

$$\rho_{ij} = \frac{\sum_{n=1}^{N_S} \left(O_{i,n} - \langle O_i \rangle\right)\left(O_{j,n} - \langle O_j \rangle\right)}{(N_S - 1)\sigma_i \sigma_j} \tag{4.11}$$

where ‹$O_i$› and $\sigma_i$ are the average and standard deviation respectively for the $i^{th}$ octave and $N_S$ is the number of individual power spectra. In order to more easily plot these data, the correlations coefficients are often averaged for a particular octave separation:

$$\langle \rho_k \rangle = \sum_{i=1}^{M-k} \rho_{i(i+k)} \tag{4.12}$$

where $k$ is the octave separation and $M$ is the total number of octaves.

## Chapter 5

## RESULTS FROM DOPED MIXED-PHASE SILICON

### 5.1 Structural Data

The films discussed in this thesis range from completely amorphous to having a crystalline fraction ($X_C$) of almost 30%, determined from the Raman spectra in figure 5.1. We define completely amorphous as having a crystalline content below the detection limit of Raman, estimated to be ~2%, and denote this film as $X_C$ = 0%. The peak positions for both the nanocrystalline phases are very similar for all the films, indicating a constant nanocrystallite size.

X-ray diffraction (XRD) analysis on these films reveals grain sizes of approximately 15 nm for the (111) direction and about 7 nm in the (220) and (311) directions (figure 5.2). The differences in the crystalline sizes along different lattice directions could be due either to elongated grains or to a bimodal distribution of crystallites. The ratio of the scattering intensities is consistent with randomly oriented grains, where one expects a (111)/(220) ratio of 0.55,[197] in good agreement with the measured value of ~0.5. A ratio of ~0.5 is typically measured for powders of silicon nanocrystals (ncs) for which no preferential orientation is assumed.

Due to the low amount of crystalline material in the $X_C$ < 20% films, no useful XRD spectra could be obtained for these mostly amorphous films. However, the XRD spectra of two samples with $X_C$ = 36% and 60% (figure 5.2) agrees well with the results from the $X_C$ = 29% sample. All of the samples were grown under very similar conditions and the nc-Si Raman peak position is the same for all of the samples, providing evidence

that the grain sizes for the low $X_C$ films are similar to that in films with higher crystalline content. The highest $X_C$ films were not included in the electronic measurements due to unintentional Indium impurities at the $10^{-4}$ to $10^{-3}$ level that strongly affected their electronic properties.

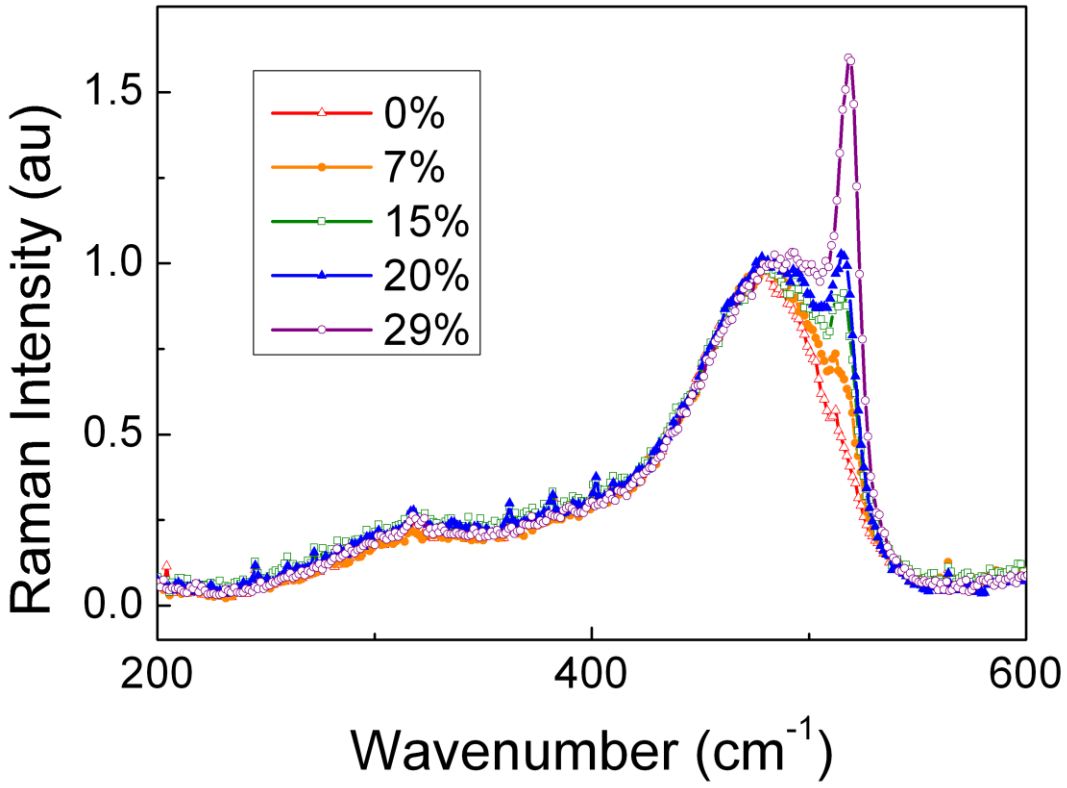


Figure 5.1: Raman spectra for the a/nc-Si:H films studied in this work, with crystal fractions ($X_C$) ranging from 0 to 29%. The crystal fraction is assigned based on the integrated intensities of the a-Si TO peak (~480 $cm^{-1}$) and the nc-Si TO peaks (500 – 520 $cm^{-1}$) as described in section 4.1.2.

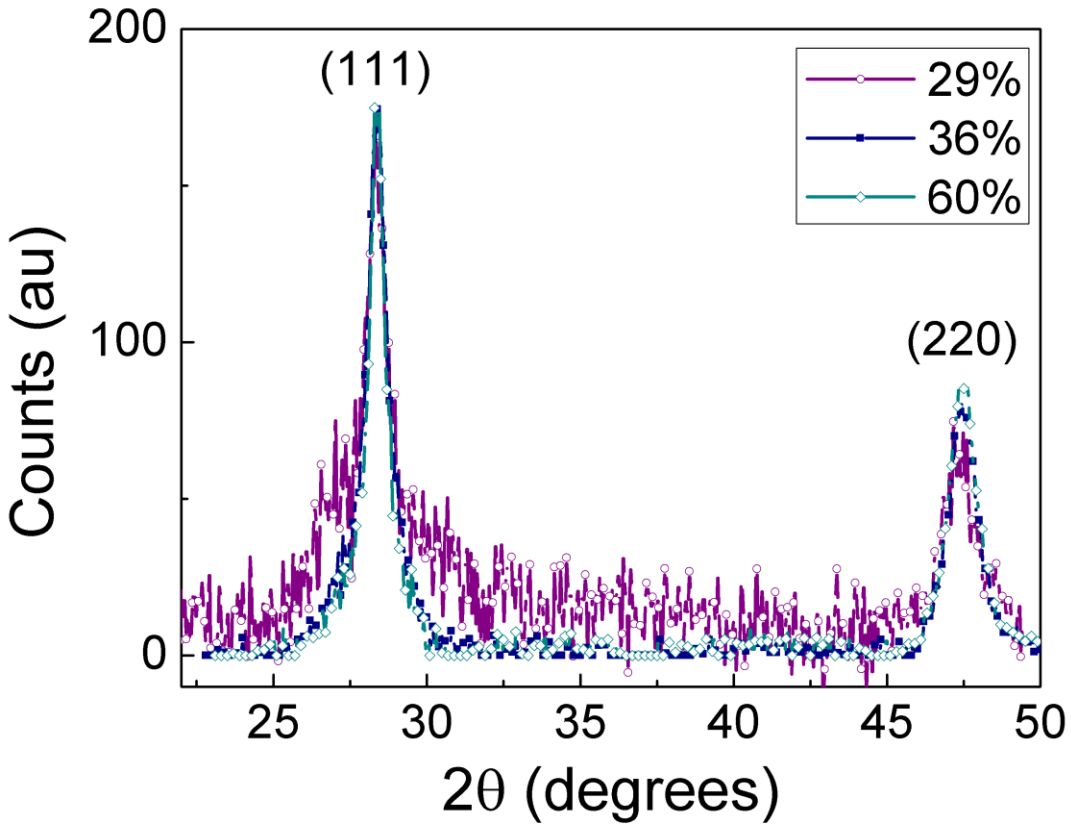


Figure 5.2: X-ray diffraction (XRD) data for the $X_C$ = 29% film studied in this work, as well as for two other films with $X_C$ = 36 and 60%, grown under similar conditions. All three films exhibit very similar peak widths and ratios of peak heights. The bulge for the 29% film near the base of the (111) peak is due to either incomplete background subtraction or scattering from the amorphous phase.

Only one sample on a silicon wafer substrates could be collected and analyzed using Fourier transform infrared (FTIR) spectroscopy ($X_C$ = 29%). Infrared (IR) spectra were obtained for the $X_C$ = 0, 15 and 20% samples using Raman spectroscopy, which can

detect Si-H vibrational modes, albeit at a much lower signal-to-noise ratio; both the FTIR and Raman IR absorption spectra are plotted against wavenumber in figure 5.3. The data obtained via Raman were processed with a low-pass Fourier transform filter to reduce excess high frequency noise in the data. No useful data could be obtained using either

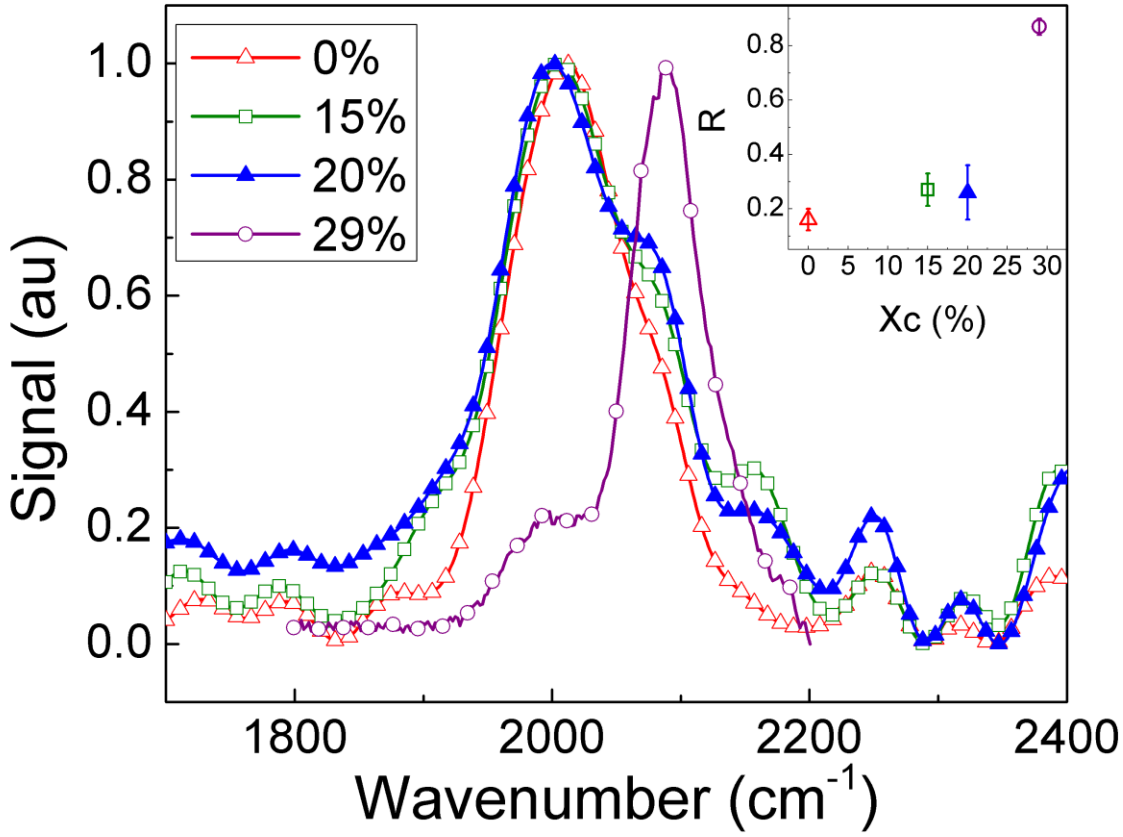


Figure 5.3: Infrared spectra from the $X_C$ = 0, 15, 20 and 29% films. The data from the 0, 15, and 20% samples were obtained via Raman spectroscopy on Corning 1737 substrates, while the $X_C$ = 29% data were obtained via traditional FTIR on a silicon wafer. The inset plots the change in the microstructure factor *R* with $X_C$, showing an increase in R with increasing $X_C$.

technique for the $X_C$ = 7% sample. Using the microstructure factor (*R*) defined in section 4.1.1, we see that the 0% sample has an *R* of 0.16, and there is a clear increase in *R* as the crystal content is increased, up to 0.87 for the 29% sample. The inset in figure 5.3 illustrates the change in *R* as a function of $X_C$. This is consistent with what was previously observed in undoped a/nc-Si:H films grown using the dual-plasma co-deposition method.[116] The increase in the absorption at 2090 $cm^{-1}$ with $X_C$ suggests that the additional hydrogen signature at 2090 $cm^{-1}$ comes from a heavily hydrogenated region surrounding the nanocrystallites, commonly referred to as the grain boundary region. This identification is supported by FTIR experiments by other groups, which suggests that absorption at higher wavenumbers, in addition to being from clustered Si-H or $Si-H_2$ in the amorphous phase, could be due to Si-H bonds on the crystallite surface.[172,198]

### 5.2 Conductivity Data

The conductivity data are displayed in an Arrhenius plot in Fig. 5.4. The films with the lowest $X_C$ (0, 7%) demonstrate activated conduction with an activation energy ($E_A$) of 0.25 and 0.29 eV respectively, as is typically observed for n-type doped a-Si:H. For the 15% film, non-activated conduction begins to dominate at low temperatures, with activated conduction above room temperature. For the 20 and 29%, non-activated conduction is observed for most of the temperature range.

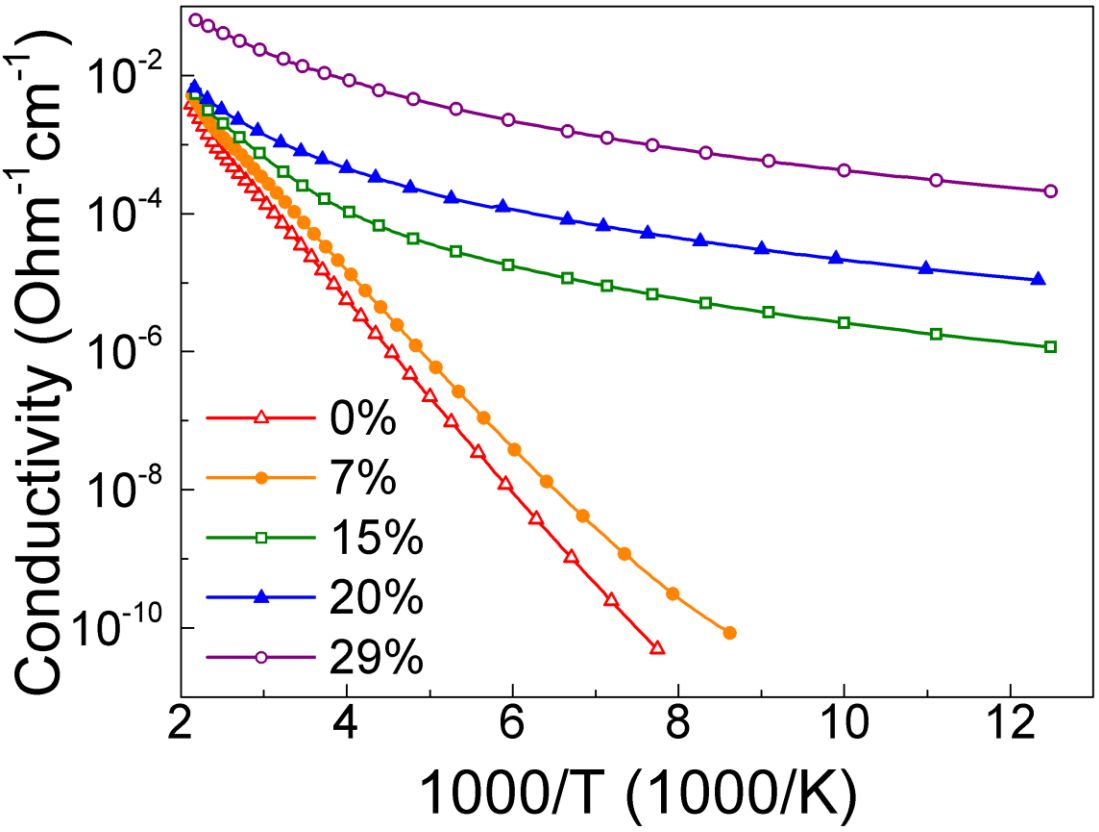


Figure 5.4: Arrhenius plot of the dark conductivity of the films in Fig. 5.1. Data were collected from 10 to 470K, but to clearly show the difference between the activated ($X_C$ = 0, 7%) and the non-activated samples ($X_C \geq 15\%$), only data down to 80K are plotted.

The reduced activation energy, $w(T)$, is plotted on a log-log scale as a function of temperature in Fig. 5.5. For the low $X_C$ films (0, 7%), the $w(T)$ plot confirms the activated behavior observed via the Arrhenius plot. In addition, the well-known shift in the activation energy due to thermal equilibration effects is present at 410K,[38] confirming that conduction occurs through the n-type doped a-Si:H matrix for these films. The 15% film displays activated conduction at high temperatures, a power-law temperature

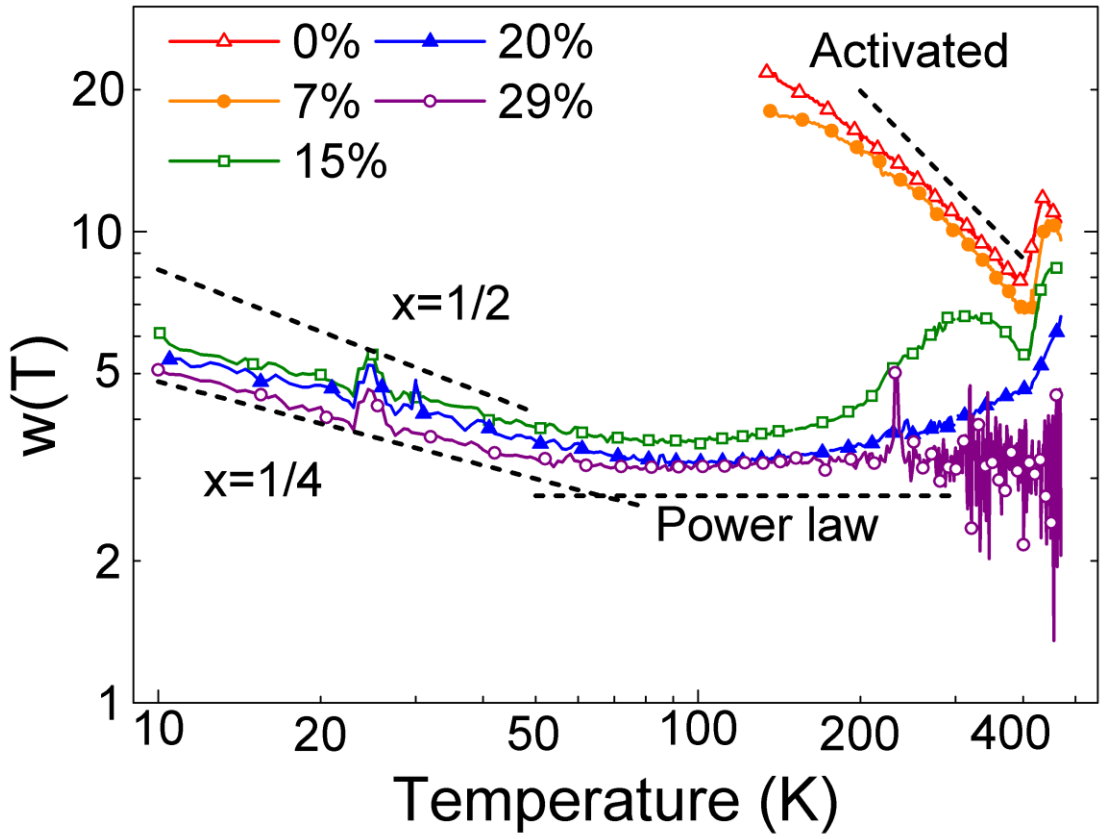


Figure 5.5: Log-Log plot of the calculated "reduced activation energies," $w(T) \approx T^x$ against temperature, for the a/nc-Si:H films with $X_C$ ranging from 0% to 29%, showing the transition from activated conduction to power-law behavior to Exp-VRH as the temperature is lowered. Slopes expected for activated conduction ($x$ = 1), ES-VRH ($x$ = ½), Mott-VRH or Exp-VRH ($x$ = ¼) and power-law ($x$ = 0) are displayed (dashed lines) for comparison.

dependence below ~300K, followed by a shift to Exp-VRH below ~50K. For the 20 and 29% samples, both the VRH and power-law regimes are clearly present. The 20% sample also displays a small amount of activated conduction at the highest temperatures,

while the 29% sample shows no activated conduction throughout the temperature range investigated.

Each data set that displayed multiple transport mechanisms ($X_C$ = 15 – 29%) was fit over their full temperature range using an expression that included the three possible conduction mechanisms:

$$\sigma_{tot} = \sigma_{VRH} + \sigma_{MPH} + \sigma_{ACT} \tag{5.1}$$

where $\sigma_{VRH}$, $\sigma_{MPH}$ and $\sigma_{ACT}$ represent the contribution to the conductivity for variable range hopping (VRH), multi-phonon hopping (MPH) and activated conduction, respectively. At the lowest temperatures, VRH was the only mechanism active, so this expression was considered first and the resulting fitting parameters were fixed for the remainder of the temperature range. In addition, the fit was constrained by the reduced activation energy, $w(T) = d\ln\sigma/d\ln T$, which proved to be much more sensitive to changes in the fit parameters. It was found that many fit parameters that yielded good fits to the conductivity data were not consistent with the temperature dependence of the reduced activation energy, $w(T)$. In Figure 5.6, the fits to the conductivity data are plotted, with the data and fit lines in the top panel and the error (|measured – calculated|/measured) in the lower panel. The error is at most 10% through a wide temperature range (10 – 470K) and over several orders of magnitude in conductivity. Figure 5.7 depicts the fits to $w(T)$, where we find excellent agreement. As a result of the inherent difficulties in using an analytical form for the activated portion of the conductivity due to thermal equilibration effects, we found that simply using the 7% film's conductivity for $\sigma_{ACT}$ resulted in very

good agreement with the measured data for the 15 and 20% films. The 29% sample required no activated component in order to be fit over the entire temperature range.

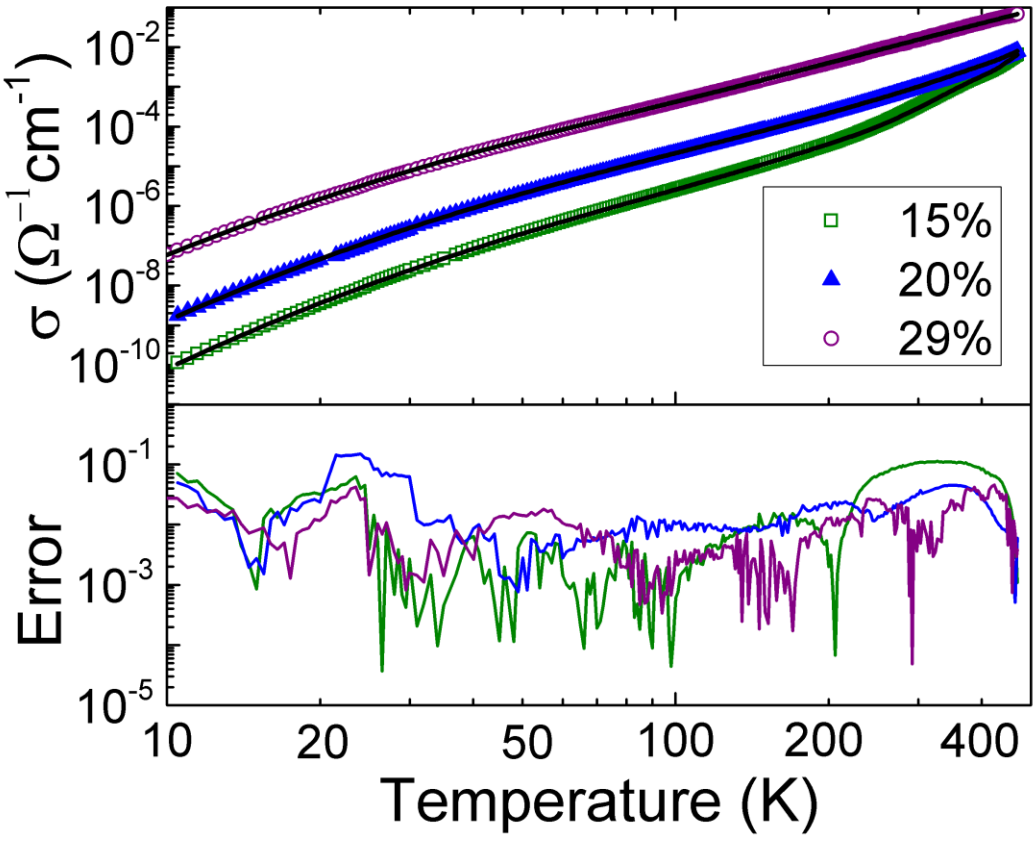


Figure 5.6: Log-log plots of the conductivity against temperature, showing fits to the conductivity data including all the transport mechanisms: Exp-VRH, MPH and activated. The error, |measured – calculated|/measured, for all the samples is shown in the lower panel. The activated term was only needed for the 15 and 20% samples. For clarity, only every third data point is plotted.

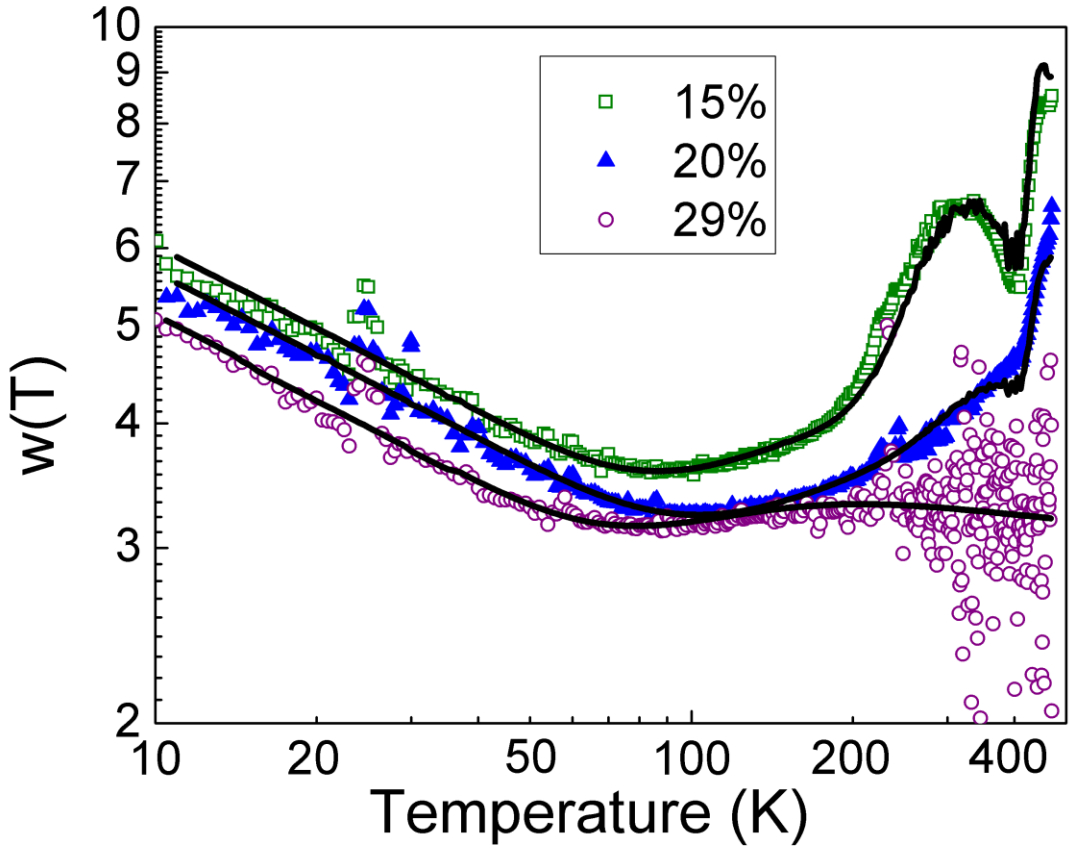


Figure 5.7: Log-log plot of the measured and calculated values of the reduced activation energy, $w(T)$ against temperature, where the calculations include all the conduction terms discussed here: Exp-VRH, MPH and thermally activated conduction in a-Si:H. The activated term was only needed for the 15 and 20% samples. For clarity, only every third data point is plotted.

In figure 5.8, the density of states at the Fermi level, $g(\varepsilon_F)$, determined using eqn. 2.4 and the $T_0$ value obtained from the Exp-VRH fit, is plotted as a function of $X_C$. The localization length ($\alpha$) is taken to be 1.5 nm; previous studies have measured $\alpha$ to be in the range of 1 – 1.8 nm.[119] The $g(\varepsilon_F)$ values are found to scale linearly with $X_C$,

following the relation $g(\varepsilon_F) \sim (1.3\times10^{19}\ eV^{-1}cm^{-3})\times X_C$. The expression for Exp-VRH was derived with the assumption of a spatially uniform density of states (DOS) and does not take into account the presence of an insulating amorphous phase along with the conductive nanocrystallites (ncs) through which transport is occurring. Thus as the crystal fraction is increased, we would expect the apparent DOS as measured by VRH to increase as well. Using this scaling, the $g(\varepsilon_F)$ for the nanocrystalline phase is calculated to be $\sim1.3\times10^{21}\ eV^{-1}cm^{-3}$. A linear relationship holds regardless of the estimated $\alpha$ value, but the extrapolated $g(\varepsilon_F)$ for $X_C$ = 100% varies, with $g(\varepsilon_F) \sim 7.6\times10^{20}\ eV^{-1}cm^{-3}$ and $2.6\times10^{21}\ eV^{-1}cm^{-3}$ for $\alpha$ = 1.8 and 1.2 nm respectively. The spatially heterogeneous nature of the DOS of mixed-phase silicon is important to consider when examining the resulting values for $g(\varepsilon_F)$ obtained via the $T_0$ parameter in hopping conduction and has not taken into account by other groups.[117,118]

Previous studies have identified hopping through band tail (BT) states as the limiting factor for electronic conduction in mixed-phase silicon.[54] The presence of BT states in the grain boundary regions has been invoked to account for the discrepancy between the macroscopic mobility of ~1 $cm^2V^{-1}s^{-1}$ at almost all doping levels, as measured by Hall effect in highly crystalline samples,[58] and the microscopic mobility of ~50 $cm^2V^{-1}s^{-1}$, as determined by electron spin resonance $T_1$ lifetime measurements.[58] Presumably, electrons can easily traverse a nc, but must hop through BT states in order to cross from one nc to another, with this hop being the rate limiting step in the conduction process.

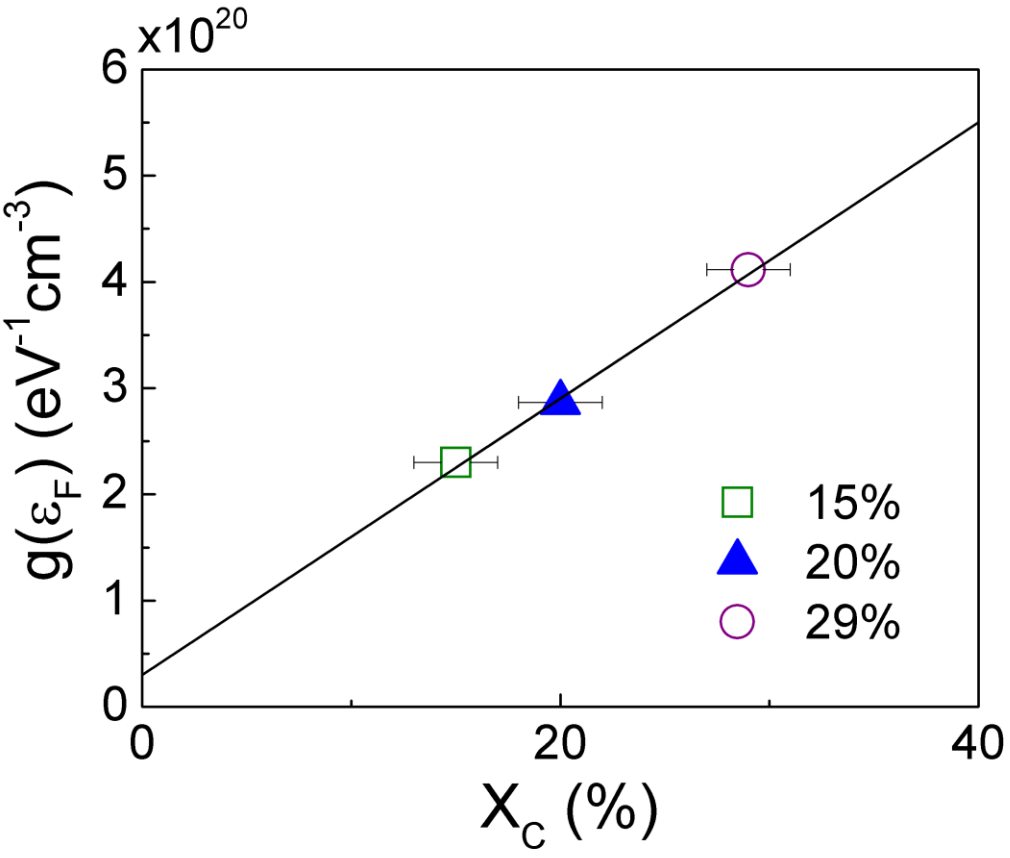


Figure 5.8: Plot of the density of states at the Fermi level, $g(\varepsilon_F)$, determined from the variable range hopping effective temperature $T_0$, as a function of the crystal fraction $X_C$. By extrapolating the linear fit, $g(\varepsilon_F) = (1.3\times10^{19}\ eV^{-1}cm^{-3})\times X_C$, to $X_C = 100\%$, the $g(\varepsilon_F)$ for the nanocrystalline phase ($X_C = 100\%$) is estimated to be approximately $1.3\times10^{21}\ eV^{-1}cm^{-3}$. A localization radius of 1.5 nm was assumed.

The observations by others of a temperature dependence $\sigma \sim \exp[-(T_0/T)^{1/4}]$ in mixed-phase silicon for many different doping levels[117–119] supports the identification of BT states, rather than active dopants, as the primary hopping sites, as BT states exist in all incarnations of mixed-phase silicon. The $T_0$ values obtained in the undoped and

lightly doped case are much larger than the $T_0$ values measured here for our heavily doped samples,[118,119] indicating a smaller $g(\varepsilon_F)$, as would be expected for hopping through states deeper in the band tails or through the valence BT, which has a broader distribution in energy than the conduction BT.[199] In Ambrosone *et al*[118] the dependence of $T_0$ on $X_C$ is opposite to what is observed here – they find that as $X_C$ increases, $T_0$ increases, reflecting a decrease in $g(\varepsilon_F)$. These authors varied $X_C$ using the RF power during film growth, which is known to also alter the quality of the material, in addition to changing the crystal fraction. Dussan and Buitrago[119] do not report the crystal fractions of their samples, but instead study the dependence of the conductivity on boron doping, finding no obvious trend of $T_0$ with doping. While the $H_2/SiH_4$ ratio is the same for all their samples, the inclusion of boron is known to alter the crystal fraction.[187,200,201]

The MPH expression for the conductivity (eqn 2.7b) contains considerably more parameters than the VRH equation. In order to minimize the number of parameters that were fit, we first attempted to fix as many of the variables as possible. The average center-to-center distance $r$ of the nanocrystals (ncs) was calculated from the crystallite size and $X_C$. Using similar arguments, we set the edge-to-edge distance of the nanocrystals $s = r - d$, where $d$ is the average diameter of the ncs (determined by XRD measurements in section 5.1). An alternative interpretation would be to use a constant $r$ and constant $s$ for all $X_C$; once the percolation threshold is reached, the electrons preferentially travel through adjacent nanocrystallites in direct contact. Even as more pathways are opened with increasing $X_C$, the distance traversed with each hop should remain constant, as should the wavefunction overlap. In this case, we assume there is a

grain boundary region of 1 nm between nanocrystallites, making $s$ = 1 nm and $r = d + s$. Using either of the two estimations of $r$ and $s$, we are left with $E_M$, $v_0$ and $p$ as fitting parameters; the results are listed in Table 5.1. Only the $E_M$ value was affected by the change in $r$ and $s$; both values are listed in Table 5.1 with the varying $r$ and $s$ value listed first and the constant $r$ and $s$ value listed second. In contrast to the works of Shimakawa and others,[67,68] the typical approximation for the density of charge carriers that are active in hopping conduction, $n_c \sim g(\varepsilon_F)k_BT$, is not used here. Instead, we estimate $n_c$ by the gas phase doping level, assuming a 50% incorporation rate of phosphorus from the gas phase to the solid phase and 100% dopant activation within the nanocrystals.[114]

The $E_M$ values listed in Table 5.1 are between 2 – 12 meV for all of the samples investigated, regardless of the values used for $r$ and $s$. The trend with $X_C$ is opposite for the two cases; $E_M$ decreases with $X_C$ for the varying case and increases with $X_C$ for constant case. Both sets of $E_M$ values are much higher than the values of 25 and 60 μeV determined by Shimakawa and coworkers in a-Ge[67] and a-C[68] respectively. Although one would expect differing $E_M$ values for various materials, a difference of a factor of several hundred is surprising considering the much smaller difference obtained for a-C and a-Ge. If $E_M$ values in the range of 10 – 100 μeV are used, and $r$ is determined from the fit to the conductivity data, then unphysically large values of $r$, on the order of a few microns are obtained, making the center-to-center distance between nanocrystals much larger than any other length scale in the problem. The parameter $v_0$ was found to be ~2.75 THz, approximately the same for all of the samples. Taking the speed of sound in silicon to be ~9000 m/s,[202] $v_0$ corresponds to a phonon wavelength of ~3.3 nm, slightly smaller

than the average radius of a nc (4.5 nm) and close to the radius in the (111) direction (3.5 nm). The measured $v_0$ represents a phonon temperature of ~130 K. Below 130 K, there is a significant drop in the phonon populations active in MPH, sharply reducing the hopping rate so that VRH dominates the conduction at the lowest measured temperatures.

| $X_C$ (%) | $\rho_{nc}$ (nc/cm$^3$) | $n_c$ (cm$^{-3}$) | $r$ (nm) | $s$ (nm) | $E_M$ (meV) | $E_M$ (meV) | $p$ | $v_0$ (THz) |
|---|---|---|---|---|---|---|---|---|
| 15 | $3.9\times10^{17}$ | $2.3\times10^{18}$ | 13.7 | 4.7 | 12.4±0.5 | 2.3±0.3 | 4.5±0.1 | 2.75±0.1 |
| 20 | $5.2\times10^{17}$ | $3.0\times10^{18}$ | 12.4 | 3.4 | 9.65±0.5 | 3.0±0.3 | 4.5±0.1 | 2.75±0.1 |
| 29 | $7.5\times10^{17}$ | $4.4\times10^{18}$ | 11 | 2 | 7.2±0.5 | 4.3±0.3 | 4.0±0.2 | 2.75±0.1 |

Table 5.1: The parameters obtained from, and used for, the MPH fits to the conductivity data. The density of nanocrystals is given by $\rho_{n,}$ calculated from $X_C$ and the known crystallite size. $r$ is set to $1/\rho_{nc}^{1/3}$, and $s = r - d$, where $d$ is the average grain diameter of ~9 nm as measured by XRD. The density of charge carriers, $n_c$, is calculated using the gas phase doping, assuming 50% incorporation in the solid phase and 100% dopant activation within the ncs. For $E_M$, two values are listed, the first for the case where $r$ and $s$ are taken from the fourth and fifth columns respectively and the second where $r$ and $s$ are assumed to be constant, with values of 10 and 1 nm respectively, as described in the text.

### 5.3 Thermal Equilibration Data

An Arrhenius plot of the thermal history dependence of the dark conductivity for cooling rates from 100 K/min to 0.1 K/min is presented in figure 5.9. For clarity, the curves for the 7, 15, 20 and 29% films have been vertically offset. It is clear that as the nanocrystallite content increases, the difference between the conductivity in the slow and fast cooled states at a given temperature decreases. In figure 5.10 we plot the conductivity gap $\sigma_{gap}$ (eqn. 4.8) at 350 K. There is relatively little change in $\sigma_{gap}$ for the low $X_C$ films, being 1.32 and 1.30 for the 0 and 7% films respectively. This is followed by a dramatic decrease to values near zero when $X_C > 15\%$, where $\sigma_{gap}$ is 0.33, 0.15 and 0.06 for the 15, 20 and 29% samples respectively.

The isothermal conductivity relaxation curves are plotted in figure 5.11 at a temperature of 410 K. The data plotted in figure 5.11 are the current as a function of time, normalized to the current at an initial time of 1 sec. For the mixed-phase films with $X_C > 7\%$, the time for the conductivity to relax to a steady state value increases and only an incomplete relaxation is recorded. Consequently for these films the current could not be normalized to both the initial and final values as needed to fit the data using a stretched exponential time dependence, precluding accurate determinations of $\beta$ and $\tau$. Fits to the two films with a complete relaxation ($X_C = 0, 7\%$) reveal virtually the same values for $\beta$ and $\tau$ of ~0.65 and ~$3\times10^3$ s, respectively. The relaxation time $\tau$ is considerably longer than in optimum-quality doped a-Si:H, typically ~100 s for this temperature. While we cannot infer accurate relaxation times for the samples with a

substantial crystalline fraction, we can qualitatively say that the relaxation time increases as the crystal fraction is increased.

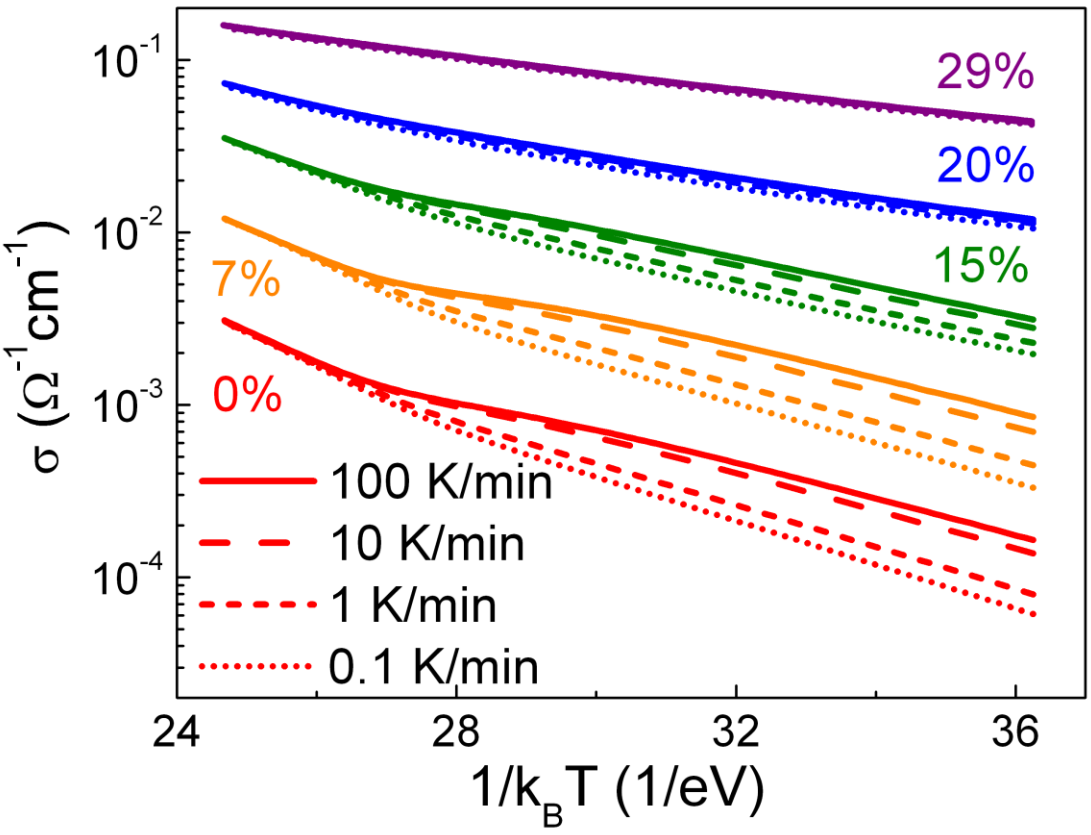


Figure 5.9: Arrhenius plot of the conductivity for the mixed-phase films as a function of cooling rate following a high temperature anneal. There is a strong decrease in the sensitivity of the conductivity to the cooling rate following a high temperature anneal as the crystal fraction is increased. For clarity, the curves for the 7, 15, 20 and 29% films have been vertically offset.

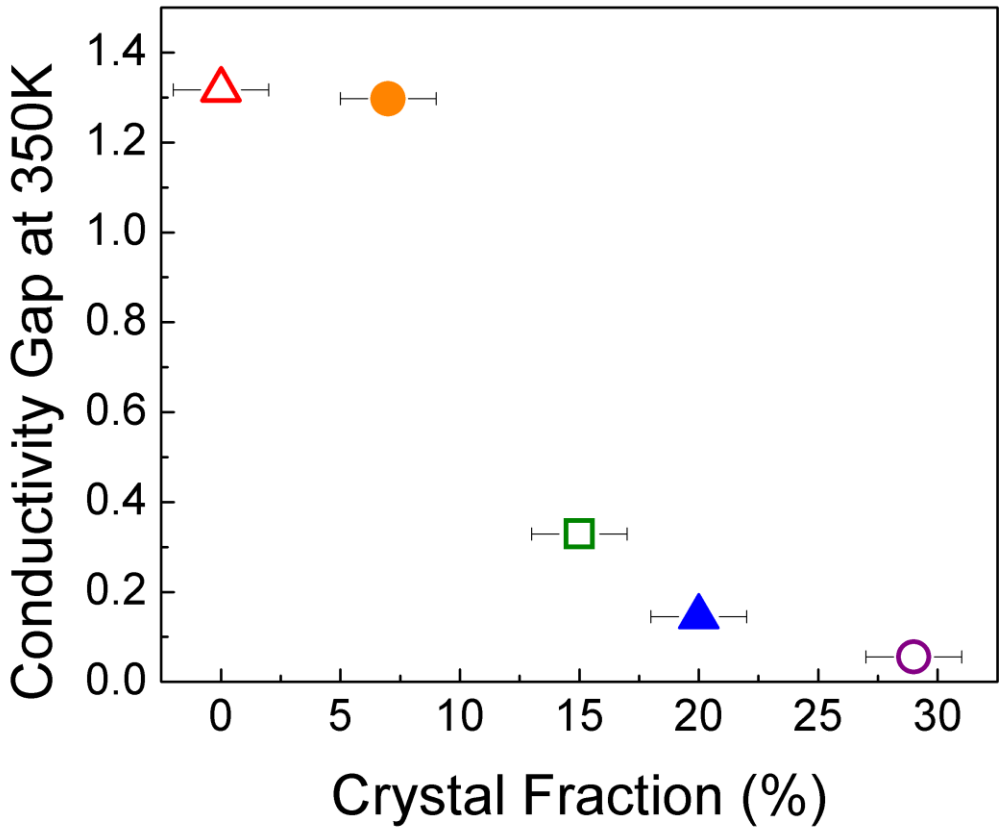


Figure 5.10: Plot of the conductivity gap as a function of crystal fraction. There is a dramatic decrease starting with the Xc = 15% film. By the $X_C$ = 29% film almost no difference is observed in the conductivity measured at different cooling rates following a high temperature anneal.

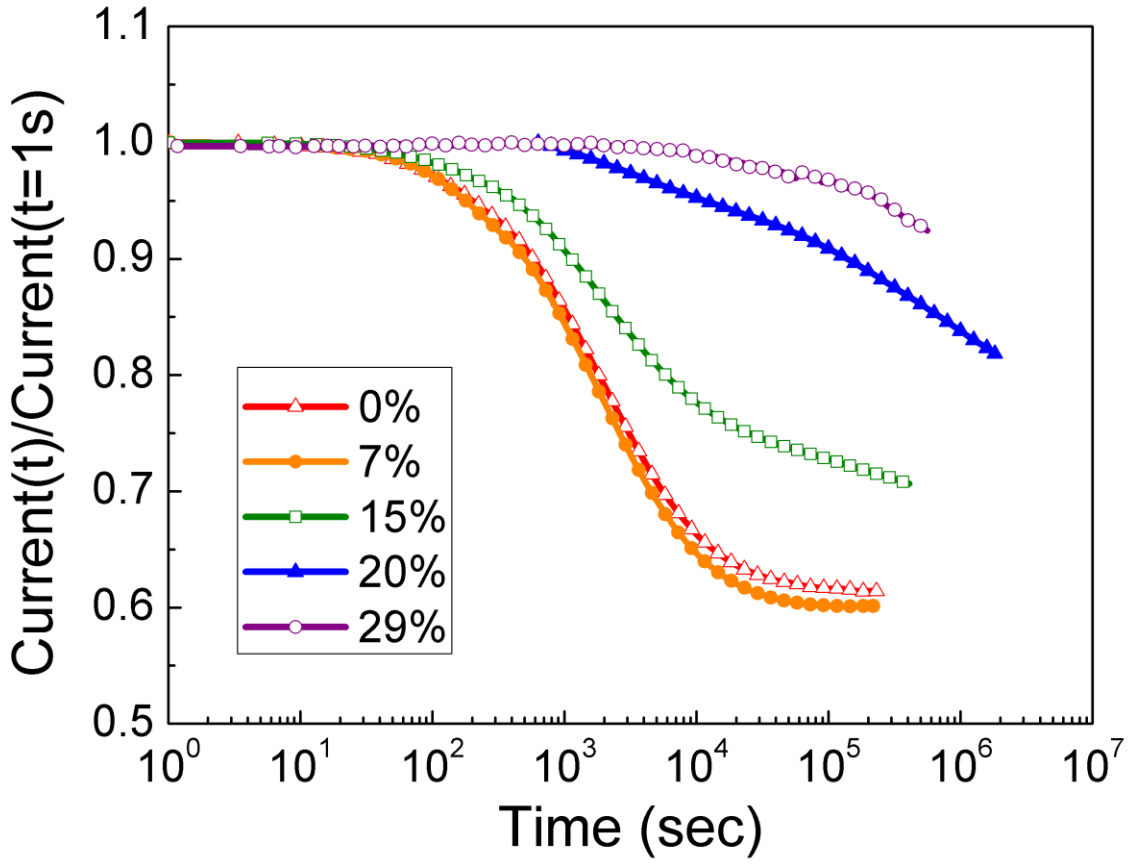


Figure 5.11: Isothermal relaxation measurements at 410 K for the mixed-phase a/nc-Si:H films. The 0 and 7% show very similar relaxation behavior, with a noticeably slower decay as $X_C$ further increases. Some relaxation is still observed in the 29% sample. As a time scale reference, $10^6$ s is approximately 12 days.

**5.4 Noise Data**

Sample noise spectra for the $X_C$ = 0 – 20% films taken at 320 K are plotted in figure 5.12. The noise magnitudes of the low $X_C$ films (0, 7%) are roughly equivalent, but the noise magnitudes decrease with increasing $X_C$, with the $X_C$ = 20% film having about an order of magnitude lower noise level when compared to the 0% sample. The

noise signals have been normalized by the square of the mean current to determine the normalized noise, $s(f)$, in order to adjust for changes in the resistivity between different samples. Due to excessive noise from the contacts on the 29% sample, accurate noise measurements could not be made. For the other four films, both the linearity, symmetry (with respect to voltage bias direction) and reproducibility of the noise measurements were checked to ensure that the data reflected bulk noise events and did not arise from contact noise.

To examine the temperature dependence of the noise magnitudes, we plot the normalized noise power at 10 Hz, $s$(10 Hz), over the temperature range of 240 – 450 K (figure 5.13a). The higher conductivity of the more crystalline samples allowed for measurements to the lowest temperature obtainable by our noise measurement system, ~240 K, while noise measurements of the more resistive amorphous films were restricted to 320 K and above. There is significant scatter in the low $X_C$ data due to the spectral wandering observed in these films, which is comparable to that observed in previous studies of a-Si:H.[100,101] To illustrate the range of values obtained for the low $X_C$ films, data are presented for two full temperature cycles. The $X_C$ = 15 and 20% films displayed excellent reproducibility between runs. For the 15% sample, the noise power is relatively temperature independent for temperatures above 350 K, followed by a steep increase in the noise power at lower temperatures. The $X_C$ = 20% sample also displays an increase in noise power below 350 K, though the rise is not as sharp as with the 15% sample. The spectral slope, $\gamma$ in $1/f^{\gamma}$, displays a general increase with increasing temperature as presented in figure 5.13b. The $\gamma$ values are all between ~0.9 and 1.2, within the range of

what can be called "1/*f* noise." The mostly amorphous samples ($X_C$ = 0, 7%) show greater scatter and thus no unambiguous temperature dependence, as previously observed in doped a-Si:H without nanocrystalline inclusions,[100] while the more crystalline samples (15, 20%) display a trend of increasing $\gamma$ with increasing temperature.

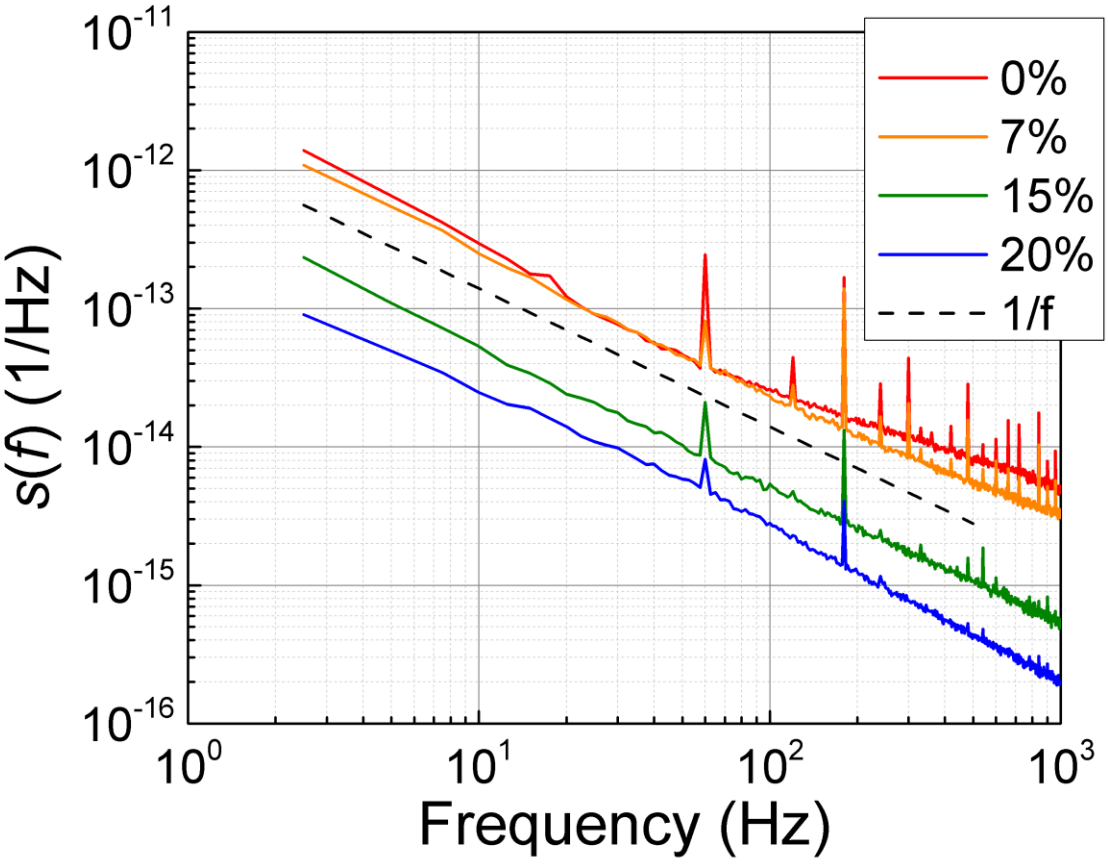


Figure 5.12: Log-log plot of normalized noise power *s*(*f*) against frequency resulting from 1024 averages taken at 320 K (after background subtraction) for the a/nc-Si:H films as $X_C$ increases from 0 to 20%. All spectra exhibit 1/*f* behavior and there is a decrease in noise magnitude with increasing crystal fraction.

The average inter-octave correlations for a given octave separation, $\langle \rho_k \rangle$, which represents correlations between fluctuators with different characteristic frequencies, are plotted in figure 5.14 for the $X_C$ = 0 – 20% samples at 320 K. We see from figure 5.14 that the low $X_C$ samples generally have larger inter-octave correlations than the high $X_C$ films, which exhibit Gaussian noise at 320 K. The inset of figure 5.14 displays the temperature dependence of the correlations, which can be determined by plotting the correlations between nearest neighbor octaves, $\langle \rho_1 \rangle$, as a function of temperature. There is no temperature dependence of the correlations for the low $X_C$ films (0, 7%), as has been previously observed with doped a-Si:H,[101] while the high $X_C$ films (15, 20%) show a marked increase in the inter-octave correlations above ~420 K, with essentially zero correlations below this temperature.

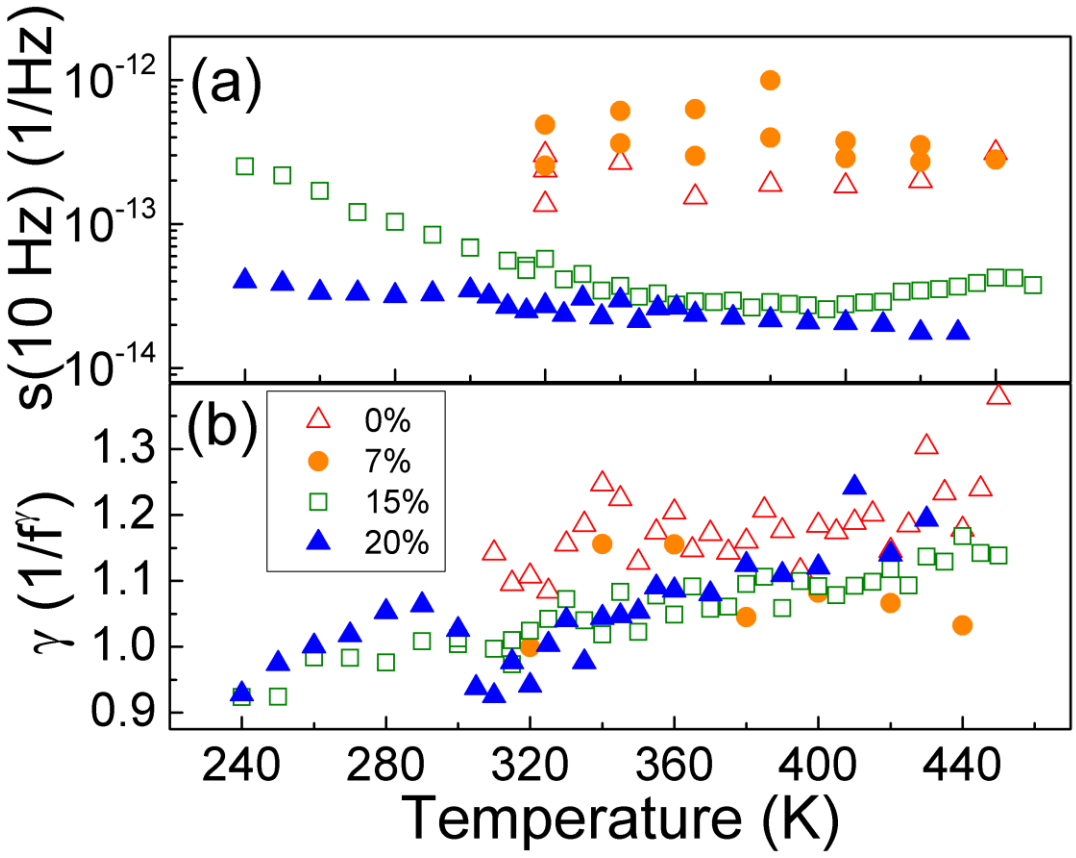


Figure 5.13: (a) The normalized noise magnitude at 10 Hz, *s*(10 Hz), plotted against temperature for all crystal fractions. There is significant scatter for the low $X_C$ films (0, 7%) due to spectral wandering. The noise magnitudes of the higher $X_C$ films (15, 20%) are very reproducible over this temperature range. (b) The power law fit ($\gamma$ = d(*log S*)/d(*logf*)) to the noise between 2.5 – 100 Hz as a function of temperature. There is a general trend of increasing $\gamma$ with increasing temperature for the high $X_C$ films (15, 20%), starting at ~0.9 at 240 K to 1.2 at 450 K. The low $X_C$ (0, 7%) films show no significant temperature dependence.

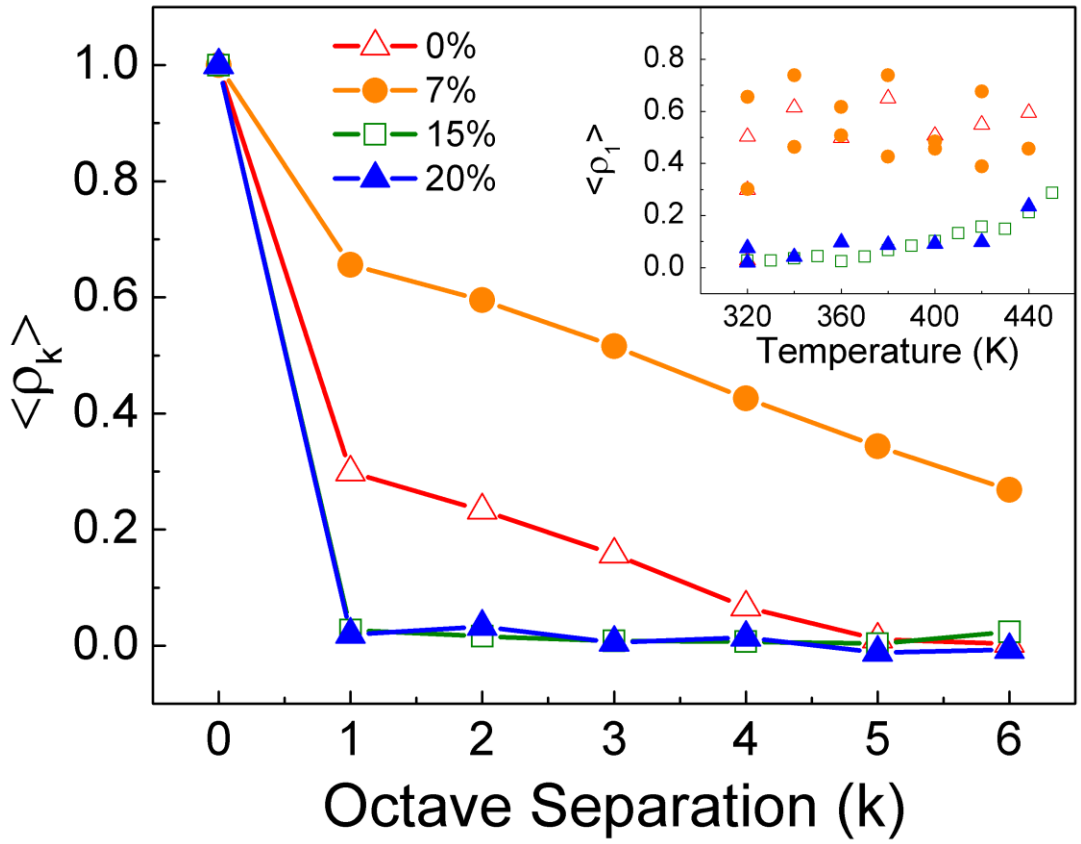


Figure 5.14: Plot of the average inter-octave correlations ‹$\rho_k$› against octave separation, for all four films at 320 K. The low crystal fraction films exhibit non-Gaussian characteristics and also significant spectral wandering, while the $X_C$ = 15 and 20% are Gaussian and relatively stationary at temperatures less than 420 K. The temperature dependence of the nearest neighbor octave correlations ‹$\rho_1$› is plotted in the inset. There is an increase in the correlations for the high $X_C$ films around 420 K and no significant temperature dependence for the low $X_C$ films; two separate temperatures sweeps for the low $X_C$ films are presented to illustrate the variations with time.

## 5.5 Discussion

In the low temperature regime the temperature dependence of the conductivity suggests that Exp-VRH through band tail (BT) states is the dominant electronic transport mechanism. The magnitude of the conductivity in the Exp-VRH hopping temperature range is determined by the DOS at the Fermi level, $g(\varepsilon_F)$, where the BT states most likely reside in the grain boundary (GB) regions surrounding the nanocrystallites. From an extrapolation of our $T_0$ values, we have determined $g(\varepsilon_F)$ for the GB region surrounding the nanocrystals to be ~$1.3\times10^{21}$ $eV^{-1}cm^{-3}$. The GB region more closely resembles a-Si:H rather than nanocrystalline silicon, due to its disordered nature and the inclusion of hydrogen, resulting in a band gap of ~1.8 eV, larger than the gap in the crystalline regions (1.1 eV).[54] The nanocrystals in these films are too large to exhibit significant quantum confinement of their electronic states. Previous studies have found that the difference in the band gaps between amorphous and crystalline silicon results in a band offset primarily between the valence bands (VBs), with the conduction bands (CBs) being quite close in energy.[123] At the doping levels investigated here (~$1.5\times10^{19}$ $P/cm^{-3}$), well above the metal-insulator transition in crystalline silicon (~$4\times10^{18}$ $cm^{-3}$),[58] the crystalline regions should be degenerately doped, setting the Fermi level near the CB edge. This forces the Fermi level to lie very close to the conduction band in the grain boundary region as well, consistent with our estimation of a large $g(\varepsilon_F)$. This situation is depicted in figure 5.15, which shows the interface between two nanocrystallites including the GB region.

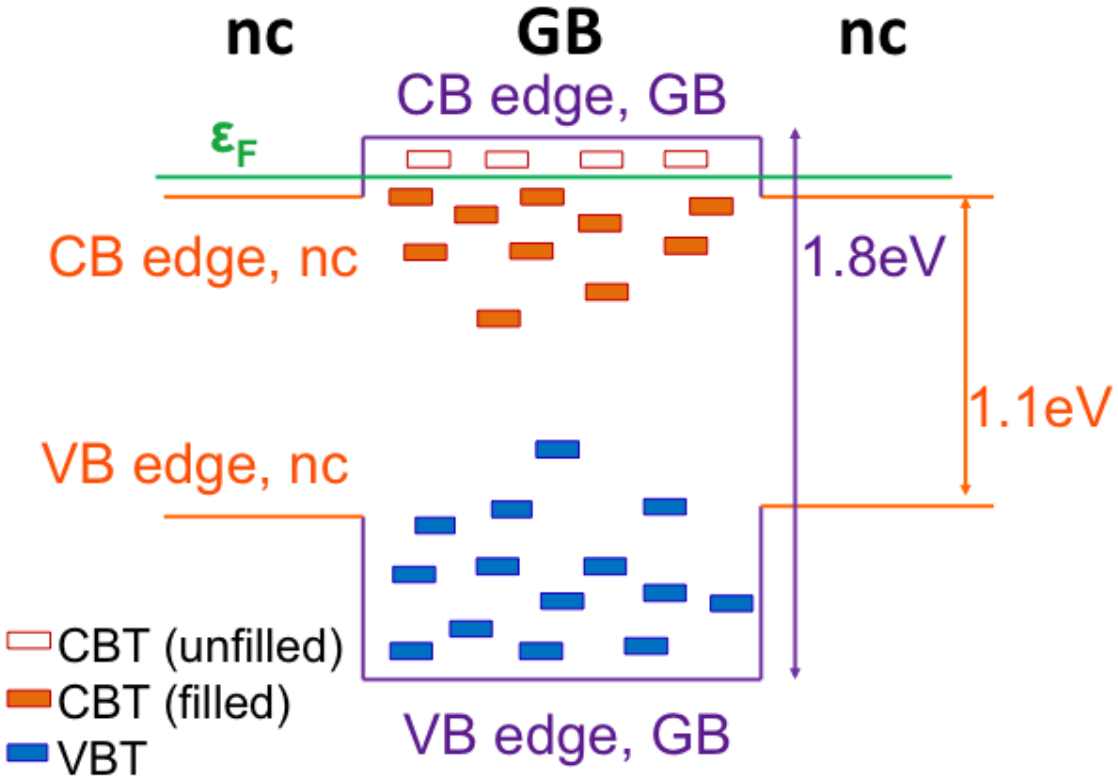


Figure 5.15: Cartoon sketch of the interface between two nanocrystallites (ncs) including the grain boundary region (GB) between them. The majority of the band offset between crystalline and amorphous silicon is between the two valence bands, with the conduction bands being close in energy. The Fermi level is above the conduction band edge in the ncs, forcing it to reside in a high density of conduction band tail (CBT) states in the GB due to the asymmetric band offset.

This same band diagram can also be applied to the multi-phonon hopping (MPH) transport region. We suppose that the electrons must absorb energy from phonons in order to hop between ncs. The total energy required for a hop is $p \times h\nu_0$ , which is ~50

meV, in the range of the CB offset between the amorphous and crystalline silicon.[123] The hops in the MPH regime may in fact be from the nanocrystalline CB into the CB of the GB, rather than hopping through the GB region at the Fermi level.

At higher temperatures, the picture becomes more complicated as we need to consider the possibility of transport occurring in both the nanocrystalline and amorphous phases. For the 29% sample, no activated component is required to fit the data over the entire temperature range (10 – 470 K) measured here, indicating that the amorphous matrix does not contribute a significant fraction of the current at any temperature for this film. The transport in doped a-Si:H cannot be fit accurately by a simple sum of activation energies due to thermal equilibration effects,[37] observable in both the conductivity data from section 5.2 and the thermal equilibration data in section 5.3. Rather, there is an abrupt change in the activation energy, which manifests itself as a kink in the conductivity at a particular temperature, instead of a continuous, smooth variation of the conductivity as expected if there were two competing transport mechanisms with different activation energies. To represent the contribution due to conduction through the a-Si:H matrix, we used a scaled version of the 7% sample's conductivity for the activated portion of the 15 and 20% sample's calculated conductivity. The 7% film does not display hopping transport over the measured temperature range, but only thermally activated conduction (including thermal equilibration) associated with doped a-Si:H. As seen in figure 5.6 and 5.7, this simple procedure provides very good agreement with the measured conductivity and $w(T)$ values. From this we can deduce that the conduction at high temperatures in the 15 and 20% samples is indeed through the a-Si:H, and does not

result from activated conduction in the ncs, and moreover, that the amorphous tissue has not substantially changed from the 7% film.

Using our model of conduction in mixed-phase silicon, the fractional conductivity due to each transport mechanism is computed as a function of temperature, defined as $\sigma_i/\sigma_{tot}$, where $i$ = *VRH*, *MPH* or *ACT*, shown in figure 5.16. The increasing importance of MPH and the decreasing contribution from activated conduction as $X_C$ increases is visible, until there is no measurable activated conduction in the 29% sample. For all of the samples, VRH dominates over a comparable range, with the persistence of VRH to high temperatures increasing with $X_C$. One point that is clearly illustrated in figure 5.16 is that it is unlikely that only one mechanism will dominate charge transport over any given temperature range, making it difficult to describe the conductivity data from mixed-phase silicon using a single charge transport process.

These calculations allow us to make quantitative comparisons between the thermal equilibration effects in the low $X_C$ films and the 15 and 20% films. Examination of the conductivity gap ($\sigma_{gap}$) plot (figure 5.10), indicates that the $X_C$ = 0 and 7% samples both have comparable values of $\sigma_{gap} \sim 1.3$, while for the $X_C$ = 15% and the 20% samples, we observe $\sigma_{gap}$ values of 0.33 and 0.15 respectively. Using the $\sigma_{gap}$ of the 0% film (1.32) as a reference, where 100% of the conduction is through the amorphous silicon, we can calculate the $\sigma_{gap}$ that one would expect for the higher $X_C$ films using the activated fractional conductivities ($\sigma_{ACT}/\sigma_{tot}$) at the temperature where the conductivity gap was measured (350 K). For the 15% and 20% samples, $\sigma_{ACT}/\sigma_{tot}$ = 0.29 and 0.13 respectively at 350 K and we predict a $\sigma_{gap}$ of 0.38 and 0.18, in very good quantitative agreement with

the observed values of 0.33 and 0.15.

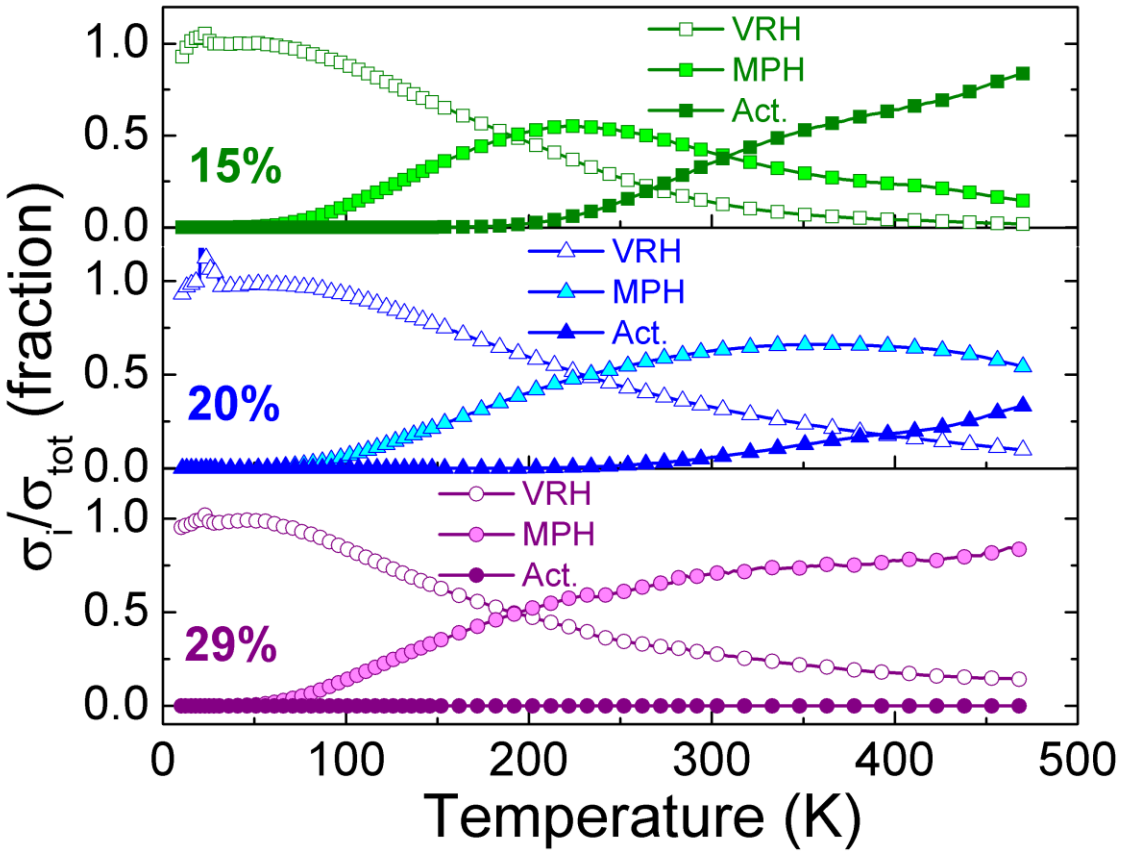


Figure 5.16: Calculated fractional conductivity, $\sigma_i/\sigma_{tot}$ for each electronic transport mechanism plotted against temperature over the temperature range 10 – 470 K. The 29% film (purple, lower) has no significant thermally activated component. We observe an activated component in the 20% sample (blue, middle) and find a significant activated fraction in the 15% sample (green, top). All samples show a mix of conduction mechanisms for temperatures greater than 100 K. For clarity, only every fifth data point is displayed.

Similar calculations can be carried out for the relaxation data where at 410 K $\sigma_{ACT}/\sigma_{tot}$ = 0.66 and 0.20 for 15 and 20% films respectively. The amorphous films relax from $i/i_0$ = 1.0 at $t$ = 1 s to $i/i_0$ ~ 0.6 in their fully relaxed state, a change of ~0.4. Scaling this change with the fractional conductivities, we would predict a change of about 0.25 and 0.08 for the 15 and 20% samples respectively. While the prediction agrees reasonably well for the 15% sample (~0.3 change), the 20% sample relaxes significantly more than we would expect based on this simple scaling argument; the measured relaxation is ~0.15. Given the increase in the infrared absorption microstructure factor ($R$) with increasing $X_C$, one would actually expect the samples to relax *less* as the crystal fraction is increased, based upon observations by Kakalios and Street on n-type doped a-Si:H films deposited under high RF power conditions.[38] These deposition conditions produce sub-optimal quality films with high $R$'s and poorer electronic properties. Furthermore, the authors measured an increasing thermal equilibration temperature ($T_E$) with decreasing film quality. Given our increasing $R$, often used as an indicator of film quality, we would expect a similar shift in $T_E$ to higher temperatures. However, as is evident in the conductivity data, $T_E$ has no measurable shift with increasing $X_C$. Even though $T_E$ does not appear to be sensitive to the increase in $X_C$, the relaxation time is increased, as deduced from the much slower relaxation of the 15 and 20% samples compared to the 0 and 7% samples, which both undergo a full relaxation in ~$10^4$ seconds.

As a final point concerning the thermal equilibration measurements, it should be noted that the 29% sample, despite the fact that there is no measurable conduction

through the amorphous phase, still exhibits a small, slow relaxation. It is possible that relaxations in the amorphous tissue closest to the grains can affect the defect (trap) density at the grain boundary, leading to a slight, but measurable change in the conductivity, though admittedly this is quite speculative at this point. A more complete set of isothermal relaxation experiments at different temperatures, along with measurements of the hydrogen diffusion coefficient, could provide important information regarding thermal equilibration in the mixed-phase samples.

The noise data measured at high temperatures (above 300 K) supports the conclusions of the conductivity and thermal equilibration data. The $X_C$ = 0 and 7% samples display noise properties that are typical of amorphous silicon, as observed by many researchers at the University of Minnesota.[99,101,203] The 15 and 20% samples display noise magnitudes about an order of magnitude lower than the amorphous films and Gaussian behavior until ~400 K, where a noticeable increase in the correlation coefficients is observed. While it is tempting to simply ascribe this to the increasing fraction of the conduction that is due to the amorphous channel, determined to be 0.64 and 0.19 for the 15 and 20% samples respectively at 400 K, the fact that the correlation coefficients are the same for both films despite the large difference in the amorphous fractional conductivity is puzzling.

The noise measurements indicate an increase in the noise magnitude as the temperature is lowered below room temperature for both the 15 and 20% films; the increase is much steeper in the 15%. This feature in the noise data is interesting, but with the limited data available, no definitive statements can be made regarding its origin.

Noise data at temperatures lower than were possible with the current measurement apparatus will be necessary to further investigate the nature of this feature in the noise spectra.

## Chapter 6

## CONCLUSIONS AND FUTURE DIRECTIONS

In this thesis, I have identified three conduction mechanisms in doped mixed-phase silicon thin films – variable range hopping (Exp-VRH) through exponential band tail states in the grain boundary region, multi-phonon hopping (MPH) between nanocrystalline grains and activated conduction in the amorphous silicon matrix. A thorough analysis of the transport measurements, including conductivity, thermal equilibration and noise spectroscopy, has been presented and quantitatively correlated with theory. Based on the resulting parameters obtained from the data analysis, it is suggested that the transition from Exp-VRH to MPH is governed by phonon populations. Below ~130 K, the phonon population decreases rapidly, limiting the hopping rate associated with MPH. As is evident through conductivity and thermal equilibration measurements, at high temperatures and for $X_C < 20\%$, the transport is dominated by traditional activated transport through the a-Si:H tissue. Measurements of thermal equilibration effects and estimates of the fractional conductivity due to the activated component are in quantitative agreement. The results of noise spectroscopy measurements show an abrupt change in the magnitude and character of the current fluctuations as the crystal fraction is increased. There is a significant decrease in the noise power magnitude and a rather abrupt change from non-Gaussian to mostly Gaussian characteristics, even as a large fraction of the current continues to travel through the amorphous phase. These results demonstrate that, due to the complex microstructure of mixed-phase silicon, there are likely several channels of electronic

transport that are active simultaneously. This work, in addition to providing a clear link between experiment and theory, emphasizes the importance of a sufficient dynamic range and/or multiple types of opto-electronic measurements to accurately determine the electronic transport in these technologically important materials.

While activated conduction, MPH, and Exp-VRH have been previously discussed in the amorphous and nanocrystalline semiconductor literature, the reduced activation energy analysis greatly increases confidence in the determination of the nature of the transport mechanisms compared to previous studies.[66–68,118,124] These results demonstrate that the reduced activation energy analysis is a powerful technique for elucidating the nature of charge transport in these films and other nanostructured materials.

These interesting transport studies raise many new questions. In particular, can we definitively identify the nature of the hopping sites involved in the transport? What is the dependence of transport on the crystallite size (which may give a clearer indication of the localization length involved in the hopping processes)? Our studies were done exclusively on n-type material – do similar trapping/hopping states exist for p-type mixed-phase films? The exploration of p-type materials would be particularly interesting given the very different band offsets between the conduction and valence band at the nanocrystalline/grain boundary interface and the difference in the widths of the valence and conduction band tails. Based only on the differing band tail widths, one would expect a much smaller density of states at the Fermi level for p-type materials, resulting in a larger measured $T_0$ value – indeed this is consistent with previous measurements of p-type mixed-phase silicon deposited by other groups.[119] Measurement of the hopping

parameters as a function of doping would enable the development of a more detailed model of the DOS and would provide tighter constraints for the fit parameters used to calculate the conductivity.[204] Similar studies could also be carried out using a thin film transistor structure to move the Fermi level via electrostatic gating, allowing one to map out the band tail states.[205]

Recent modifications made to the dual-chamber co-deposition system used to synthesize these materials should allow much greater control of these parameters (crystallite size, doping, film quality) and opens the door to many avenues for future research, including a large range of new composite materials that were previously impossible to make. Studies involving variations of the doping level and compensation, as well as exploring higher crystal fractions and different crystallite diameters will shed light on the nature of the hopping sites in these technologically important and complex materials.

## REFERENCES


[1] C. Wronski, B. Von Roedern, and A. Kolodziej, Vacuum **82**, 1145 (2008).
[2] C.C. Wu, S.D. Theiuss, G. Gu, M.-H. Lu, J.C. Sturm, S. Wagner, and S.R. Forrest, IEEE Electron. Device Lett. **18**, 609 (1997).
[3] A. Reznik, S.D. Baranovskii, O. Rubel, G. Juska, S.O. Kasap, Y. Ohkawa, K. Tanioka, and J.A. Rowlands, J. Appl. Phys. **102**, 053711 (2007).
[4] H. Gleskova, S. Wagner, V. Gašparík, and P. Kováč, J. Electrochem. Soc. **148**, G370 (2001).
[5] R.A. Street, *Hydrogenated Amorphous Silicon* (Cambridge University Press, 1991).
[6] W. Schülke, Phil. Mag. B **43**, 451 (1981).
[7] S.R. Elliott, Adv. Phys. **38**, 1 (1989).
[8] R.L.C. Vink, G.T. Barkema, M.A. Stijnman, and R.H. Bisseling, Phys. Rev. B **64**, 245214 (2001).
[9] K. Laaziri, S. Kycia, S. Roorda, M. Chicoine, J.L. Robertson, J. Wang, and S.C. Moss, Phys. Rev. B **60**, 13520 (1999).
[10] D.J.H. Cockayne, Ann. Rev. Mater. Res. **37**, 159 (2007).
[11] R.L.C. Vink, G.T. Barkema, and W.F. van der Weg, Phys. Rev. B **63**, 115210 (2001).
[12] W.A. Kamitakahara, C.M. Soukoulis, H.R. Shanks, U. Buchenau, and G.S. Grest, Phys. Rev. B **36**, 6539 (1987).
[13] J.M. Gibson, M.M.J. Treacy, T. Sun, and N.J. Zaluzec, Phys. Rev. Lett. **105**, 125504 (2010).
[14] M.M.J. Treacy and K.B. Borisenko, Science **335**, 950 (2012).
[15] M.M.. Treacy, J.. Gibson, and P.. Keblinski, J. Non-Cryst. Solids **231**, 99 (1998).
[16] P. Biswas, R. Atta-Fynn, S. Chakraborty, and D.A. Drabold, J. Phys. C **19**, 455202 (2007).
[17] S.N. Bogle, P.M. Voyles, S.V. Khare, and J.R. Abelson, J. Phys. C **19**, 455204 (2007).
[18] M.M.J. Treacy and J.M. Gibson, Acta Crystall. A - Crys. **52**, 212 (1996).
[19] J.. Gibson, M.M.. Treacy, and P.. Voyles, Ultramicroscopy **83**, 169 (2000).
[20] R. Hosemann and S.N. Baggchi, *Direct Analysis of Diffraction by Matter* (North-Holland, Amsterdam, 1962).
[21] P.A. Fedders, D.A. Drabold, and S. Nakhmanson, Phys. Rev. B **58**, 15624 (1998).
[22] J. Dong and D.A. Drabold, Phys. Rev. Lett. **80**, 1928 (1998).
[23] Y. Pan, F. Inam, M. Zhang, and D.A. Drabold, Phys. Rev. Lett. **100**, 206403 (2008).
[24] G. Allan, C. Delerue, and M. Lannoo, Phys. Rev. B **57**, 6933 (1998).
[25] D.A. Drabold, Y. Li, B. Cai, and M. Zhang, Phys. Rev. B **83**, 045201 (2011).
[26] A.H.M. Smets, M.A. Wank, B. Vet, M. Fischer, R.A.C.M.M. van Swaaij, M. Zeman, D.C. Bobela, C.R. Wronski, and R.M.C.M. van de Sanden, IEEE Journal of Photovoltaics **2**, 94 (2012).
[27] S.T. Pantelides, Phys. Rev. Lett. **57**, 2979 (1986).
[28] L.K. Wagner and J.C. Grossman, Phys. Rev. Lett. **101**, 265501 (2008).
[29] P.A. Khomyakov, W. Andreoni, N.D. Afify, and A. Curioni, Phys. Rev. Lett. **107**, 255502 (2011).

[30] A.H.M. Smets, W.M.M. Kessels, and M.C.M. van de Sanden, Appl. Phys. Lett. **82**, 1547 (2003).
[31] A. Smets and M. van de Sanden, Phys. Rev. B **76**, (2007).
[32] J. Melskens, A.H.M. Smets, S.W.H. Eijt, H. Schut, E. Brück, and M. Zeman, J. Non-Cryst. Solids **358**, 2015 (2012).
[33] E.C. Freeman and W. Paul, Phys. Rev. B **20**, 716 (1979).
[34] G.D. Cody, C.R. Wronski, B. Abeles, R.B. Stephens, and B. Brooks, Solar Cells **2**, 227 (1980).
[35] W.E. Spear and P.G. Le Comber, Solid State Comm. **17**, 1193 (1975).
[36] N.F. Mott, Phil. Mag. **19**, 835 (1969).
[37] R.A. Street, J. Kakalios, and T.M. Hayes, Phys. Rev. B **34**, 3030 (1986).
[38] J. Kakalios and R.A. Street, in *Amorphous Silicon and Related Materials*, edited by H. Fritzsche (World Scientific Publishing Company, 1988), p. 165.
[39] D.L. Staebler and C.R. Wronski, Appl. Phys. Lett. **31**, 292 (1977).
[40] D.L. Staebler and C.R. Wronski, J. Appl. Phys. **51**, 3262 (1980).
[41] C. van Berkel and M.J. Powell, Appl. Phys. Lett. **51**, 1094 (1987).
[42] M. Stutzmann, W.B. Jackson, and C.C. Tsai, Phys. Rev. B **32**, 23 (1985).
[43] H.M. Branz, Phys. Rev. B **59**, 5498 (1999).
[44] R. Biswas, B.C. Pan, and Y.Y. Ye, Phys. Rev. Lett. **88**, 205502 (2002).
[45] W. Kruhler, H. Pfeiderer, R. PLattner, and W. Stetter, in *AIP Conference Proceedings* (1984), p. 311.
[46] P. Stradins and H. Fritzsche, J. Non-Cryst. Solids **198–200, Part 1**, 432 (1996).
[47] J. Kakalios and W.B. Jackson, in edited by H. Fritzsche (World Scientific Publishing Company, 1988), p. 207.
[48] H. Fritzsche, in *Amorphous and Polycrystalline Thin-Film Silicon Science and Technology* (Mater. Res. Soc. Symp. Proc. 1245, Pittsburgh, PA, 2010), p. A.14.01.
[49] J.M. Pearce, J. Deng, R.W. Collins, and C.R. Wronski, Appl. Phys. Lett. **83**, 3725 (2003).
[50] S.Y. Myong and K.S. Lim, Appl. Phys. Lett. **88**, 243510 (2006).
[51] A.H.M. Smets, in *Amorphous and Polycrystalline Thin-Film Silicon Science and Technology* (Mater. Res. Soc. Symp. Proc. 1245, Pittsburgh, PA, 2010), p. A.14.02.
[52] D.C. Bobela, H.M. Branz, and P. Stradins, Appl. Phys. Lett. **98**, 201908 (2011).
[53] R. Butte, R. Meaudre, M. Meaudre, S. Vignoli, C. Longeaud, J.P. Kleider, and P.R. i Cabarrocas, Phil. Mag. B **79**, 1079 (1999).
[54] J. Kočka, A. Vetushka, and A. Fejfar, Phil. Mag. **89**, 2557 (2009).
[55] L. Fekete, P. Kužel, H. Němec, F. Kadlec, A. Dejneka, J. Stuchlík, and A. Fejfar, Phys. Rev. B **79**, 115306 (2009).
[56] L.R. Wienkes, C. Blackwell, and J. Kakalios, Appl. Phys. Lett. **100**, 072105 (2012).
[57] T. Dylla, S. Reynolds, R. Carius, and F. Finger, J. Non-Cryst. Solids **352**, 1093 (2006).
[58] K. Lips, P. Kanschat, and W. Fuhs, Sol. Energy Mater. Sol. Cells **78**, 513 (2003).
[59] A.H.M. Smets, T. Matsui, and M. Kondo, J. Appl. Phys. **104**, 034508 (2008).
[60] B.I. Shklovskii and A.L. Efros, *Electronic Properties of Doped Semiconductors* (Springer-Verlag, Berlin, Heidelberg, New York, Tokyo, 1984).

[61] C. Godet, Phil. Mag. B **81**, 205 (2001).
[62] C. Godet, J. Non-Cryst. Solids **299–302, Part 1**, 333 (2002).
[63] M. Grünewald and P. Thomas, Phys. Stat. Sol. (b) **94**, 125 (1979).
[64] M. Ortuno and M. Pollak, J. Non-Cryst. Solids **59–60, Part 1**, 53 (1983).
[65] M.H.A. Pramanik and D. Islam, J. Non-Cryst. Solids **45**, 325 (1981).
[66] K. Shimakawa, Phil. Mag. B **60**, 377 (1989).
[67] K. Shimakawa, Phys. Rev. B **39**, 12933 (1989).
[68] K. Shimakawa and K. Miyake, Phys. Rev. B **39**, 7578 (1989).
[69] K. Shimakawa and K. Miyake, Phys. Rev. Lett. **61**, 994 (1988).
[70] F. Cleri, P. Keblinski, L. Colombo, D. Wolf, and S.R. Phillpot, Europhys. Lett. **46**, 671 (2007).
[71] N. Robertson and L. Friedman, Phil. Mag. B **36**, 1013 (1977).
[72] N.F. Mott and E.A. Davis, *Electronic Processes in Non-crystalline Materials,*, 2nd ed. (Oxford, Clarendon Press, Oxford, 1979).
[73] R.A. Street, Phys. Rev. Lett. **49**, 1187 (1982).
[74] R.A. Street, D.K. Biegelsen, W.B. Jackson, N.M. Johnson, and M. Stutzmann, Phil. Mag. B **52**, 235 (1985).
[75] R.A. Street, M. Hack, and W.B. Jackson, Phys. Rev. B **37**, 4209 (1988).
[76] J.B. Johnson, Phys. Rev. **32**, 97 (1928).
[77] W. Schottky, Ann. D. Physik **57**, 541 (1918).
[78] I. Bloom and Y. Nemirovsky, Appl. Phys. Lett. **58**, 1664 (1991).
[79] E.A.M. Klumperink, S.L.J. Gierkink, A.P. Van Der Wel, and B. Nauta, IEEE Journal of Solid-State Circuits **35**, 994 (2000).
[80] E.G. Ioannidis, A. Tsormpatzoglou, D.H. Tassis, C.A. Dimitriadis, F. Templier, and G. Kamarinos, J. Appl. Phys. **108**, 106103 (2010).
[81] S.C. Lai, M.F. Yang, S. Bin Dolmanan, L. Ke, and X.W. Sun, IEEE Trans. Electron Devices **57**, 2306 (2010).
[82] Y. Nemirovsky, D. Corcos, I. Brouk, A. Nemirovsky, and S. Chaudhry, IEEE Instru. Meas. Mag. **14**, 14 (2011).
[83] G. Liu, S. Rumyantsev, M. Shur, and A.A. Balandin, Appl. Phys. Lett. **100**, 033103 (2012).
[84] A. van der Ziel, Adv. Electronics and Electron Phys. **49**, 225 (1979).
[85] M.B. Weissman, Rev. Mod. Phys. **60**, 537 (1988).
[86] P. Dutta and P.M. Horn, Rev. Mod. Phys. **53**, 497 (1981).
[87] A. D'Amico, G. Fortunato, and C.M. Van Vliet, Solid-State Electron. **28**, 837 (1985).
[88] J. C. Anderson, Phil. Mag. B **48**, 31 (1983).
[89] F. Z. Bathaei and Anderson, J.C., Phil **55**, 87 (1987).
[90] W.K. Choi, A.E. Owen, P.G. LeComber, and M.J. Rose, J. Appl. Phys. **68**, 120 (1990).
[91] C. Parman and J. Kakalios, Phys. Rev. Lett. **67**, 2529 (1991).
[92] C.E. Parman, N.E. Israeloff, and J. Kakalios, Phys. Rev. B **44**, 8391 (1991).
[93] K.K. Hung, P.K. Ko, C. Hu, and Y.C. Cheng, IEEE Electron. Device Lett. **11**, 90 (1990).

[94] K.S. Ralls, W.J. Skocpol, L.D. Jackel, R.E. Howard, L.A. Fetter, R.W. Epworth, and D.M. Tennant, Phys. Rev. Lett. **52**, 228 (1984).
[95] M.J. Uren, D.J. Day, and M.J. Kirton, Appl. Phys. Lett. **47**, 1195 (1985).
[96] M.J. Kirton and M.J. Uren, Adv. Phys. **38**, 367 (1989).
[97] N. Clément, K. Nishiguchi, A. Fujiwara, and D. Vuillaume, Nature Comm. **1**, 92 (2010).
[98] C.E. Parman, N.E. Israeloff, and J. Kakalios, Phys. Rev. Lett. **69**, 1097 (1992).
[99] C.E. Parman, N.E. Israeloff, and J. Kakalios, Phys. Rev. B **47**, 12578 (1993).
[100] G.M. Khera, Non-Gaussian Noise in Hydrogenated Amorphous Silicon, University of Minnesota, 1996.
[101] G.M. Khera and J. Kakalios, Phys. Rev. B **56**, 1918 (1997).
[102] K.M. Abkemeier, Phys. Rev. B **55**, 7005 (1997).
[103] R.E. Johanson, D. Scansen, and S.O. Kasap, Phil. Mag. B **73**, 707 (1996).
[104] R.E. Johanson, D. Scansen, and S.O. Kasap, J. Vac. Sci. Technol. B **17**, 73 (1999).
[105] R.E. Johanson, M. Güneş, and S.O. Kasap, J. Non-Cryst. Solids **266–269, Part 1**, 242 (2000).
[106] R.E. Johanson, S.O. Kasap, F. Gaspari, D. Yeghikyan, and S. Zukotynski, J. Vac. Sci. Technol. A **18**, 661 (2000).
[107] M. Güneş, R.E. Johanson, and S.O. Kasap, J. Non-Cryst. Solids **266-269**, 304 (2000).
[108] P.A.W.E. Verleg and J.I. Dijkhuis, Phys. Rev. B **58**, 3904 (1998).
[109] P.A.W.E. Verleg and J.I. Dijkhuis, Phys. Rev. B **58**, 3917 (1998).
[110] P.A.W.E. Verleg and J.I. Dijkhuis, J. Non-Cryst. Solids **266–269, Part 1**, 232 (2000).
[111] R.E. Johanson, M. Gunes, and S.O. Kasap, in *Circuits, Devices and Systems, IEEE Proceedings* (2002), pp. 68–74.
[112] S.B. Li, Z.M. Wu, Y.D. Jiang, W. Li, N.M. Liao, and J.S. Yu, Nanotechnology **19**, 085706 (2008).
[113] M. Güneş, R.E. Johanson, S.O. Kasap, F. Finger, and A. Lambertz, J. Mater. Science **14**, 731 (2003).
[114] J. Müller, F. Finger, R. Carius, and H. Wagner, Phys. Rev. B **60**, 11666 (1999).
[115] R.W. Lof and R.E.I. Schropp, J. Appl. Phys. **108**, 063714 (2010).
[116] Y. Adjallah, C. Anderson, U. Kortshagen, and J. Kakalios, J. Appl. Phys. **107**, 043704 (2010).
[117] S.B. Concari, R.H. Buitrago, M.T. Gutiérrez, and J.J. Gandía, J. Appl. Phys. **94**, 2417 (2003).
[118] G. Ambrosone, U. Coscia, A. Cassinese, M. Barra, S. Restello, V. Rigato, and S. Ferrero, Thin Solid Films **515**, 7629 (2007).
[119] A. Dussan and R.H. Buitrago, J. Appl. Phys. **97**, 043711 (2005).
[120] J. Kočka, T. Mates, H. Stuchlíková, J. Stuchlík, and A. Fejfar, Thin Solid Films **501**, 107 (2006).
[121] Y. Qin, H. Yan, F. Li, L. Qiao, Q. Liu, and D. He, Appl. Surf. Sci. **257**, 817 (2010).
[122] A. Di Nocera, A. Mittiga, and A. Rubino, J. Appl. Phys. **78**, 3955 (1995).
[123] J.M. Essick, Z. Nobel, Y.-M. Li, and M.S. Bennett, Phys. Rev. B **54**, 4885 (1996).

[124] M.A. Rafiq, Y. Tsuchiya, H. Mizuta, S. Oda, S. Uno, Z.A.K. Durrani, and W.I. Milne, J. Appl. Phys. **100**, 014303 (2006).
[125] E. Šimánek, Solid State Comm. **40**, 1021 (1981).
[126] J. -H Zhou, S.D. Baranovskii, S. Yamasaki, K. Ikuta, K. Tanaka, M. Kondo, A. Matsuda, and P. Thomas, Phys. Stat. Sol. (a) **205**, 147 (1998).
[127] S.J. Konezny, M.N. Bussac, and L. Zuppiroli, Appl. Phys. Lett. **92**, 012107 (2008).
[128] P. Sheng, Phys. Rev. B **21**, 2180 (1980).
[129] I. Balberg, J. Jedrzejewski, and E. Savir, Phys. Rev. B **83**, 035318 (2011).
[130] I.V. Antonova, M. Gulyaev, E. Savir, J. Jedrzejewski, and I. Balberg, Phys. Rev. B **77**, 125318 (2008).
[131] I. Balberg, Y. Dover, R. Naides, J.P. Conde, and V. Chu, Phys. Rev. B **69**, 035203 (2004).
[132] Y.-H. So, S. Huang, G. Conibeer, and M.A. Green, Europhys. Lett. **96**, 17011 (2011).
[133] S.Y. Myong, O. Shevaleevskiy, K.S. Lim, S. Miyajima, and M. Konagai, J. Appl. Phys. **98**, 054311 (2005).
[134] A.G. Zabrodskii and I.S. Shlimak, Sov. Phys. Semicond. **9**, 391 (1975).
[135] A.G. Zabrodskii, Phil. Mag. B **81**, 1131 (2001).
[136] L.R. Wienkes, C. Blackwell, and J. Kakalios, in *Amorphous and Polycrystalline Thin-Film Silicon Science and Technology*, edited by B. Yan, S. Higashi, C.C. Tsai, Q. Wang, and H. Gleskova (Mater. Res. Soc. Symp. Proc. 1321, Pittsburgh, PA, 2011), p. 285.
[137] R.C. Chittick, J.H. Alexander, and H.F. Sterling, J. Electrochem. Soc. **116**, 77 (1969).
[138] A. Matsuda, T. Kaga, H. Tanaka, and K. Tanaka, Japan. J. Appl. Phys. **23**, L567 (1984).
[139] H. Curtins, N. Wyrsch, and A.V. Shah, Electron. Lett. **23**, 228 (1987).
[140] S. Oda, J. Noda, and M. Matsumura, Japan. J. Appl. Phys. **28**, L1860 (1989).
[141] S. Oda, J. Noda, and M. Matsumura, Japan. J. Appl. Phys. **29**, 1889 (1990).
[142] W.M.M. Kessels, R.J. Severens, A.H.M. Smets, B.A. Korevaar, G.J. Adriaenssens, D.C. Schram, and M.C.M. van de Sanden, J. Appl. Phys. **89**, 2404 (2001).
[143] N.M. Johnson, J. Walker, C.M. Doland, K. Winer, and R.A. Street, Appl. Phys. Lett. **54**, 1872 (1989).
[144] A.H. Mahan, J. Carapella, B.P. Nelson, R.S. Crandall, and I. Balberg, J. Appl. Phys. **69**, 6728 (1991).
[145] H. Wiesmann, A.K. Ghosh, T. McMahon, and M. Strongin, J. Appl. Phys. **50**, 3752 (1979).
[146] H. Matsumura, J. Appl. Phys. **65**, 4396 (1989).
[147] J. Doyle, R. Robertson, G.H. Lin, M.Z. He, and A. Gallagher, J. Appl. Phys. **64**, 3215 (1988).
[148] M.H. Brodsky, M. Cardona, and J.J. Cuomo, Phys. Rev. B **16**, 3556 (1977).
[149] P.E. Vanier, F.J. Kampas, R.R. Corderman, and G. Rajeswaran, J. Appl. Phys. **56**, 1812 (1984).
[150] G. Ganguly and A. Matsuda, Phys. Rev. B **47**, 3661 (1993).
[151] A. Matsuda, J. Non-Cryst. Solids **338–340**, 1 (2004).

[152] R. Collins, A. Ferlauto, G. Ferreira, C. Chen, J. Koh, R. Koval, Y. Lee, J. Pearce, and C. Wronski, Sol. Energy Mater. Sol. Cells **78**, 143 (2003).
[153] P. Roca i Cabarrocas, S. Hamma, S.. Sharma, G. Viera, E. Bertran, and J. Costa, J. Non-Cryst. Solids **227–230, Part 2**, 871 (1998).
[154] A. Matsuda, J. Non-Cryst. Solids **59–60, Part 2**, 767 (1983).
[155] C.C. Tsai, G.B. Anderson, R. Thompson, and B. Wacker, J. Non-Cryst. Solids **114, Part 1**, 151 (1989).
[156] K. Nakamura, K. Yoshino, S. Takeoka, and I. Shimizu, Japan. J. Appl. Phys. **34**, 442 (1995).
[157] A. Matsuda, Thin Solid Films **337**, 1 (1999).
[158] U.K. Das, P. Chaudhuri, and S.T. Kshirsagar, J. Appl. Phys. **80**, 5389 (1996).
[159] K. Bhattacharya and D. Das, J. Phys. D **41**, 155420 (2008).
[160] A. Bouchoule, *Dusty Plasmas: Physics, Chemistry and Technological Impacts in Plasma Processing* (Wiley, Chichester□; New York, 1999).
[161] A.V. Kharchenko, V. Suendo, and P.R. i Cabarrocas, Thin Solid Films **427**, 236 (2003).
[162] A.F. i Morral and P.R. i Cabarrocas, Thin Solid Films **383**, 161 (2001).
[163] J.P. Kleider, C. Longeaud, M. Gauthier, M. Meaudre, R. Meaudre, R. Butté, S. Vignoli, and P. Roca i Cabarrocas, Appl. Phys. Lett. **75**, 3351 (1999).
[164] O. Saadane, S. Lebib, A.V. Kharchenko, C. Longeaud, and R. Roca i Cabarrocas, J. Appl. Phys. **93**, 9371 (2003).
[165] J. Kakalios, U. Kortshagen, C. Blackwell, C. Anderson, Y. Adjallah, L.R. Wienkes, K. Bodurtha, and J. Trask, in *Amorphous and Polycrystalline Thin-Film Silicon Science and Technology* (Mater. Res. Soc. Symp. Proc. 1321, Pittsburgh, PA, 2011).
[166] L. Mangolini, E. Thimsen, and U. Kortshagen, Nano Lett. **5**, 655 (2005).
[167] C.B. Blackwell, Effects of Nanocrystalline Silicon Inclusions in Doped and Undoped Thin Films of Hydrogenated Amorphous Silicon, University of Minnesota, 2009.
[168] D.J. Griffiths, *Introduction to Electrodynamics*, 3rd ed. (Prentice Hall, Upper Saddle River, NJ, 1999).
[169] G. Herzberg, *Molecular Spectra and Molecular Structure* (Prentice-Hall, New York, 1939).
[170] B.C. Smith, *Fundamentals of Fourier Transform Infrared Spectroscopy*, 2nd ed. (CRC Press, Boca Raton, FL, 2011).
[171] Y.J. Chabal and K. Raghavachari, Phys. Rev. Lett. **53**, 282 (1984).
[172] V.A. Burrows, Y.J. Chabal, G.S. Higashi, K. Raghavachari, and S.B. Christman, Appl. Phys. Lett. **53**, 998 (1988).
[173] G. Lucovsky, R.J. Nemanich, and J.C. Knights, Phys. Rev. B **19**, 2064 (1979).
[174] E. Bhattacharya and A.H. Mahan, Appl. Phys. Lett. **52**, 1587 (1988).
[175] C. Manfredotti, F. Fizzotti, M. Boero, P. Pastorino, P. Polesello, and E. Vittone, Phys. Rev. B **50**, 18046 (1994).
[176] K.K. Gleason, M.A. Petrich, and J.A. Reimer, Phys. Rev. B **36**, 3259 (1987).
[177] H. Wagner and W. Beyer, Solid State Comm. **48**, 585 (1983).
[178] D. Quicker and J. Kakalios, Phys. Rev. B **60**, 2449 (1999).

[179] L. Xu, Z.P. Li, C. Wen, and W.Z. Shen, J. Appl. Phys. **110**, 064315 (2011).
[180] E.C. Le Ru, *Principles of Surface-Enhanced Raman Spectroscopy and Related Plasmonic Effects*, 1st ed. (Books24x7com, Norwood Mass, 2005).
[181] H. Richter, J. Appl. Phys. **52**, 7281 (1981).
[182] V. Paillard, P. Puech, M.A. Laguna, R. Carles, B. Kohn, and F. Huisken, J. Appl. Phys. **86**, 1921 (1999).
[183] G. Viera, S. Huet, and L. Boufendi, J. Appl. Phys. **90**, 4175 (2001).
[184] T.Y. Kim, N.M. Park, K.H. Kim, G.Y. Sung, Y.W. Ok, T.Y. Seong, and C.J. Choi, Appl. Phys. Lett. **85**, 5355 (2004).
[185] R. Meyer and D. Comtesse, Phys. Rev. B **83**, 014301 (2011).
[186] C. Smit, R.A.C.M.M. van Swaaij, H. Donker, A.M.H.N. Petit, W.M.M. Kessels, and M.C.M. van de Sanden, J. Appl. Phys. **94**, 3582 (2003).
[187] R. Saleh and N.H. Nickel, Thin Solid Films **427**, 266 (2003).
[188] R. Tsu, J. Gonzalez-Hernandez, S.S. Chao, S.C. Lee, and K. Tanaka, Appl. Phys. Lett. **40**, 534 (1982).
[189] A.T. Voutsas, M.K. Hatalis, J. Boyce, and A. Chiang, J. Appl. Phys. **78**, 6999 (1995).
[190] V. Golubev, V. Davydov, A. Medvedev, A. Pevtsov, and N. Feoktistov, Physics of the Solid State **39**, 1197 (1997).
[191] E. Bustarret, M.A. Hachicha, and M. Brunel, Appl. Phys. Lett. **52**, 1675 (1988).
[192] E. Lifshin and I. ebrary, *X-ray Characterization of Materials* (Wiley-VCH, Weinheim□; New York, 1999).
[193] M. Tanielian, M. Chatani, H. Fritzsche, V. Šmíd, and P.D. Persans, J. Non-Cryst. Solids **35-36**, 575 (1980).
[194] A.G. Zabrodskii, Sov. Phys. Semicond. **11**, 345 (1977).
[195] R.M. Hill, Phys. Stat. Sol. (a) **35**, K29 (1976).
[196] J. Kakalios, R.A. Street, and W.B. Jackson, Phys. Rev. Lett. **59**, 1037 (1987).
[197] 27-1402, ASTM card number, (n.d.).
[198] D.C. Marra, E.A. Edelberg, R.L. Naone, and E.S. Aydil, J. Vac. Sci. Technol. A **16**, 3199 (1998).
[199] S. Reynolds, J. Optoelectron. Adv. Mater. **11**, 1086 (2009).
[200] T. Matsui, M. Kondo, and A. Matsuda, J. Non-Cryst. Solids **338–340**, 646 (2004).
[201] T. Toyama, W. Yoshida, Y. Sobajima, and H. Okamoto, J. Non-Cryst. Solids **354**, 2204 (2008).
[202] S.F. Wang, Y.F. Hsu, J.C. Pu, J.C. Sung, and L.G. Hwa, Mater. Chem. Phys. **85**, 432 (2004).
[203] L.M. Lust and J. Kakalios, Phys. Rev. Lett. **75**, 2192 (1995).
[204] L. Pichon, E. Jacques, R. Rogel, A.C. Salaun, and F. Demami, Semicond. Sci. Tech. **28**, 025002 (2013).
[205] L. Pichon and R. Rogel, Appl. Phys. Lett. **99**, 072106 (2011).